Functional Relevance of the Extracellular Matrix Proteins Periostin and Tenascin C during Liver Damage and Regeneration

von Michaela Christina Hrabak

Inaugural-Dissertation zur Erlangung der Doktorwürde der

Tierärztlichen Fakultät der Ludwig-Maximilians-Universität

München

Functional Relevance of the Extracellular Matrix Proteins Periostin and Tenascin C during Liver Damage and Regeneration

von Michaela Christina Hrabak

aus Ansbach

München 2021

Aus dem Veterinärwissenschaftlichen Department der
Tierärztlichen Fakultät der Ludwig-Maximilians-Universität München

Lehrstuhl für Molekulare Tierzucht und Biotechnologie

Arbeit angefertigt unter der Leitung von Univ.-Prof. Dr. Maik Dahlhoff

Angefertigt am:

Institut für Pathologie des Universitätsklinikums Düsseldorf

Mentor: Univ.-Prof. Dr. Irene Esposito

Gedruckt mit der Genehmigung der Tierärztlichen Fakultät

der Ludwig-Maximilians-Universität München

Dekan: Univ.-Prof. Dr. Reinhard K. Straubinger, Ph.D.

Berichterstatter: Univ.-Prof. Dr. Maik Dahlhoff

Korreferent: Univ.-Prof. Dr. Cornelia A. Deeg

Tag der Promotion: 06. Februar 2021

Für meine Familie

Parts of this study were presented at the following conferences:

CRC 974 “Communication and system relevance in liver damage and regeneration“ Retreat, Heinrich-Heine-University Dusseldorf, Trier, April 21 – 22, 2018

103. Annual Conference of the German Society of Pathology, Frankfurt on the Main, June 13 – 15, 2019

TABLE OF CONTENTS

ABBREVIATIONS

ACTA2	Actin alpha 2, smooth muscle
ADM	Acinar-to-ductal-metaplasia
aHSC	Activated hepatic stellate cells
AII	Angiotensin II
ALD	Alcoholic liver disease
aMF	Activated myofibroblasts
AMP	Adenosine monophosphate
AMPK	AMP-activated protein kinase
aPF	Activated portal fibroblasts
BAX	BCL2 associated X, apoptosis regulator
BCL2	Apoptosis regulator B-cell lymphoma 2
BD	Bile duct
BDL	Bile duct ligation
CCL2	CC-chemokine ligand 2
CCl_3*	Trichloromethyl radical
CCl_3OO*	Trichloromethylperoxy radicals
CCl_4	Carbon tetrachloride
CCR2	CC-chemokine receptor 2
CDE	Choline-deficient ethionine-supplemented
CoH	Canal of Hering
CTD	Carboxyl-terminal domain
CTD	Carboxyl-terminal domain
Ctrl	Control
d	Days
DNA	Deoxyribonucleic acid
DDE	3,5-diethoxycarbonyl-1,4-dihydrocollidine
DR	Ductular reaction
EMT	Epithelial-to-mesenchymal transition
ERK	Extracellular signal-regulated kinase
FFPE	Formalin fixed paraffin embedded
GAG	Glycosaminoglycan chains

GFAP	Glial fibrillary acidic protein
GLB1	β-galactosidase
GMEM	Glioma mesenchymal extracellular matrix antigen
HA	Hepatic artery
HCC	Hepatocellular carcinoma
HE	Hematoxylin-Eosin
HGF	Hepatocyte growth factor
HPF	High-power field
HSC	Hepatic stellate cells
HVB	Hepatitis B virus
HVC	Hepatitis C virus
i.p.	Intra peritoneal
IFNG	Interferon-γ
iHSC	Inactivated hepatic stellate cells
IL6	Interleukin-6
IPF	Idiopathic pulmonary fibrosis
JAK	Janus kinase
K1C19	Keratin, type I cytoskeletal 19
LBW-r. %	Liver-body weight-relation
LOX	Lysyl oxidase
MF	Myofibroblasts
MMPs	Matrix metalloproteinases
MKI67	Proliferation marker protein Ki-67
NAFLD	Non-alcoholic fatty liver disease
NASH	Non-alcoholic steatohepatitis
NK	Natural killer cells
NKT	Liver-specific cells γδ T
PBC	Primary biliary cholangitis
PDGF	Platelet-derived growth factor
PF	Portal fibroblasts
PHx	Partial hepatectomy
PI3K	Phosphatidylinositol 3-kinase
POSTN	Periostin

PPARA	Peroxisome proliferator-activated receptor α
PSC	Primary sclerosing cholangitis
PSR	Picro Sirius Red
PT	Portal tract
PV	Portal vein
qHSC	Quiescent hepatic stellate cells
qRT-PCR	Quantitative real-time polymerase chain reaction
RAS	Renin-angiotensin system
RUNX2	Runt-related transcription factor 2
ROS	Reactive oxygen species
SEM	Standard error of the mean
sHSC	Senescent hepatic stellate cells
SMAD	Mothers against decapentaplegic homolog
SOX9	Sex-determining region Y-box 9
SP	Signal peptide
STAT3	Signal transducer and activator of transcription 3
STE	Saline Tris-EDTA
TA	Tenascin assembly
TAA	Thioacetamide
TGFA	Transforming growth factor-alpha
TGFB	Transforming growth factor-beta
TIMPs	Tissue inhibitors of metalloproteinases
TNC	Tenascin C
TNFR1	TNF receptor 1
TNR6	Tumor necrosis factor receptor superfamily member 6
TRAIL	TNF-related apoptosis-inducing ligand
wks	Weeks
ZETT	Zentrale Einrichtung für Tierforschung und wissenschaftliche Tierschutzaufgaben

I. INTRODUCTION

The liver has a remarkable regenerative capacity. Therefore, after a mild or acute injury, mature hepatocytes proliferate and restore liver parenchyma. Severe or chronic damage is associated with fibrogenesis and the activation of hepatic progenitor cells (HPC) [1]. Liver fibrosis is defined by the excessive accumulation of extracellular matrix (ECM). The ongoing formation of fibrous scars can ultimately lead to cirrhosis, portal hypertension and liver failure [2]. Liver diseases are one of the major causes of morbidity and mortality worldwide and cause approximately two million deaths per year [3]. Despite intensive research, the most effective therapy is still to remove the causative agent [4]. Following liver injuries, hepatic stellate cells (HSC) get activated and transdifferentiate into ECM producing myofibroblasts (MF). These activated HSC are the main contributor to liver fibrosis [2]. The ECM provides structural features and can also actively regulate different cell functions, such as proliferation, migration and differentiation [5]. Besides fibrogenesis, the activation of HPC plays an important role after severe liver damage. The bipotential HPC can transdifferentiate either into hepatocytes or into cholangiocytes, which can be histologically observed as ductular reaction (DR) [6]. During liver regeneration, the liver parenchyma is restored and the fibrous scar is removed [7,8]. The two ECM proteins Periostin (POSTN) and Tenascin C (TNC) are both upregulated during inflammatory and fibrotic processes in different organs. In mouse models, the loss of POSTN causes a reduced stiffness of the heart muscle after myocardial infarction and leads to cardiac rupture [9]. Deficiency of TNC results in reduced myocardial fibrosis after chronic pressure overload in mice, as well [10]. However, the role of POSTN and TNC in liver diseases is not fully elucidated so far. Thus, the aim of this study is to investigate the functional relevance of these two proteins during liver damage and regeneration. Furthermore, their influence on the dedifferentiation and proliferation of HPC is being investigated. Therefore, a cholestatic and a toxin-mediated liver fibrosis as well as a partial hepatectomy were induced or applied to control, POSTN- and TNC-deficient mice.

1. The liver of mice

1.1. Anatomy and histology of the liver

The liver is the largest gland and main metabolic organ, which is located subdiaphragmatic in the abdomen. It weights between 3-5 % of the body weight (1-2 g) and consists of four lobes: the right lobe, medial lobe, left lobe, and the caudate lobe (Fig. 1). The liver has a dual blood supply. The portal vein transports about 60-70% of the blood from unpaired organs, especially from the gastrointestinal tract to the liver, whereas the hepatic artery provides 30-40% of oxygen-rich blood. Both vessels enter the liver through the hilum and branch out to interlobular veins and arteries [11–13].

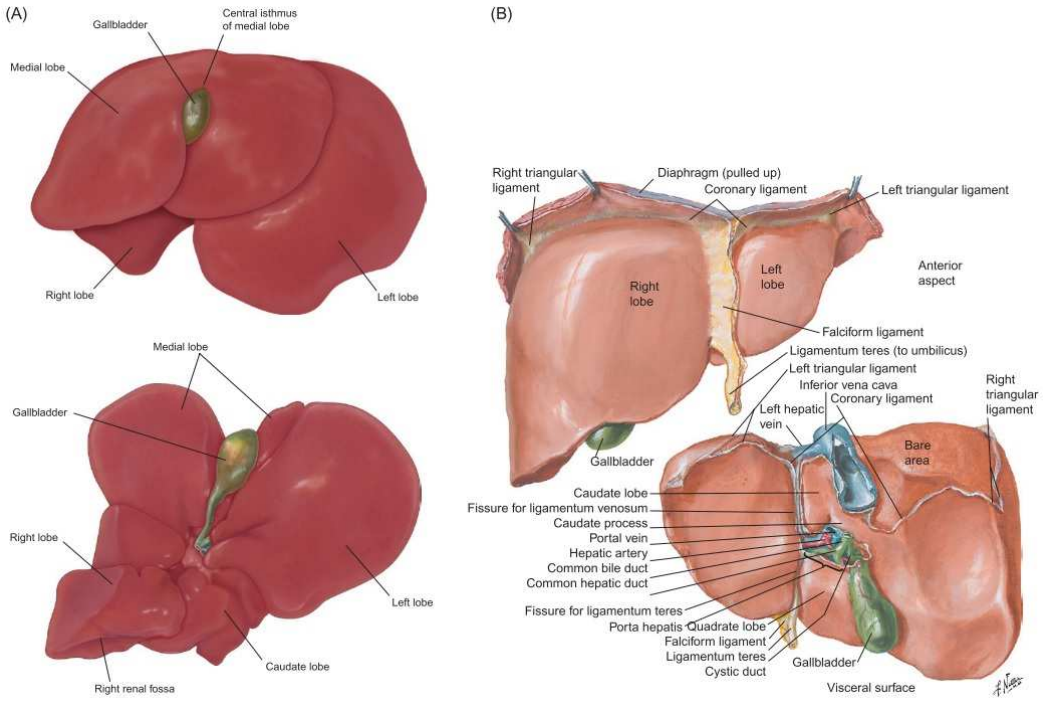

Fig. 1: Comparative anatomy of the liver of mice (A) and humans (B). The murine liver consists of four liver lobes: the right lobe, medial lobe, the left lobe, and the caudate lobe. The human liver also consists of four lobes: the left lobe, the right lobe, the quadrate lobe and the caudate lobe [13].

The liver is coated by the Glisson‘s capsule and connective tissue separates the liver parenchyma into lobules. Each lobule has a central vein (CV) in the center and portal tracts (PT) at the periphery. The PT contains a portal vein (PV), a hepatic artery (HA) and a bile duct (BD) and is also named Glisson’s triad. The liver

parenchyma between the CV and the PT, the acinus, can be divided into three zones. Zone 1 is “periportal” and next to the PT. Zone 3 is “centrilobular” and around the CV and Zone 2 is in between (Fig. 2) [11].

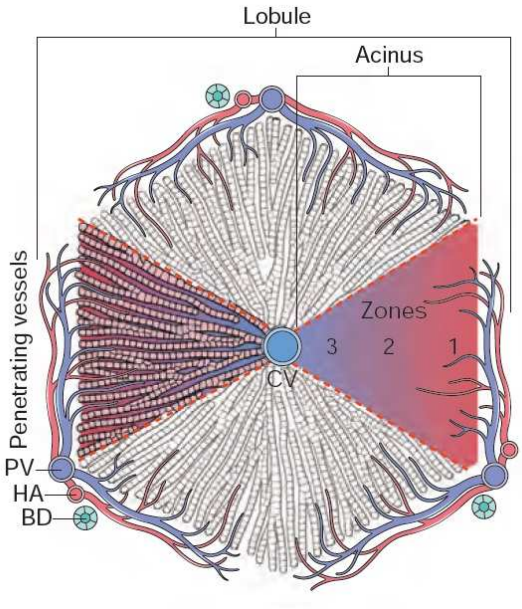

Fig. 2: Liver lobule. The central vein (CV) is in the center of the lobule. The portal tract (PT) at the periphery contains a portal vein (PV), a hepatic artery (HA) and a bile duct (BD). The acinus can be divided into three zones, whereby zone 1 is “periportal” and zone 3 is “centrilobular” [11].

Hepatocytes make up to 70% of the total liver cells and represent the parenchyma. They are arranged in plates from the PT to the CV. Between adjacent hepatocytes are bile canaliculi. Thereby, secreted bile and other metabolized compounds can be transported to the BD of the PT and finally excreted via the bile into the duodenum. The blood from the PV and HA flows into the sinusoids. They are the capillaries of the liver, run between the hepatocyte plates and end in the CV. Another important histological component of the liver is the space of Disse, which is located between the sinusoids and the hepatocytes [14,15]. In this perisinusoidal space different cell types are located: Kupffer cells as liver resident macrophages as well as HSC which store vitamin A in droplets and are able to transdifferentiate into MF in response to liver injury [2,15].

1.2. Physiology of the liver

The liver is the main metabolic organ in mammals and humans with various

functions. It receives nutrient-rich blood from the gastrointestinal tract via the PV which is mainly metabolized in the hepatocytes. They metabolize carbohydrates, lipids, and proteins (e.g. via glycolysis, gluconeogenesis) and synthesize proteins (e.g. albumin). Furthermore, hepatocytes produce bile to facilitate the digestion of fat and fat-soluble components of the chyme. Drugs and other potentially toxic substances are metabolized in the liver as well and are excreted via the bile. The metabolic functions of the liver depend on the zones. In the periportal area, glycogenic processes occur, whereas glycolytic processes take place close to the CV. This results from the oxygen content of the blood and the zonal distribution of the required enzymes. Besides the metabolic and detoxifying functions, the liver also serves as a storage for glycogen and vitamin A [14].

2. Liver fibrosis

Liver fibrosis is defined as an abnormal accumulation of ECM proteins. It is a wound-healing response to persisting liver injury. The main causes are cholestatic and metabolic diseases as well as viral and autoimmune hepatitis [2]. The progressing deposition of ECM and the resulting disorder of the architecture of the liver can lead to cirrhosis and/or hepatocellular carcinoma (HCC). Cirrhosis is the end stage of liver fibrosis and is characterized by an altered hepatic function and the development of regenerative nodules of hepatocytes [16,17].

2.1. Pathogenesis of liver fibrosis

Fibrosis is the consequence of the persistent wound-healing response of the liver induced by a series of events. Various agents like bile acids, metabolites or viruses can cause liver injuries and induce apoptosis and/or necrosis of epithelial cells, like hepatocytes or cholangiocytes [2,18]. The damaged cells release inflammatory and fibrogenic cytokines, reactive oxygen species (ROS) and chemoattractants to recruit inflammatory cells and macrophages. Phagocytosis of apoptotic cells and cell debris activate intracellular signaling cascades in macrophages which activates them. Macrophages start secreting ROS and cytokines, such as the platelet-derived growth factor (PDGF) and the transforming growth factor-beta 1 (TGFB1) which leads to a further recruitment of leucocytes [19,20].

This inflammatory milieu activates HSC to transdifferentiate into an active,

myofibroblast-like phenotype. These activated HSC (aHSC) are one of the main producers of ECM and secrete inflammatory and fibrogenic cytokines as well. The release of these factors keeps up the vicious circle of sustained inflammation and fibrosis of the liver [17,21,22]. Besides aHSC, other MF can be recruited (e.g. portal MF) and thereby contribute as well to progressive liver fibrosis [23,24]. The excessive collagen deposition is also a result of the imbalance between ECM-degrading matrix metalloproteinases (MMPs) and their corresponding inhibitors: the tissue inhibitors of metalloproteinases (TIMPs) [25,26]. MMPs are a family of endopeptidases which degrade different ECM molecules, influence the immune response, and thereby contribute to tissue homeostasis. During liver fibrosis, the expression of TIMPs, their specific inhibitors, is upregulated. The inhibition of MMPs results in a reduced degradation and thereby in an increased accumulation of ECM (Fig. 3) [27,28].

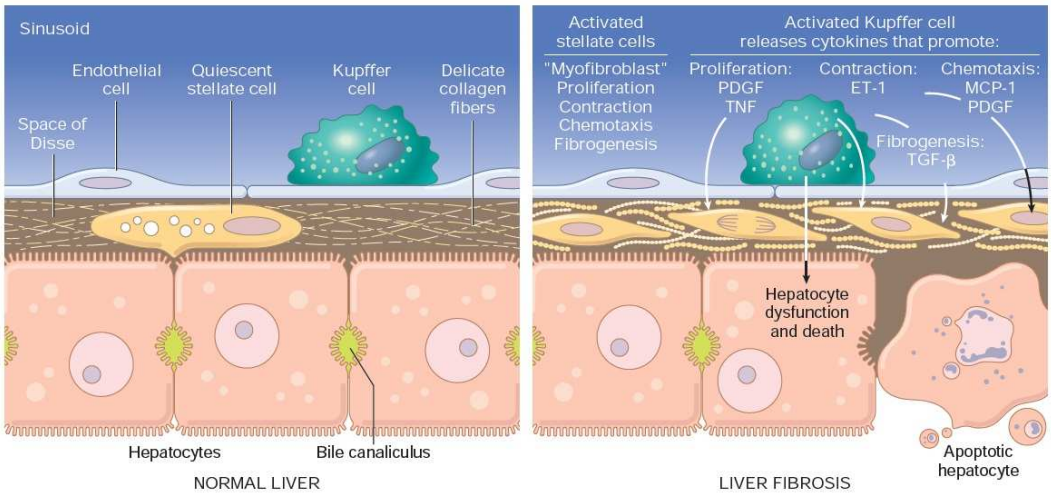

Fig. 3: Subendothelial changes during fibrogenesis. In the normal liver, HSC are in a quiescent state and store vitamin A. In response to liver injury, HSC get activated, transdifferentiate into fibrogenic MF and secrete ECM. The excessive accumulation of ECM lead to liver fibrosis [11].

2.2. Origin of fibrogenic myofibroblasts in liver fibrosis

The accumulation of ECM results from the activation of mesenchymal cells into MF in response to chronic liver damage [16,23]. In the past, aHSC were considered as the main producing cells of the ECM. In recent years, studies demonstrate that there are more types of MF involved in liver fibrogenesis. Different origins of MF have been identified: HSC, portal fibroblasts (PF), epithelial-to-mesenchymal

transition (EMT) and bone-marrow derived fibroblasts. Depending on the etiology of liver damage, the contribution of the individual cell types varies [23,29,30].

Hepatic stellate cells

HSC are resident mesenchymal cells, located in the space of Disse and represent about 5-8% of total hepatic cells. Under normal conditions, they are in a quiescent state, store vitamin A in lipid droplets and produce collagen IV [31–33]. Quiescent HSC (qHSC) express neural markers like nerve growth factor receptor , synaptophysin and glial fibrillary acidic protein (GFAP) [16–18]. Following liver injury, qHSC get activated and transdifferentiate into contractile MF, the aHSC. They downregulate the expression of neural markers and lose their vitamin A-droplets. Activated HSC express myogenic markers like Actin alpha 2, smooth muscle (ACTA2), are motile and secrete collagens [4,37,38]. Due to their motility, aHSC can migrate and accumulate, where the parenchyma needs to be repaired. Chemoattractants, like PDGF and TGFB, attract aHSC to the site of liver injury where they promote fibrosis [39,40]. Lineage tracing studies demonstrate that aHSC are the major source of hepatic MF. Mederacke *et al*. generated a new transgenic mouse (LratCre) that labels 99% of HSC. They demonstrated that HSC contribute to 93.6% of myofibroblasts in the carbon tetrachloride (CCl_4)-model. To confirm their findings, they used the thioacetamide (TAA) model. In this model, the proportion of aHSC of MF was 94.8%. To determine the contribution of HSC in cholestatic liver fibrosis, the author worked with three models: the bile duct ligation (BDL), $Mdr2^{ko}$ mice and 3,5-diethoxycarbonyl-1,4-dihydrocollidine (DDC)-containing diet. In these models, the proportion of HSC was between 87 and 90%. Already seven days after the BDL, the aHSC rose to 80% of total ACTA2-expressing cells. These results indicate that aHSC are the major source of MF in toxic as well as in cholestatic liver diseases [41]. In contrast to this study, Iwaisako *et al*. assign aHSC a lower contribution to cholestatic liver diseases. They applied on collagen-α1(I)-GFP mice the BDL and the CCl_4-model. Their results of the BDL model showed an increasing contribution of aHSC with progressing fibrosis. The portion of aHSC correspond to 18±7% after 5 days, 47±3% after 17 days and with a maximum of 51±4% of MF 20 days after ligation of the bile duct. In the CCl_4-model, the author obtained similar results like Mederacke *et al*.. After a treatment for 1.5 month, they assign to aHSC

83±5.2% of total MF of the liver [42]. All in all, both studies illustrate that aHSC are the main contributors to fibrogenic cells in liver fibrosis.

HSC get activated by apoptotic and injured cells, like hepatocytes, endothelial and biliary cells. These damaged cells release fibrogenic cytokines and ROS. Thereby, leukocytes are recruited and Kupffer cells are activated which enhance the activation of HSC [18,43–45]. After their activation and transdifferentiation into MF, aHSC secrete excessively ECM, including collagen I and III [46,47]. Besides their function as fibrogenic cells, they are also pro-inflammatory cells. The secretion of cytokines and chemokines enables aHSC to recruit leukocytes, as well. This results in a vicious circle and promotes liver fibrosis [22,48].

Portal fibroblasts

PF are liver resident cells and located around bile ducts in the portal tract. Under normal conditions, they are part of the connective tissue and do not express ACTA2. In recent years, studies demonstrate that PF can get activated and contribute to liver fibrosis by producing ECM after a cholestatic liver injury [49,50]. PF are activated by apoptotic and injured cells, like hepatocytes, biliary and endothelial cells. These damaged cells release fibrogenic cytokines and ROS which activates PF and stimulate them to produce collagen, predominantly around bile ducts [2,51]. The activated PF (aPF) express ACTA2, proliferate and contribute to an enlargement of the portal tract in the course of cholestatic diseases [23,52]. As mentioned before, there are controversial results about the contribution of aPF to hepatic MF in chronic liver diseases. Mederacke *et al*. assign aHSC as the major source whereas Iwaisako et al. postulate that aPF are the dominant contributors in cholestatic liver fibrosis [41,42]. The group of Iwaisako performed the BDL and the CCl_4-model in mice. Afterwards, they compared the gene expression profile of BDL-aPF with BDL-aHSC and CCl_4-aHSC. The BDL-aHSC expressed less similar genes with CCl_4-aHSC (217 genes) than with BDL-aPF (635 genes) [42]. These data suggest that aHSC have different phenotypes as well as different gene expression profiles in different etiologies. Furthermore, these results illustrate the difficulties in the explicit assignment of activated MF (aMF) to a certain origin. Nevertheless, both lineage-tracing studies demonstrate that there are different origins of MF and that aPF contributes to cholestatic liver fibrosis.

Epithelial-to-mesenchymal transition

Epithelial-to-mesenchymal transition (EMT) describes the transdifferentiation from fully differentiated epithelial cells into fully differentiated mesenchymal cells [53]. Several studies demonstrate that EMT contributes to organ fibrosis in the lung and kidney [54,55]. There are controversial results about the contribution of EMT in liver fibrosis. Sicklick *et al*. demonstrate than in cell culture hepatic epithelial progenitor cells also express mesenchymal markers and conclude that EMT is possible in adult liver cells [56]. However, recent *in vivo* studies demonstrate that neither hepatocytes nor cholangiocytes undergo EMT in liver fibrosis in mice [57,58]. Activated HSC and aPF contribute to more than 95% of myofibroblasts. It can be concluded that EMT is no or only a minor source of MF during liver fibrogenesis [23,41].

Bone marrow-derived cells

Fibrocytes from bone marrow contribute to hepatic MF, as well. Forbes *et al*. studied the origin of hepatic MF in humans. In their study, a woman received a bone marrow transplant from a male donor. Afterwards, she developed an HCV-related cirrhosis and the authors analyzed, via *in situ* hybridization for the Y chromosome, MF from her liver biopsies. Forbes *et al*. demonstrate that 12.4% of the hepatic MF were positive for the Y chromosome [59]. Recent studies have shown that the migration of fibrocytes from the bone marrow to the liver also occurs in mice. Kisseleva *et al*. transplanted bone marrow from collagen α1(I)-GFP^+ reporter mice in chimeric mice. Afterwards, the authors performed the BDL to induce a cholestatic liver fibrosis in these chimeric mice. Analysis of the liver tissue reveal that collagen-expressing GFP^+ cells are detectable and derive from bone marrow [24]. Another study of Scholten *et al*. subject bone marrow transplanted mice to a CCl_4-induced liver fibrosis. This study confirms that fibrocytes migrate from the bone-marrow to the liver and transdifferentiate into MF [60].

2.3. Key cytokines and signaling pathways involved in liver fibrosis

Different cytokines and the associated signaling pathways affect the activation and the different features of MF. PDGF is the most potent mitogen cytokine. Damaged cells and stimulated immune cells, especially Kupffer cells, secrete PDGF and

thereby stimulate the proliferation and migration of MF [61,62]. PDGF induces the activation of the extracellular signal-regulated kinase (ERK) signaling pathway. Thereby PDGF mediates the migration and proliferation of HSC [63]. Besides the mitogenic feature, PDGF is also fibrogenic. It regulates via the phosphatidylinositol 3-kinase (PI3K) pathway fibrogenic actions in HSC [64]. However, the most potent fibrogenic cytokine is TGFB which acts via the TGFB/ mothers against decapentaplegic homolog (SMAD) pathway in HSC. It thereby stimulates the differentiation of HSC into myofibroblast-like cells which produce ECM [65–67]. Furthermore, TGFB stimulates the expression of TIMPs and therefore the degradation of the ECM will be prevented [68].

Besides mitogenic and fibrogenic cytokines, vasoactive mediators regulate liver fibrosis, as well. Vasodilators (e.g. relaxin) have antifibrotic effects and vasoconstrictors (e.g. norepinephrine and angiotensin II (AII)) promote fibrogenesis [69,70,71]. Activated HSC secrete AII, a vasoconstrictive mediator from the renin-angiotensin system (RAS), which can regulate the intrahepatic blood flow by increasing the blood pressure. Moreover, AII binds to AI receptors in contractile aHSC. Thereby, AII stimulate the proliferation and migration of aHSC as well as the synthesis of ECM [48,72,73]. Adipokines, cytokines mainly from the adipose tissue, are another group of mediators that have an important impact on liver fibrosis. Leptin is a profibrogenic adipokine which acts via the Janus kinase (JAK)-signal transducer and activator of transcription 3 (STAT3) signaling pathway. Thereby it can activate HSC, macrophages and Kupffer cells. In addition, leptin can stimulate TIMPs whereby it inhibits the collagen degradation [74,75,76]. Adiponectin is an anti-fibrotic adipokine which acts via adenosine monophosphate (AMP)-activated protein kinase (AMPK) and the peroxisome proliferator-activated receptor alpha (PPARA). Adiponectin is thus able to inhibit the proliferation of HSC and reduce liver fibrosis [77,78].

2.4. Fibrosis patterns in different liver diseases

Different etiologies of chronic liver diseases lead to different fibrosis patterns. Chronic cholestatic liver diseases (e.g. primary biliary cholangitis (PBC), primary sclerosing cholangitis (PSC)) are characterized by portal fibrosis with porto-portal septa [79,80]. In chronic virus hepatitis (e.g. hepatitis B virus (HVB) and HVC

infections), fibrosis also develops in the PT. With progressing disease, the PT get larger and fibrous septa from the PT to the CV are formed, as well [81]. In alcoholic liver disease (ALD) and non-alcoholic fatty liver disease (NAFLD), fibrosis starts centrilobular and the so called pericentral fibrosis can be observed [81,82].

3. Liver regeneration

For a long time, the regression of liver fibrosis was considered as impossible. However, many studies demonstrate that the liver has a remarkable regenerative capacity and that even advanced liver fibrosis is reversible if the underlying agent is removed. The fibrous scar can be removed, hepatocytes regenerate and a normal liver architecture can be restored [7,83,84].

3.1. Reversibility of liver fibrosis

The reversibility of liver fibrosis is characterized by decreased fibrogenic cytokines and increased activity of collagenases. The aMF disappear and the fibrous septa are removed [2,85]. Activated HSC, the major source of aMF, can undergo apoptosis, senescence or return to an inactivated phenotype. Apoptosis can be induced by an increased expression of TNF receptor 1 (TNFR1) and their ligands. This leads to a caspase8/caspase3-mediated cell death. Furthermore, the caspase9-dependent apoptosis can be activated by an overexpression of proapoptotic proteins (e.g. apoptosis regulator B-cell lymphoma 2 (BCL2), BCL2 associated X, apoptosis regulator (BAX)) [85,86]. Activated HSC can also undergo senescence. These senescent HSC (sHSC) do not proliferate anymore and express senescence markers, such as senescent associated beta galactosidase (GLB1), cyclin-dependent kinase inhibitor 2A (Cdkn2a) and Cyclin-dependent kinase inhibitor 1A variant 1 (Cdkn1a). In the fibrotic liver, sHSC accumulate along fibrotic septa and secrete MMPs which degrade the ECM and lead to regression of fibrosis. Moreover, natural killer cells (NK) and liver-specific γδ T cells (NKT) get activated by interferon-gamma (IFNG) and remove activated as well as sHSC. Especially in sHSC, many NK-stimulating genes are upregulated, whereby they become a target for the immune system [87,88].

Besides the activated and senescent phenotype, a new phenotype was detected – the inactivated HSC (iHSC). Transgenic mice were subjected to CCl_4- or

thioacetamide (TAA)- induced liver fibrosis. Subsequently, the mice could recover, and the liver tissue was analyzed. By using genetically labeled cells, it was demonstrated that half of the aHSC do not undergo apoptosis. Instead, they differentiate into an inactivated state. These iHSC are able to react more rapidly to fibrogenic stimuli, revert back to aHSC and contribute again to liver fibrosis [89,90]. Activated HSC are also the major source of MMPs and their physiological inhibitors, the TIMPs [86,7]. MMPs can be subclassified into five groups (gelatinases, collagenases, membrane-type, matrilysins and stromelysins) whereby their effect depends on the tissue and cell type [27]. During liver fibrosis, aHSC secrete MMPs (e.g. MMP-19) which contribute to the matrix turnover. Normal ECM get degraded whereas abnormal ECM accumulate. Furthermore, aHSC secrete TIMP1, which inhibits abnormal ECM-degrading MMPs, such as MMP-9, -12 and -13. This contribute to accumulation of ECM during fibrosis. In contrast, during resolution of liver fibrosis, the amount of aHSC decreases and thus the expression of TIMP1. This leads to active MMPs which degrade collagens and facilitate the resolution of liver fibrosis (Fig. 4) [27,91].

Moreover, macrophages are a crucial part of liver fibrogenesis as well as of the regression of fibrosis. During fibrogenesis, LY6C^{hi} macrophages are recruited via the CC-chemokine ligand 2 (CCL2)-CC-chemokine receptor 2 (CCR2) axis into the liver. There they secrete fibrogenic cytokines and stimulate HSC to differentiate into ECM-producing MF [92]. During regression of liver fibrosis, LY6C^{hi} macrophages switch their phenotype to pro-restorative LY6C^{low} macrophages which secrete the fibrolytic MMP-12 and -13 [93–95]. Furthermore, LY6C^{low} macrophages express TNF-related apoptosis-inducing ligand (TRAIL) and MMP-9 to promote apoptosis of aHSC [96]. The phagocytic capability of macrophages also contributes to resolution of liver fibrosis, as phagocytosis of apoptotic cells stimulate the secretion of MMPs (Fig. 4) [97,98].

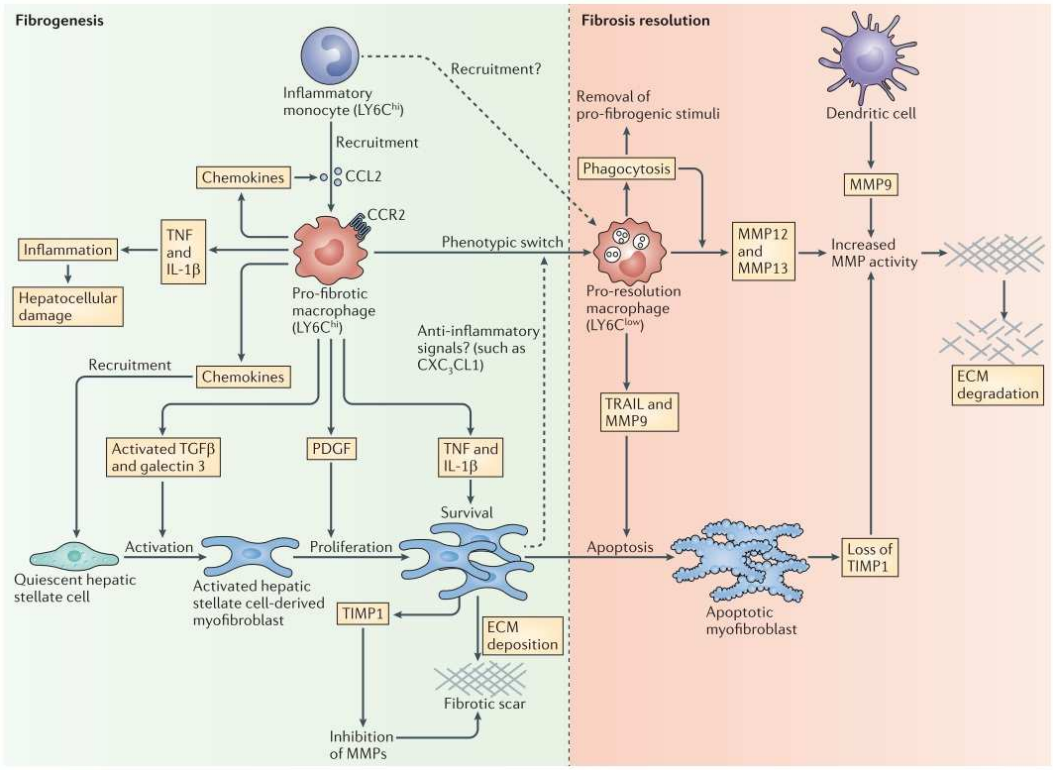

Fig. 4: The dual role of macrophages during liver fibrosis and resolution of liver fibrosis. LY6C^{hi} macrophages are recruited to the liver during fibrogenesis. They secrete fibrogenic cytokines and contribute to the activation of HSC and accumulation of ECM. Instead, during regression of liver fibrosis, they switch to the LY6C^{low} phenotype. These pro-resolutive macrophages induce apoptosis of aHSC and secrete MMPs, which cause degradation of the abnormal ECM. Macrophages can thereby contribute to the regression of liver fibrosis [99].

3.2. Hepatic progenitor cells and the ductular reaction

HPC are bipotential cells and located in the canal of Hering (CoH). In rodent models, they were first described as oval cells because of their oval shaped nucleus and their large nuclear-to-cytoplasm ratio [100,101]. Damages to the liver induce the activation of HPC cells which can transdifferentiate either into cholangiocytes or into hepatocytes. Thereby, they are able to substitute damaged liver tissue [102,103]. The proliferation of HPC is histologically observed as bile duct hyperplasia, the so called DR [104]. Thus the DR correlates with fibrosis stages in chronic liver diseases and is also associated with a portal infiltration of inflammatory cells [105–107].

However, there are controversial opinions about the impact of HPC on liver regeneration. Furuyama *et al*. subjected mice to partial hepatectomy (PHx), BDL and induced liver fibrosis by CCl_4. The authors demonstrated with Cre-based lineage tracing that SOX9$^+$ HPC are located in the CoH and contribute a large part

to new cholangiocytes and hepatocytes [108]. Another study from Shin *et al*. corroborates the impact of HPC in liver regeneration. The authors were able to trace and delete Forkhead Box L1 (FOXL1)-Cre-marked HPC in mice. They subjected these mice to a CDE-induced liver injury and obtained that FOXL1-Cre-marked HPC are necessary for the regeneration of new hepatocytes and cholangiocytes [109]. On the other hand, there are studies which assign HPC only a minor or no contribution to liver regeneration. The group of Malato *et al*. used a hepatocyte-fate tracing mouse model instead of marking progenitor cells. They observed that during normal liver homeostasis and after acute CCl_4 injury, new hepatocytes are generated from proliferating mature hepatocytes. However, their study also shows that 1.3% hepatocytes arrive from HPC after a six weeks CCl_4-treatment [1]. The study of Yanger *et al*. also raises doubts about the contribution of HPC in liver regeneration. The authors marked cholangiocytes and hepatocytes in mice and performed the CCl_4, the PHx, the DDE and the CDE-diet model. In none of their models did HPC contributed to newly generated hepatocytes. Instead, in their study, new hepatocytes and cholangiocytes derived from preexisting hepatocytes. This suggests that hepatocytes could be HPC [110]. This hypothesis is affirmed by Tarlow *et al*. who consider hepatocytes as a potential origin of HPC, as well. By using a chimeric lineage tracing system, the authors demonstrate that hepatocytes transdifferentiate via ductular metaplasia directly into biliary cells. After eliminating the causative agent, these hepatocyte-derived biliary cells return back to hepatocytes and can thereby restore damaged hepatocytes [111]. So far, no specific marker for HPC exists which makes it difficult to determine their contribution to liver regeneration.

The microenvironment around HPC, the so-called HPC niche, is important for the fate of these cells. The HPC niche contains ECM, cytokines and growth factors, which stimulate the activation, proliferation and differentiation of HPC [112]. In chronic liver diseases, the degree of inflammation and fibrosis correlates with the increased amount of HPC [113,114]. During chronic liver damage, HSC gets activated and secrete ECM proteins, which provide a structural network for the HPC niche. These proteins support the differentiation and migration of HPC [115,116]. Furthermore, aHSC release cytokines and growth factors, such as TGFB, TGFA and the hepatocyte growth factor (HGF). Thereby, the proliferation of HPC can be

regulated [117]. Moreover, HPC have regulative features as well. They also secrete growth factors, such as PDGF and TGFB, which -again- leads to a further activation of HSC and an increased deposition of collagens. HPC can thereby promote liver fibrosis [118].

3.3. Regeneration after partial hepatectomy

The remarkable regenerative capacity of the liver becomes clear after a PHx. The original liver mass is restored by proliferation of resident mature hepatocytes from the residual lobes [119]. At the beginning, hepatocytes leave their quiescent state and enter the G1 phase of the cell-cycle. Subsequently, the DNA synthesis (S-phase) and the following mitosis (M-phase) occur. The hepatocytes stop to proliferate as soon as the liver mass is fully restored [120].

After PHx, mesenchymal cells like stellate cells and Kupffer cells, are activated and start to secrete cytokines like HGF, TNF and interleukin-6 (IL6). This triggers the re-entry of hepatocytes into the cell cycle. TGFB is an antiproliferative factor which inhibits the DNA synthesis in hepatocytes. It is assumed that TGFB is the most potent cytokine to stop the regenerative process and enables hepatocytes to switch back to a quiescent state. Unfortunately, the mechanisms explaining the termination of liver regeneration are not fully cleared yet [119,121].

4. The extracellular matrix

The ECM is an active three-dimensional structure of tissues and organs. On the one hand, it preserves the scaffolding of organs and on the other hand, it provides functional features to regulate tissue homeostasis. The ECM consists of proteins, polysaccharides and water, whereby fibrous proteins and proteoglycans are the main macromolecules [122]. Within the group of fibrous proteins, fibronectins, laminins, elastins and especially collagens represent the main components. They facilitate cell migration, mediate cell adhesion and provide the structural meshwork [123,124]. Proteoglycans are composed of a specific protein which is linked to glycosaminoglycan chains (GAG). These hydrophilic molecules are located in the interstitial space, provide the hydrogel formation and regulate cell migration and proliferation as well [125,126]. The ECM continuously undergoes remodeling to maintain tissue homeostasis and protects the organ. As a result of hepatic injury,

ECM is increasingly produced by MF as part of the wound-healing response of the liver. In case of a chronic or severe liver damage, this leads to an excessive accumulation of ECM and causes hepatic fibrosis [2,122]. Two of the highly upregulated ECM proteins during liver fibrosis are the glycoproteins POSTN and TNC [127,128].

4.1. Periostin

POSTN is a 90 kDa nonstructural ECM protein and belongs to the fasciclin family. It was originally identified in mouse osteoblastic cells and renamed because in adult mice POSTN is primary expressed in the periodontal ligament and periosteum. The protein structure consists of a signal peptide (SP), followed by an amino-terminal emilin (EMI) domain, four fasciclin (FAS 1) domains and a carboxyl-terminal domain (CTD) which contains proteolytic cleavage sites and splicing occurs (Fig. 5) [129–131]. The EMI domain enables POSTN to interact with Fibronectin, Notch 1 and Collagen I [132–134]. The FAS 1 domains provide the interactions with BMP-1 and TNC [133,135]. Under physiological conditions, POSTN is only low expressed whereas in response to chronic or severe tissue damage as well as in inflammatory diseases, POSTN expression is upregulated. Fibrogenic and pro-inflammatory cytokines, such as TGFB1, PDGF, fibroblast growth factors, stimulate the secretion of POSTN [132,136]. POSTN is involved in many different diseases and therefore plays an important role in tissue homeostasis and remodeling. It contributes to fibrosis in many organ systems. In the lung, POSTN secrets cytokines to recruit inflammatory cells and promotes idiopathic pulmonary fibrosis (IPF) [137]. In the heart, the POSTN expression correlates with myocardial fibrosis and promotes rheumatic and atherosclerotic cardiac valve degeneration by production of MMPs and inducing angiogenesis [138–140]. Moreover, POSTN is upregulated in the renal tissue after glomerular injury [141]. Besides fibrotic processes, POSTN is also essential for regenerative processes in organs. After an acute pancreatitis, it is crucial for a successful regeneration of the exocrine pancreas [142]. Recent studies indicate that POSTN could also play an important role in liver fibrosis and regeneration. Its expression is upregulated in patients with acute or chronic hepatitis as well as in mice with liver fibrosis [143,144].

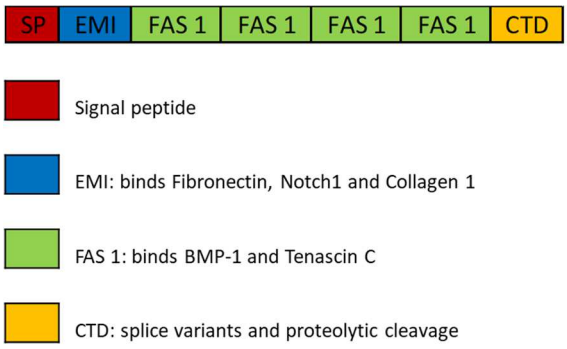

Fig. 5: The protein structure of Periostin. POSTN is a 90 kDa matricellular protein, which consists of a signal peptide, an EMI domain, four FAS 1 domains and one CTD.

4.2. Tenascin C

TNC is a hexametric ECM protein and belongs to the tenascin gene family. It was identified independently by different working groups and each laboratory gave TNC a different name, such as glioma mesenchymal extracellular matrix antigen (GMEM), Myotendinous antigen or Cytotactin [145–147]. In 1986, Chiquet-Ehrismann *et al*. introduced the name Tenascin C. It arises from the latin words "*tenere*" (to hold), which reflects its prominently location in tendons and from "*nasci*" (to be born), which reflects its impact in embryonic development. The C arise from the former name Cytotactin [148]. TNC has a hexametric protein structure which can be highly modulated by alternative splicing and enables TNC to interact with many binding partners (Fig. 6). Each of the six arms contains an amino-terminal Tenascin assembly (TA) domain where the oligomers can be linked together by coiled-coil interaction in the HEPTAD region [149]. Following the HEPTAD region, 13 epidermal growth factor-like (EGFL) repeats are present which are required for cell adhesion to fibroblasts, glia cells and neurons [150,151]. After the EGFL repeats, multiple alternative-spliced Fibronectin-III (FN-III) domains are connected. The splicing of the FN-III affect the size of TNC which range from 180-250 kDa [152]. Furthermore, the FN-III domains are an elastic region which enables TNC to stretch and fold [153]. Adjacent to these domains, the C-terminal end contains a calcium-binding fibrinogen globe. TNC can thereby interact with other ECM proteins and regulate cell adhesion, proliferation and migration [154,155]. Under physiological conditions, TNC is only low expressed in the adult organism, preferentially in tissue which is exposed to high tensile stress [156]. In response to tissue damage and pathological

conditions, such as inflammatory processes and cancer, the expression of TNC is upregulated and impairs tissue homeostasis and remodeling [157–159]. Numerous cytokines, such as TGFB and PDGF, induce the secretion of TNC which contributes to wound-healing and fibrosis in different organ systems [160,161]. In the lung, TNC is especially expressed in the early inflammatory response and therefore modulates wound-healing and promotes fibrosis [162,163]. Furthermore, TNC promotes myocardial fibrosis and thus also cardiac dysfunction [10]. TNC expression is upregulated during chronic pancreatitis and pancreatic ductal adenocarcinoma (PDAC) [164]. As part of the wound-healing process in the liver, TNC influences the migration of HSC and promotes the secretion of collagen I. It upregulates cytokine secretion to enhance the inflammatory response and ultimately promotes liver fibrosis [165,166].

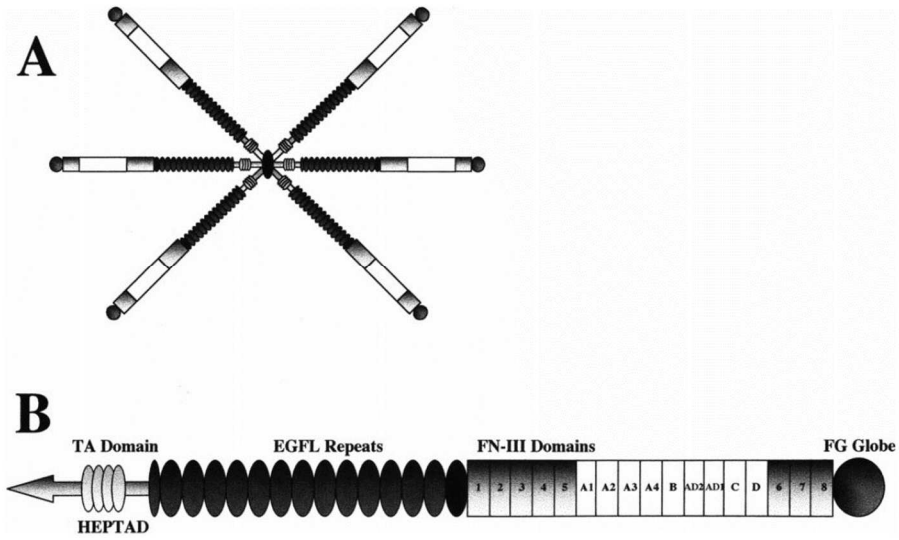

Fig. 6: The protein structure of Tenascin C. A: The hexametric structure of TNC. B: One oligomer. Six oligomers are linked together at their TA domain. The following EGFL are required for cell adhesion. Alternative spliced FN-III domains enable TNC to stretch and fold and effect the size of it. The FG globe at the end facilitates the communication with other ECM molecules [167].

5. Mouse models for experimental liver fibrosis and regeneration

The mechanisms of the complex interactions of hepatic cells during liver fibrosis and regeneration are not fully understood yet. Therefore, experimental animal models are needed to study and understand the mechanisms. Recent studies

demonstrate that different mouse strains are differently susceptible to carbon tetrachloride (CCl_4)-induced and diet-induced liver damage [168,169]. This suggest that the genetic background could also have an impact on the cholestatic-induced liver fibrosis and on the regeneration process. Therefore, it is recommended to use animals with the same genetic background in the experiments.

5.1. The bile duct ligation model

The BDL is the most used model to induce a cholestatic liver damage in mice. It provides a deep insight in the mechanisms of bile acid mediated inflammation and the resulting liver fibrosis. In this model, the common bile duct is double ligated [170]. Bile acids, the major component of the bile and different metabolites (e.g. bilirubin and drug metabolites), are secreted by hepatocytes. Under normal conditions, the bile reaches the duodenum via the bile duct. As an emulsifier, it enables the absorption and digestion of fat and fat-soluble vitamins. Via the enterohepatic circulation 95% of the bile acids are transported back to the liver where the potentially toxic metabolites are excreted. After the surgical ligation of the bile duct, the disrupted bile flow leads to an increase of these bile components in the liver and subsequently causes hepatocellular damage [171–173]. After three to four weeks, a strong portal fibrosis with porto-portal septa has evolved in mice [170].

5.2. The carbon tetrachloride model

The CCl_4 model is the most used model to induce a toxic liver fibrosis in mice. The hepatotoxin CCl_4 can be administered by gavage, inhalation or by intra peritoneal (i.p.) injections. Especially i.p. injections are easy and fast to perform and provide exact analyses of liver tissue at certain time points. Furthermore, this model can also be used as a regeneration model because the liver regenerates after completion of the CCl_4 treatment [174]. Regardless of the way of administration, CCl_4 is metabolized in the liver. Cytochrome P450 activates CCl_4 to trichloromethyl radical (CCl_3*), which causes peroxidation of lipids, hypomethylation of proteins as well as mutations in nucleic acids. CCl_3* thereby causes a reduced protein synthesis and induces hepatocellular injury. Moreover, the oxygenation of CCl3* to trichloromethylperoxy radicals (CCl_3OO*) lead to further peroxidation of lipids and a reduced membrane permeability. This leads to inflammation with resulting

liver fibrosis and can even cause HCC [175].

The CCl_4 model induces necroses of centrilobular hepatocytes resulting in a pericentral fibrosis with centro-central septa [176]. It is recommended to applicate CCl_4 by i.p. injections. The standard treatment is 0.5-0.7 mL/g mouse weight CCl_4, solved in corn oil, two times per week for six weeks or three times per week for four weeks. The application by gavage lead to a high mortality rate. The application by inhalation requires more equipment and the CCl_4 vapors are toxic for humans and are therefore not recommended [174]. The genetic background has an influence on the fibrogenesis. The susceptibility for liver fibrosis depends on the mouse strain. FVB/N mice show only a weak fibrotic reaction whereas BALB/c mice are highly susceptible to CCl_4-mediated liver fibrosis. C57BL/6 are the most frequently used mice because of the large selection of genetically-modified strains, even if they demonstrate only an intermediate susceptibility to CCl_4-related fibrosis [177,178].

5.3. The partial hepatectomy model

The PHx is the most used model to study the regenerative liver growth. It provides a deep insight in the mechanism of liver regeneration as well as a deeper understanding of the involved signaling pathways. In this model, two-third (70%) of the liver is removed: the left lateral lobe and the left and right median lobe. The original liver mass is restored within one week by proliferating hepatocytes of the residual lobes [179,180].

The gender, the age and the genetic background of mice have an influence on the regeneration process. Female mice have a significant decreased or delayed proliferation of hepatocytes and restoration of the liver mass [181]. Furthermore, the regenerative capability decreases with increasing age of rodents. Younger animals show higher levels of pro-restorative cytokines, such as IL6 [182].

II. AIM OF THE STUDY

Severe or chronic liver damage causes liver fibrosis and can ultimately lead to cirrhosis and HCC. Thereby, HSC and other MF are activated and secrete excessively ECM. The accumulation of the ECM leads to fibrous scarring and distorts the normal liver architecture [2]. Besides the fibrotic reaction, severe liver damage leads to an activation of HPC. These bipotential cells proliferate and can transdifferentiate either into cholangiocytes or hepatocytes, which can histologically be observed as DR [1,183]. The ECM provides on the one hand structural features, on the other hand it forms a special microenvironment around HPC to affect their fate [122].

In this study, the functional role of POSTN and TNC during liver damage and regeneration will be analyzed by using three different mouse models. First, it will be clarified weather POSTN and TNC contribute to liver fibrosis. Is their influence dependent on the time and on the causative agent? Next, the influence of POSTN and TNC on the DR and the fate of HPC will be characterized. As part of the HPC-niche they might have an impact on the proliferation and dedifferentiation of HPC to promote liver regeneration. Furthermore, possible compensatory effects of these two ECM proteins should be investigated. Does the loss of one ECM protein lead to a compensatory increase of another one?

The results of our study will reveal if POSTN and TNC play a role in liver damage and regeneration. Our study elucidates the function of POSTN and TNC in the HPC-niche and contribute to a better understanding of their role during the fibrotic and regenerative process in the liver.

III. MICE, MATERIALS AND METHODS

1. Mice

Experimental procedures as well as the maintenance of the animals were carried out in accordance to the German Animal Welfare Act and were approved by the State Office for Nature, Environment and Consumer Protection (Landesamt für Natur; Umwelt und Verbraucherschutz, LANUV) of North Rhine-Westphalia (approval numbers: 84-02.04.2018.A212 and 81-02-04-2018.A149).

1.1. Laboratory mouse strains

For this project POSTN-deficient, TNC-deficient and control mice were used. All mice were bred and housed in the animal facility of the central Unit for Animal Research and Animal Welfare Affairs (Zentrale Einrichtung für Tierforschung und wissenschaftliche Tierschutzaufgaben, ZETT). Knockout and control mice were generated from crossing the corresponding heterozygote mice.

1.1.1. Periostin$^{-/-}$ mice

The mouse strain C57BL/6J;Cg-Postn^{tm1Jmol}/J was originally purchased from Jackson Laboratory (Bar Harbor, ME, USA) and generated by replacing exon 4-10 of the Periostin gene through a neomycin resistance cassette [184]. The extracellular matrix protein POSTN is overexpressed during inflammation, tissue regeneration and other pathological conditions [185]. Therefore, Postn$^{-/-}$ mice were originally used for cardiological research. They showed less fibrosis after a myocardial infarction and also less fibrosis after long-term pressure overload [186].

1.1.2. Tenascin C$^{-/-}$ mice

The mouse strain C57BL/6J;Cg-TgH(Tnc) was originally purchased from RIKEN BioResource Research Center (3-1-1 Koyadai, Tsukuba, Ibaraki 305-0074, Japan) and generated by replacing exon 2 by a lacZ gene and a neomycin resistant cassette [187]. TNC is upregulated during different pathological conditions, such as cancer and chronic inflammation [128] For this reason, Tnc$^{-/-}$ mice are often used in studies about carcinogenesis, tissue regeneration and wound healing [164,188].

1.2. Housing conditions

All mice used for the *in vivo* experiments were kept in specific pathogen-free air-conditioned rooms at 20-24 °C with a twelve-hour day night cycle and a relative humidity of 50-60%. All over the time, the mice had *ad libitum* access to feed (ssniff Spezialdiäten GmbH, Soest, Germany) and water. They were housed in conventional cages with a maximum occupancy of three mice per type II cage or of six mice per type II long cage. According to the FELASA guidelines, the health status was quarterly monitored [189]. This was negative at all timepoints for the relevant pathogens.

1.3. Genotyping of the mouse strains

1.3.1. DNA extraction

DNA from each mouse was extracted from tail tips or a punch of ear. Therefore, each piece of tissue was incubated with 500 µl saline Tris-EDTA (STE) buffer at 40 °C over night. On the next day, the lysate was centrifuged for 5 minutes at 10.000 x g and the supernatant was transferred into a new tube. 350 µl isopropanol was added, mixed gently, and centrifuged for 20 min at 14.000 x g at 4 °C. Subsequently, the supernatant was decanted carefully, and the residual pellet was washed with 500 µl ethanol absolute. The lysate was centrifuged for 10 minutes at full speed at 4 °C. The supernatant was carefully removed with a pipette and the pellet was dried at 37 °C in a heating block until the ethanol was completely evaporated. The DNA pellet was dissolved in 50 µl ddH_2O. The concentration was measured photometrically and, if necessary, diluted for further PCR analysis.

1.3.2. Polymerase chain reaction (PCR)

Following the DNA extraction, the genotype was determined by performing the corresponding PCR.

For the PCR, a 20 µl reaction was set as following:

Mastermix (2x):	10 µl
Each Primer (100 pM):	1 µl
Genomic DNA:	20-100 ng
ddH_2O:	adjust to 20 µl

The amplification parameters were set as following:

POSTN PCR:	TNC PCR:
94 °C 1 min initial denaturation	94 °C 3 min initial denaturation
40 cycles with:	40 cycles with:
94 °C 30 sec denaturation	94 °C 30 sec denaturation
58 °C 30 sec annealing	55 °C 30 sec annealing
72 °C 1 min elongation	72 °C 45 sec elongation
72 °C 10 min final elongation	72 °C 10 min final elongation

Each PCR set includes a positive and a negative control. The amplification product was visualized by gel electrophoresis on 1.8% agarose gel. The gel was run at 100 V including a ladder with 100 bp and images were taken with a gel documentation system.

2. Materials

Unless indicated, the companies or distributors are based in Germany.

2.1. Reagents

Acetic acid	VWR International GmbH, Darmstadt
Albumin Fraktion V	Carl Roth GmbH + Co. KG, Karlsruhe
DAB Substrate Kit	Abcam plc, Cambridge (UK)

Dulbecco's PBS	Merck KGaA, Darmstadt
EDTA	Carl Roth GmbH + Co. KG, Karlsruhe
Eosin Y	Merck KGaA, Darmstadt
Ethanol 70%	VWR International GmbH, Darmstadt
Ethanol 99.5% denatured with 1% MEK	VWR International GmbH, Darmstadt
Eukitt® Quick-hardening mounting medium	Merck KGaA, Darmstadt
Formaldehyde solution 4% phosphate buffered	neoFroxx GmbH, Einhausen
GeneRuler 100 bp Plus DNA Ladder	Thermo Fisher Scientific, Waltham (USA)
Isopropanol	Merck KGaA, Darmstadt
Mayer's hemalum solution	Merck KGaA, Darmstadt
Movat Pentachrome (Verhöff) StainKit	MORPHISTO GmbH, Frankfurt am Main
Normal Goat Serum	Abcam plc, Cambridge (UK)
Parrafin	Engelbrecht GmbH, Edermünde
peqGREEN 20 000X DNA/RNA binding dye	VWR International GmbH, Darmstadt
Picro Sirius Red Stain Kit	Abcam plc, Cambridge (UK)
Power SYBR Green Mastermix	Thermo Fisher Scientific, Waltham (USA)
Proteinase K	Thermo Fisher Scientific, Waltham (USA)
REDTag® ReadyMix™ PCR Reaction Mix	Sigma-Aldrich Chemie GmbH, Steinheim
RevertAid First Strand cDNA Synthesis Kit	Thermo Fisher Scientific, Waltham (USA)
RNEasy Mini Kit	Qiagen GmbH, Hilden
Sodium Chloride	Merck KGaA, Darmstadt

Tri-Sodium Citrate 2-hydrate	Carl Roth GmbH + Co. KG, Karlsruhe
TRIS	Carl Roth GmbH + Co. KG, Karlsruhe
Tween® 20	Merck KGaA, Darmstadt
Xylene	VWR International GmbH, Darmstadt

2.2. Buffer

Blocking Solution:

BSA	1% in PBS
Goat serum	10%
Triton-X	0.1%

Citrate buffer:

Citric acid	10 mM
pH 6.0	

TE buffer:

Tris	10 mM
EDTA	1 mM
pH 9.0	

STE buffer:

TRIS	50 mM
NaCl	100 mM
EDTA	100 mM
SDS	1%
Proteinase K	0.5mg/ml

TAE (50x):

TRIS	2 M
EDTA	50 mM
Acetic acid	1 M
pH 8.0	

TBS (10x):

TRIS	250 mM
NaCl	1400 mM
pH 7.6	

2.3. Consumables

Coverslips 24 x 50 mm	Engelbrecht GmbH, Edermünde
Centrifuge tubes 15mL, 50 mL	Greiner Bio-One International GmbH, Kremsmünster (A)
Cryo Rack	Greiner Bio-One International GmbH, Kremsmünster (A)
Cryo.s™ 2mL	Greiner Bio-One International GmbH, Kremsmünster (A)
Embedding cassettes	R. Langenbrinck GmbH, Emmendingen
FEATHER® Microtome Blade A35	pfm medical ag, Köln
MicroAMP™ Optical 96-Well Reaction Plate	Thermo Fisher Scientific, Waltham (USA)
Reaction tubes 1.5 mL, 2.0 mL	SARSTEDT AG & Co. KG, Nümbrecht
StarFrost Advanced Adhesive microscope slides	Engelbrecht GmbH, Edermünde
TipOne® 10µL, 100µL, 1000µL	STARLAB International GmbH, Hamburg

2.4. Antibodies and detection systems

Anti-ACTA2 (ab5694)	Abcam plc., Cambridge (UK)
Anti-MKI67 (550609)	BD Transduction Laboratories, Heidelberg
Anti-POSTN (ab14041)	Abcam plc., Cambridge (UK)
Anti-SOX9 (AB5535)	Merck, Damrstadt
Anti-TNC (ab108930)	Abcam plc., Cambridge (UK)
Anti-TROMA III (K1C19)	DSHB, Iowa (USA)
VECTASTAIN® ABC HRP Kit (Peroxidase, Mouse IgG)	Vector Laboratories Inc., Burlingame (USA)
VECTASTAIN® ABC HRP Kit (Peroxidase, Rabbit IgG)	Vector Laboratories Inc., Burlingame (USA)
ZytoChem Plus (HRP) One-Step Polymer anti-Mouse/Rabbit/Rat	Zytomed Systems, Berlin

2.5. Primer

Primer sequences used for *Postn* genotyping:

Periostin (fwd)	5’-CCT TGC CAG TCT CAA TGA AGG-3’
Periostin wildtype (rev)	5’-TGA CAG AGT GAA CAC ATG CC-3’
Periostin knockout (rev)	5’-GGA AGA CAA TAG CAG GCA TGC TG-3’

Primer sequences used for *Tnc* genotyping:

Tenascin C (fwd)	5’-CTC AGA TCC GAA GCT GCG ATA C-3’
Tenascin C wildtype (rev)	5’-GTT GAA CAC CAC TGG CTG ATT CT-3’
Tenascin C knockout (rev)	5’-CTC CAT GCT TGG AAC AAC GA-3’

Primer sequences used for qRT-PCR:

Name	Primer fwd (5’ → 3’)	Primer rev (3’ → 5’)
Postn	CACGGCATGGTTATTCCTTCA	AGGGTCTGGGCCATAGAACT

Tnc	AACGGACTGCCCACATCTCA	TTCCGGTTCAGCTTCTGTGGTA
Acta2	CTGTCAGGAACCCTGAGACGC	GGATGGGAAAACAGCCCTGG
K1c19	CCCAGGTCGCCGTCCACTCTGAGCA	GCGTGCCTTCCAGGGCAGCTTTCATGC
Sox9	GCAAGCTGGCAAAGTTGATCT	GCTGCTCAGTTCACCGATG

2.6. *In* vivo experiments

STERICAN needles 20 G, 27 G	B. Braun Melsungen AG, Melsungen
Aesculap GT421 "Isis"	Albert Kerbl GmbH, Buchbach
Bepanthen® ointment	Bayer Vital GmbH, Leverkusen
Carbon tetrachloride	Sigma-Aldrich Chemie GmbH, Steinheim
Coated VICRYL™; 5-0; Type: V396H	Ethicon, Norderstedt
Conventional cages Type II and Type II long	Tecniplast Deutschland GmbH, Hohenpeißenberg
Dräger Sulla 800V	Drägerwerk AG & Co. KGaA, Lübeck
Feed	Sniff Spezialdiäten GmbH, Soest
Infrared lamp "IL30"	Beurer GmbH, Ulm
Injekt® -F 1mL, 2mL, 5 mL	B. Braun Melsungen AG, Melsungen
Isofluran CP	CP-Pharma Handelsgesellschaft mbH, Burgdorf
Kodan® paint forte	Schülke & Mayr GmbH, Norderstedt
Minitag	TEM SEGA, Pessac (France)
NaCl 0.9%	Fresenius Kabi Deutschland GmbH, Bad Homburg
Novaminsulfon 500mg Lichtenstein	Zentiva Pharma GmbH, Frankfurt am Main
Omnifilm® tape	PAUL HARTMANN AG, Heidenheim
Rimadyl® 50mg/ml injection solution	Zoetis Deutschland GmbH, Berlin
Sempermed® supreme surgical gloves	Lohmann & Rauscher GmbH & Co. KG, Neuwied

Steuergerät HT10 heating pad	Minitüb GmbH, Tiefenbach
Surgical instruments	Fine Science Tools GmbH
Vicryl™; 5-0; Type: V632H	Ethicon, Norderstedt

2.7. Laboratory equipment

Embedding Center "TES 4004"	pfm medical ag, Köln
Eppendorf Bio-Photometer 6131	Eppendorf AG, Hamburg
Eppendorf Centrifuge 5417R	Eppendorf AG, Hamburg
Eppendorf Research Pipetten	Eppendorf AG, Hamburg
Flex Cycler	Analytik Jena AG, Jena
HM430 Sliding Microtome	Thermo Fisher Scientific, Waltham (USA)
IKAMAG® RCT	IKA®-Werke GmbH & CO. KG, Staufen
Mixing Block MB-102	Biozym Scientific GmbH, Hessisch Oldendorf
Pap pen	DCS Innovative Diagnostik-Systeme, Hamburg
pH meter HI2020 edge®	Hanna Instruments Deutschland GmbH, Vöhringen
PowerPac™ 300 Power Supply	Bio-Rad Laboratories GmbH, Feldkirchen
Precision balance PCB 2500-2	KERN & SOHN GmbH, Balingen
QUANTUM ST5 geldocumentation	PEQLAB, VWR International GmbH
ROMMELSBACHER THS 2022/E cooking plate	ROMMELSBACHER ElektroHausgeräte GmbH, Dinkelsbühl
Sakura Tissue-Tek® Film™ "Film-E2"	Sakura Finetek Germany GmbH
Sakura Tissue-Tek® Prisma™ "Prisma-E2S"	Sakura Finetek Germany GmbH
StepOnePlus™ Real-Time PCR System	Thermo Fisher Scientific, Waltham (USA)
Sub-Cell GT Cell	Bio-Rad Laboratories GmbH, Feldkirchen
TissueLyser LT	Qiagen GmbH, Hilden

Tissue-Tek® VIP™ "VIP-5E-F2"	Sakura Finetek Germany GmbH
Universal oven U75	Memmert GmbH + Co. KG, Schwabach
Vitaquick® pressure cooker	Fissler GmbH, Idar-Oberstein
Vortex Genie 2	Bender & Hobein AG, Zurich (Switzerland)
Warm water bath	LABORTECHNIK GmbH+Co. KG, Lonsee-Ettlenschieß
Zeiss Axioskop 2 plus	Carl Zeiss Microscopy GmbH, Jena

2.8. Software

GraphPad Prism 7	GradPad Software Inc., San Diego (USA)
Mendeley	Elsevier B.V., Amsterdam (Netherlands)
Microsoft Office 365	Microsoft, Redmond (USA)
ZEISS ZEN	Carl Zeiss Microscopy GmbH, Jena

3. Methods

3.1. Mouse models

Three different mouse models were used to induce liver damage, fibrosis or to initialize the regeneration process. The BDL was used to induce a cholestatic-obstructive liver fibrosis. The CCl_4 model was used to induce a toxic damage resulting in liver fibrosis as well as to study liver regeneration. The third model was performed to study the regenerative process after PHx. All *in vivo* experiments were performed at the ZETT.

3.1.1. The bile duct ligation model

The induction of the cholestatic-obstructive liver damage was caused by the ligation of the common bile duct [170]. Therefore, twelve weeks old male $Postn^{-/-}$, $Tnc^{-/-}$ and control mice received 5 mg/kg body weight Carprofen s.c. 30 minutes before the operation. The anesthetization was performed by using the gas anesthesia table Minitag (TEM SEGA) with inhalation Isoflurane (3-4%) in 100%

oxygen (5 L/min). The abdomen was shaved with an electric fur shaver, sanitized and eye ointment were used to protect the cornea from drying out. The mice were fixed on a heating pad (37 °C) with tape. The maintenance of the inhalation anesthesia was carried out with the help of a mask, connected to the anesthetic machine with 1-2% Isoflurane in 100% oxygen (1L/min). The abdomen was opened with a laparotomy along the *linea alba*. To keep the peritoneal cavity open, two serrefines were used. The liver was lifted with a cotton swab so that it adhered to the diaphragm and the hilum was visible. The bile duct was carefully isolated from the hepatic artery and the portal vein by using a blunt tweezer. Afterwards, the bile duct was ligated twice by using two surgical knots. After cutting the ends of the suture, the peritoneal cavity was rinsed with 0.9% NaCl solution and the serrefines were removed. The peritoneum and the abdominal muscles as well as the skin were closed with running sutures. At the end of the operation, the skin was cleaned with a moisturized, sanitizing cotton swab and the mouse turned back into its cage. It received infrared light until it was fully awake. All mice received 5 mg/kg body weight carprofen two times per day for three days after the operation. The sham operated mice were treated like the operated ones, just without the ligation of the bile duct (Fig. 7).

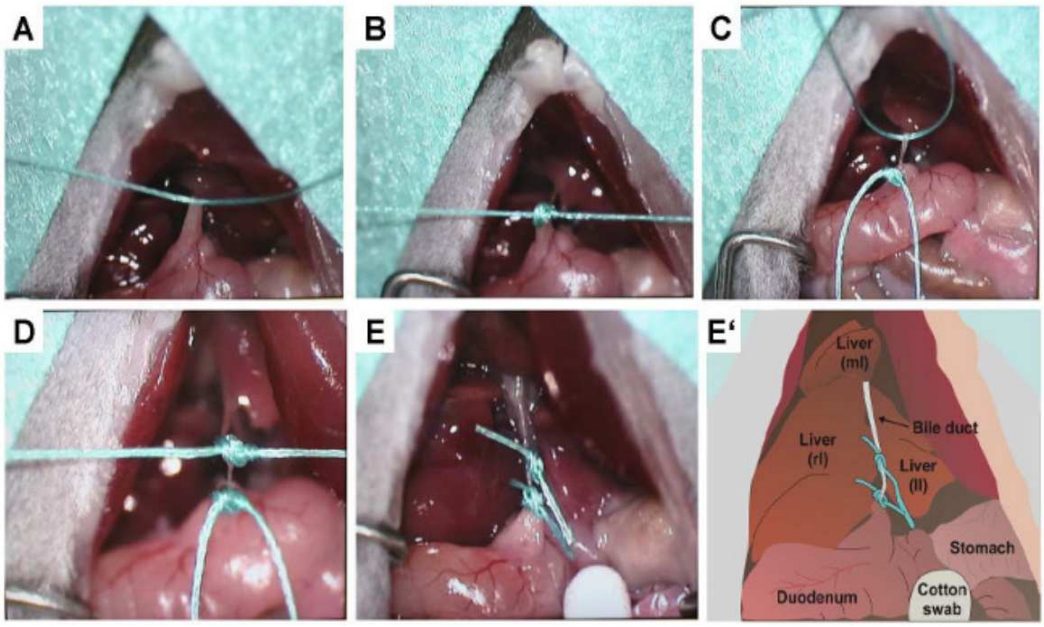

Fig. 7: Practical implementation of the BDL in mice. A: The liver is lifted and adheres to the diaphragm. The bile duct is separated with the suture. B: The first ligature of the bile duct. C & D: Knotting of the second ligature. E & E´: Double-ligated bile duct and cut ends

of the suture [170].

The mice were euthanized 3, 7 or 21 days after the BDL by cervical dislocation. The sham operated mice were euthanized 21 days after the operation. The liver was removed, photographed, and weighted. The distal half of the right lobe was cut into small pieces, snap frozen in liquid nitrogen, and stored at -80 °C. The remaining liver was fixated in 4% buffered formaldehyde solution. After a fixation time of 48 to 72 hours, the tissue samples were subsequently dehydrated and embedded in paraffin. Five to six mice were used in each experimental group (Tab. 1).

Tab. 1: Number of mice used in the BDL model.

	Ctrl	Postn$^{-/-}$	Tnc$^{-/-}$
3 days	6	5	6
7 days	6	6	6
21 days	6	6	6
sham	6	6	6

3.1.2. The carbon tetrachloride model

The induction of a toxic liver damage was caused by intraperitoneal injections of CCl_4 [174]. Therefore, ten weeks old male Postn$^{-/-}$, Tnc$^{-/-}$ and control mice received 0.7 mL/kg body weight CCl_4 diluted in 50 µl corn oil two times per week. The injection solution was applied i.p. at room temperature by using sterile syringes and 27G needles. All mice received oral Metamizol (150 mg/kg body weight) 30 minutes before the CCl_4 injection. The sham group received only corn oil as an injection solution. In consideration of the fact that the liver starts to regenerate after the CCl_4-treatment, this model was used for two experimental groups: the CCl_4 "Fibrosis" and the CCl_4 "Regeneration" group.

3.1.2.1. CCl_4 "Fibrosis" group

The CCl_4 "Fibrosis" group was treated for 2, 4 or 8 weeks to induce a mild to severe fibrosis. The sham group was treated for 8 weeks. After the treatment, the mice were euthanized by cervical dislocation. The liver was removed, photographed, and weighed. The liver lobes were separated from each other. One part from each

liver lobe was collected and reduced to small pieces. Subsequently, they were snap frozen in liquid nitrogen and stored at -80 °C. The remaining liver lobes were fixated in 4% buffered formaldehyde solution. After a fixation time of 48 to 72 hours, the tissue samples were subsequently dehydrated and embedded in paraffin. Three to six mice were used in each experimental group (Tab. 2).

Tab. 2: Number of mice used in the CCl_4 "Fibrosis" group.

	Ctrl	Postn$^{-/-}$	Tnc$^{-/-}$
2 weeks	5	5	5
4 weeks	5	5	5
8 weeks	6	6	5
sham	6	3	3

3.1.2.2. CCl_4 "Regeneration" group

The mice of the CCl_4 "Regeneration" group were treated for 12 weeks and subsequently allowed to regenerate for different time points. Therefore, the mice were euthanized either 7, 14 or 21 days after the last CCl_4 injection by cervical dislocation. Mice of the sham group were euthanized 21 days after the last corn oil injection. The liver was sampled and trimmed just as in the CCl_4 "Fibrosis" group. Four to six mice were used in each experimental group (Tab. 3).

Tab. 3: Number of mice used in the CCl_4 "Regeneration" group.

	Ctrl	Postn$^{-/-}$	Tnc$^{-/-}$
7 days	6	5	6
14 days	6	4	5
21 days	6	4	5
sham	6	6	6

3.1.3. The partial hepatectomy model

The regenerative capacity of the liver was studied by performing the two-thirds PHx. Therefore 70% of the liver was removed in 10 to 16 weeks old male control, Postn$^{-/-}$ and Tnc$^{-/-}$ mice. All mice received 5 mg/kg body weight Carprofen s.c. 30 minutes before the operation. The anesthetization was performed by using the gas anesthesia table Minitag (TEM SEGA) with inhalation Isoflurane (3-4 %) in 100% oxygen (5 L/min). The abdomen was shaved with an electric fur shaver,

sanitized and eye ointment were used to protect the cornea from drying out. The mice were fixed on a heating pad (37 °C) with tape. The maintenance of the inhalation anesthesia was carried out with the help of a mask, connected to the anesthetic machine with 1-2% Isoflurane in 100% oxygen (1 L/min). The abdomen was opened with a laparotomy along the *linea alba*. To keep the peritoneal cavity open, two serrefines were used. The falciform ligament was cut through to facilitate a more flexible liver. Subsequently, a suture loop was placed around the right median lobe. The knot was put as close to the base of the lobe as possible. The ligature was pulled tight whereby the liver parenchyma was cut through. In this way, the suture ligated the vessels and biliary ducts. After making a tight knot, the liver lobe was gently removed, and the suture ends were cut. The next suture loop was placed around the left median lobe and tighten close to the base of the lobe. The liver tissue and the suture ends were removed close to the ligature. The third suture loop was placed around the left lateral lobe. Similarly, the last liver lobe was removed (Fig. 8). After the resection of each lobe, possible bleeding points were stopped by using a cotton swab. Subsequently, the peritoneal cavity was rinsed with 0.9% NaCl solution and the serrefines were removed. The peritoneum and the abdominal muscles as well as the skin were closed with running sutures. At the end of the operation, the skin was cleaned with a moisturized, sanitizing cotton swab and the mouse turned back into her cage. It received infrared light until it was fully awake. All mice received 5 mg/kg carprofen two times per day for three days after the operation. The sham operated mice were treated like the operated ones, just without the resection of the liver lobes.

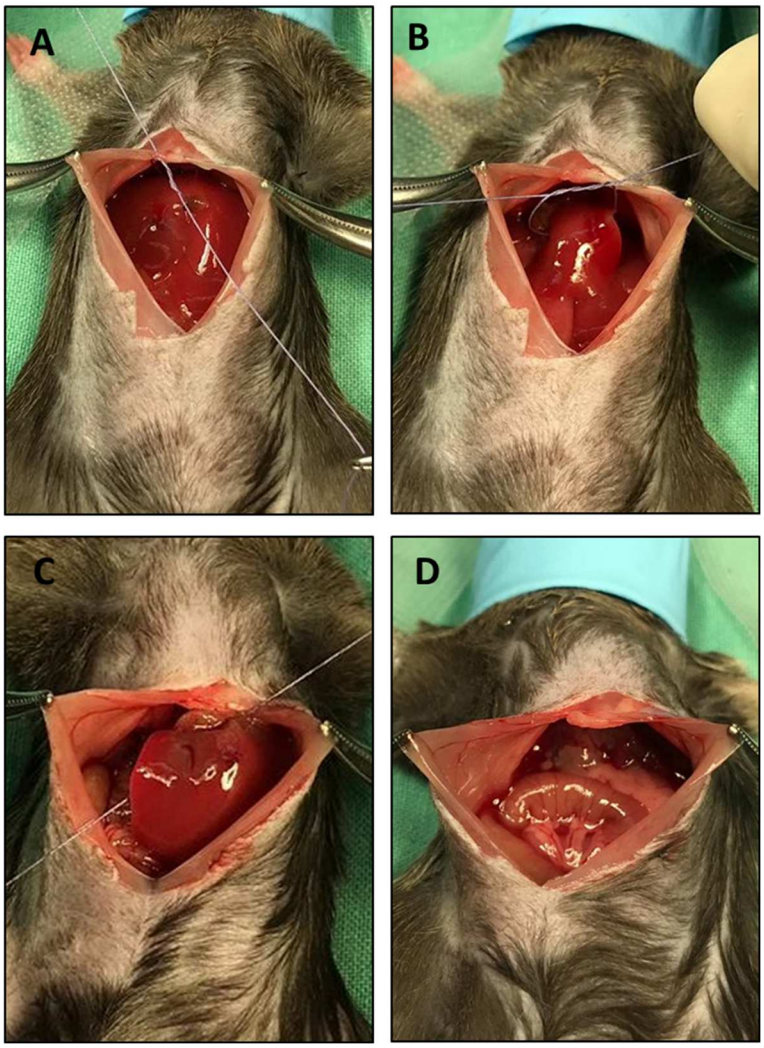

Fig. 8: The partial hepatectomy in mice. A: First ligature around the right median lobe. B: Second ligature around left median lobe. C: Third ligature cut through the parenchyma of the left lateral lobe. D: Peritoneal cavity after resection of the liver lobes.

The mice were euthanized 4, 8, 14 or 21 days after the partial hepatectomy by cervical dislocation. The sham operated mice were euthanized 21 days after operation. The liver was removed, photographed, and weighed. The distal half of the caudate lobe was cut in small pieces, snap frozen in nitrogen, and stored at -80 °C. The remaining liver lobes were separated from each other, the right lobe was additionally cut in 2 pieces and fixated in 4% buffered formaldehyde solution. After a fixation time of 48 to 72 hours, the tissue samples were subsequently dehydrated and embedded in paraffin. Four to six mice were used in each experimental group (Tab. 4).

Tab. 4: Number of mice used in the PHx model.

	Ctrl	Postn$^{-/-}$	Tnc$^{-/-}$
4 days	6	6	6
8 days	6	6	6
14 days	6	6	6
21 days	6	6	6
sham	6	4	4

3.2. Histology

For histological analysis of the liver, microscope slides were produced. Therefore, formalin fixed paraffin embedded (FFPE) tissue was cut with the microtome into 2 µm thick sections and carefully transferred to a warm water bath. Afterwards, they were mounted on microscope slides and dried at room temperature. Finally, the slides were fixated at 60 °C at the dry incubator for one hour directly before staining. For short term storage the slides were kept at 4 °C. For the evaluation of the liver tissue, different scoring systems were established for each staining.

3.2.1. Histological stainings

Different histological stainings were performed for a semiquantitative evaluation of the degree of inflammation and stage of fibrosis. The grading, the determination of the degree of inflammation, was performed by using the Hematoxylin-Eosin staining. The staging, the determination of the fibrosis stage, was performed by using the Movat Pentachrome and the Picro Sirius Red staining.

3.2.1.1. Hematoxylin-Eosin staining

The Hematoxylin-Eosin staining was performed to get an overview of the extent of liver damage and to evaluate the degree of inflammation. The staining was performed automatically with the Sakura Tissue-Tek®Prisma™ system. Therefore, sections of FFPE tissue mounted on microscope slides were deparaffinized in xylol, rehydrated in a descending alcohol series and subsequently hydrated in tap water. For nuclear staining, the sections were afterwards stained for 6 minutes in hematoxylin. The slides were washed with tap water for 30 seconds to obtain differentiation. Subsequently, the eosinophilic structures were stained for 2:45 minutes with eosin. The slides were washed in tap water for 15 seconds and dehydrated in an ascending alcohol series and xylene. Finally, slides were

automatically covered with the Tissue-Tek® Film™ by using the Tissue-Tek® Coverslipping Film.

The grading was according to the mHAI (modified Histological Activity Index) Score [190]. This grading system provides a detailed evaluation of the inflammation (Tab. 5) and represents the histological features (Tab. 6).

Tab. 5: Modified Histological Activity Index (mHAI).

Criteria	Score	Histoligical features
Interface-Hepatitis	0 1 2 3 4	None Focal, few portal tracts Focal, most portal tracts Continuously around <50% of portal tracts Continuously around >50% of portal tracts
Confluent necroses	0 1 2 3 4 5 6	None Focal Zone-3-necroses, few Zone-3-necroses, numerous Zone-3 and few portocentral bridges Zone-3 and multiple portocentral bridges Panacinar/multiacinar necroses
Single cell necroses	0 1 2 3 4	None Till 1 focus per 10x field 2-4 foci per 10x field 5-10 foci per 10x field >10 foci per 10x field
Portal inflammation	0 1 2 3 4	None Mild, few or all portal tracts Moderate, few or all portal tracts Strong, all portal tracts Massive, all portal tracts

Tab. 6: Histological features of the different grades.

Grade	Verbal	mHAI-Score	Histological features
1	Mild	1-3	Minimal portal inflammatory cell infiltration, none or mild hepatocellular necroses or inflammatory cell infiltration, no interface-hepatitis
2	Moderate	4-8	Mild or moderate portal inflammatory cell infiltration, focal interface-hepatitis, single hepatocellular necroses, no confluent necroses
3	Strong	9-12	Strong portal inflammatory cell infiltration, strong interface-hepatitis, multiple hepatocellular necroses, possible confluent necroses, no bridging or panlobular necroses
4	Massive	13-18	Massive portal inflammatory cell infiltration and interface-hepatitis, strong hepatocellular inflammation with confluent necroses and possible bridging and panlobular necroses

3.2.1.2. Movat Pentachrome staining

The Movat Pentachrome staining was performed to evaluate the degree of fibrosis and to characterize the fibrotic tissue 21 days after the BDL. Collagen and reticular fibers dyed yellow, whereas mucin and ground substance dyed blue. Therefore, sections of FFPE tissue mounted on microscope slides were deparaffinized in xylol, rehydrated in a descending alcohol series and subsequently hydrated in distilled water. The slides were pretreated with 3% acetic acid for 30 seconds and afterwards stained with 1% alcian blue solution for 30 minutes. After being washed in running tap water for 2 minutes, elastic fibers and nuclei were stained with Verhoeff's solution (Verhoeff's solution A, B and C diluted 3:2:1) for 8 minutes. Following this, slides were dipped in 1% iron (III) chloride for 1 minute to obtain differentiation. After being washed with tap water for 10 minutes, slides were incubated with brilliant-croceine-fuchsine-acid-solution for 5 minutes to stain the cytoplasm. Afterwards, slides were dipped in 1% acetic acid for 30 seconds and transferred in 2% phosphotungstic acid for 15 minutes. Following this, slides were dipped in 1% acetic acid for 1 minute and subsequently dehydrated in two changes of 99% ethanol for 3 and 15 minutes. Fibers were stained with safron du gatinais solution for 15 minutes. Finally, slides were dehydrated in an ascending alcohol series and xylene. Coverslips were mounted onto slides using mounting medium.

The staging was according to the Desmet Score [190]. The Desmet Score is used to classify the liver fibrosis into four stages. Here, stage 0 equates no fibrosis, stage 1 a mild, stage 2 a moderate and stage 3 a severe fibrosis with occasional disorders in architecture (Tab. 7).

Tab. 7: Desmet Score.

Stage	Verbal	Histological features
0	No fibrosis	No fibrous expansion
1	Mild fibrosis	Fibrous expansion of some portal tracts
2	Moderate fibrosis	Fibrous expansion of numerous portal tracts, (In-)complete portoportal septa
3	Strong fibrosis	Fibrous expansion with marked septa, possible disorder in architecture
4	Cirrhosis	Complete cirrhotic remodeling

3.2.1.3. Picro Sirius Red staining

The Picro Sirius Red staining was performed to evaluate the collagen deposition in the liver. It dyes collagen I and III red and the cytoplasm yellow. Therefore, sections of FFPE tissue mounted on microscope slides were deparaffinized in xylol, rehydrated in a descending alcohol series and subsequently hydrated in distilled water. The slides were stained with Picro Sirius Red solution for 60 minutes. Afterwards, they were rinsed quickly in two changes of 0.5% acetic acid solution before rinsed in 99% ethanol. Finally, slides were dehydrated in two changes of 99% ethanol and coverslips were mounted onto slides using mounting medium. In the BDL model, the staging was according to the Ishak Score (Tab. 8) [190]. Therefore, the whole tissue section was scored. This staging system provides a sensitive classification of the fibrotic liver into seven stages (0-6).

Tab. 8: The Ishak Score.

Stage	Histological features
0	No fibrosis
1	Fibrous expansion of <50% of portal tracts, occasional short fibrous septa
2	Fibrous expansion of >50% of portal tracts, occasional short fibrous septa
3	Fibrous expansion of >50% of portal tracts, occasional portoportal bridging
4	Fibrous expansion of portal tracts with marked portoportal bridging, occasional portocentral bridging
5	Incomplete cirrhosis with some pseudolobuli
6	Complete cirrhosis

In the CCl_4 model, the Ishak Score was modified due to a different fibrosis pattern. Additionally, to the seven stages of the Ishak Score, the thickness of the septa was taken into consideration for a more precise evaluation. Therefore, the septa were classified in none (0), thin (1) or in thick/marked (2) septa. The Ishak Score and the

thickness of the septa were added into a total modified Ishak Score (mIS). The score ranges from 0 to 8:

mIS = (0-6) + (0-2)

3.2.2. Immunohistochemistry

Immunohistochemical stainings were performed for a more detailed characterization of the murine liver tissue. Therefore, different markers were used: POSTN and TNC as a marker for the proteins of interest, ACTA2 as a marker for aHSC, Keratin, type I cytoskeletal 19 (K1C19) as a marker for the DR, sex-determining region Y-box 9 (SOX9) as a progenitor marker and the proliferation marker protein Ki-67 (MKI67) to determine the hepatocellular proliferation rate.

Sections of FFPE tissue mounted on microscope slides were incubated at 60 °C overnight. Afterwards, they were deparaffinized in xylol, rehydrated in a descending alcohol series and subsequently hydrated in distilled water. A heat-induced epitope retrieval was performed with a pressure cooker. Therefore, the slides were immersed in citrate or TE buffer, boiled for 20 minutes and allowed to cool down for 30 minutes. After being washed twice in TBS-T, slides were incubated in 3% H_2O_2 to block the endogenous peroxidase. Subsequently, the slides were washed twice in TBS-T and the tissue was surrounded with a hydropic barrier using a pap pen. To avoid non-specific background staining, a protein block was performed with blocking solution for one hour. Afterwards, slides were rinsed in TBS-T and the first antibody, diluted in blocking solution with the appropriate dilution was applied on the tissue for one hour (Tab. 9). Following this, slides were washed twice in TBS-T and were incubated with the secondary antibody for 30 minutes. Slides were washed again for two times and the detection system was added. Depending on the primary antibody, different detection systems were used (Tab. 9). If the polymer detection system was used, the last two steps were replaced by adding ZytoChem Plus (HRP) one-step polymer for 30 minutes. Afterwards, slides were washed again twice in TBS-T and incubated with DAB with corresponding duration. The color reaction was stopped by washing the slides in tap water and afterwards they counterstained with Meyer’s hematoxylin for 20 seconds. The slides were subsequently rinsed with running tap water. In the end,

slides were dehydrated in an ascending alcohol series and coverslips were mounted onto slides using mounting medium.

Tab. 9: Antibodies and corresponding detection systems.

Antibody	Dilution	Antigen Demasking	Detection system	DAB incubation time
Anti-TNC	1:300	TE buffer	VECTASTAIN® ABC "Rabbit"	2 min
Anti-POSTN	1:200	Citrate buffer	VECTASTAIN® ABC "Rabbit"	2 min
Anti-ACTA2	1:200	Citrate buffer	VECTASTAIN® ABC "Rabbit"	2 min
Anti-TROMA III (K1C19)	1:200	TE buffer	One-Step Polymer	1:30 min
Anti-SOX9	1:1000	Citrate buffer	VECTASTAIN® ABC "Rabbit"	1:30 min
Anti-MKI67	1:200	Citrate buffer	VECTASTAIN® ABC "Mouse"	45 sec

3.2.2.1. Periostin and Tenascin C quantification

The expression of the extracellular matrix proteins POSTN and TNC was quantified by using a total score of intensity and distribution. Therefore, the whole tissue section was scored. Due to different fibrosis patterns the score was adapted to the respective mouse model. The BDL model causes portal fibrosis and therefore, the periportal area (PP) was taken into consideration. The CCl_4-model causes a pericentral fibrosis and therefore, the pericentral area (PC) was taken into consideration. The intensity was classified from negative (0), weak (1), moderate (2) to strong (3). The distribution was classified as grade 0 (negative), grade 1 (< 25% of PP or PC), 2 (> 50% of PP or PC), 3 (> 50% of PP or PC and < 25% of the parenchyma) and 4 (> 50% of PP or PC and > 50% of the parenchyma). The intensity and distribution scores were added into a total score of Periostin expression. The score ranges from 0 to 7:

Periostin or Tenascin C Score = (0-3) + (0-4)

3.2.2.2. Actin alpha 2, smooth muscle

The myogenic marker ACTA2 is a well-established marker for aMF [2]. Under normal conditions, it is only expressed in the wall of portal and central veins. After an injury and the following activation of MF, these cells express ACTA2 [8]. The

expression of ACTA2 was quantified by using a total score of intensity and distribution. Therefore, the whole tissue section was scored. The expression was quantified portal/periportal (PP), septal (S), perisinusoidal (PS) and pericentral (PC). The intensity was classified from negative (0), weak (1), moderate (2) to strong (3). The distribution was classified as grade 0 (negative), grade 1 (< 25% of tissue), 2 (25-50% of the tissue), 3 (50-75% of the tissue), 4 (> 75% of the tissue). Intensity and distribution scores of all four locations were added into a total histopathological Score (HS). The score ranges from 0 to 28:

HS = PP [(0-3) + (0-4)] + S [(0-3) + (0-4)] + PS [(0-3) + (0-4)] + PC [(0-3) + (0-4)]

3.2.2.3. Keratin, type I cytoskeletal 19

K1C19 belongs to the family of keratins. It is expressed in ductal epithelium and therefore used to represent and evaluate the DR in damaged liver tissue [191]. The expression of K1C19 was evaluated in eight randomly chosen fields at 20x magnification. Due to different expression pattern, the DR was determined differently. In the BDL-model, the DR was reported as ratio between the total amount of bile ducts and portal tracts. In both experimental groups of the CCl_4-model, the DR was reported as a total amount of bile ducts of the eight fields.

3.2.2.4. SRY-Box Transcription Factor 9

SOX9 is a marker for HPC. $SOX9^+$ mature hepatocytes behave in injured livers like HPC. They are bipotential cells which are characterized by the ability to differentiate into cholangiocytes or hepatocytes [192]. The expression of SOX9 in hepatocytes was evaluated in ten randomly chosen high-power fields (HPF, 40x), according to the H-Score [193]. The intensity was classified in weak (1), moderate (2) and strong (3) regarding the percentage of positive stained cells. The score ranges from 0 to 300 and is determined by using following formula:

H-Score = (3 x % of strong stained cells) + (2 x % of moderate stained cells) + (1 x % of weak stained cells)

3.2.2.5. Proliferation marker protein Ki-67

The nuclear antigen MKI67, is a marker for proliferating cells. It is expressed during the G1- until the M-phase in the cell cycle and is absent in quiescent cells [194].

Therefore, MKI67 was used to determine the hepatocellular proliferation index (HPI). In five randomly chosen high-power fields (HPF), the percentage of positive stained hepatocytes were manually counted, and the average was calculated. This results in following formula:

HPI (%) = (% of HPF 1 + % of HPF 2 + % of HPF 3 + % of HPF 4 +% of HPF 5) / 5

3.3. RNA analysis

RNA was isolated and the genes of interest were analyzed by using the quantitative real-time PCR (qRT-PCR). The analyses were carried out with the support of Katrin Binia.

3.3.1. RNA isolation from liver tissue

Snap frozen liver tissue was homogenized by using the TissueLyser LT (Qiagen). Subsequently, the RNA isolation was performed with the Qiagen RNeasy Mini Kit according to the manufacturer's instructions. The RNA concentration was measured with a photometer and stored at -80 °C.

3.3.2. cDNA synthesis

5 µg of total RNA was reverse transcribed into cDNA by using the RevertAid First Strand cDNA Synthesis Kit (Thermo Fisher). The procedure was performed according to the manufacturer's instructions. The cDNA was stored at -20 °C.

3.3.3. Quantitative real-time PCR

The qRT-PCR was performed by using the StepOnePlus™ real-time PCR system (Applied Biosystems). For the qRT-PCR a 20 µl reaction was set as following:

SYBR GREEN (2x):	10 µl
Each Primer (10 µM):	1 µl
cDNA:	20 ng
ddH_2O:	adjust to 20 µl

All samples were pipetted in triplets in a 96-well plate. Relative quantification of gene expression and normalized to control sham mice was calculated with the ΔΔCT-method. GAPDH was used as housekeeping gene.

The following qRT-PCR program was used for the gene analyses:

95 °C 10 min.

40 cycles with:

95 °C 15 sec.

60 °C 20 sec.

72 °C 30 sec.

Meltingscurve:

95 °C 15 sec.

60 °C 1 min.

90 °C 15 sec.

3.4. Statistical analysis

Statistical analysis was performed using the GraphPad Prism 7 software (GraphPad Software Inc., San Diego, CA, USA) and statistical significance between control and knockout mice was determined by Kruskal-Wallis test. Results are presented as means ± standard error of the mean (SEM). *P* values less than 0.05 were considered statistically significant (* $P< 0.05$; ** $P< 0.01$; *** $P<0.001$).

IV. RESULTS

1. Results of the bile duct ligation model

The BDL model was performed to induce a cholestatic liver fibrosis. Mice were sacrificed 3, 7 or 21 days after the operation.

1.1. Necroscopies

In the BDL model, two $Tnc^{-/-}$ mice had to be taken out of the experiment because of a bad general condition. One two days and the other one six days after the operation. Neither controls nor $Postn^{-/-}$ mice had to be removed from the experiment or died due to the operation. The necroscopies of all sham operated mice showed no abnormalities of the general condition or of the peritoneal cavity as well as a normal liver and gallbladder. Instead, three days after the BDL, all mice showed a mild jaundiced skin and a mild jaundiced serosa of the peritoneal cavity. The gallbladder was enlarged, and the liver showed multiple red miliary dots. Seven days after the operation all mice of the experimental group showed a more severe icterus, a more enlarged gallbladder as well as a mild enlarged liver compared to the sham group. Over the time, the icterus worsened among all genotypes. After 21 days, the necroscopy of every mouse revealed a massively enlarged gallbladder as well as an enlightened and enlarged liver with a rougher surface (Fig. 9). Macroscopically, there was never a difference between the liver tissue of the three genotypes.

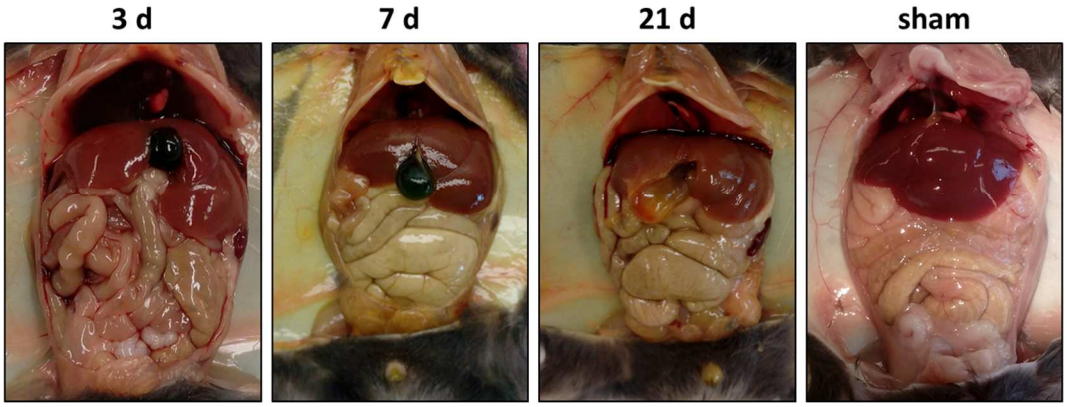

Fig. 9: The liver of control mice after the BDL. The liver and gallbladder got bigger and the

jaundice worsened with progressive cholestatic damage.

The analysis of the liver- and bodyweight identified an increased relation at all timepoints in any mice, without achieving statistical significance between the genotypes. After the BDL, the liver-body weight-relation (LBW-r. %) increased continuously in control mice to a mean maximum of 7.90% and in Postn$^{-/-}$ mice to 9.13%. In Tnc$^{-/-}$ mice, the LBW-r. % increased only until day seven and amounted 7.17% after 21 days (Fig. 10).

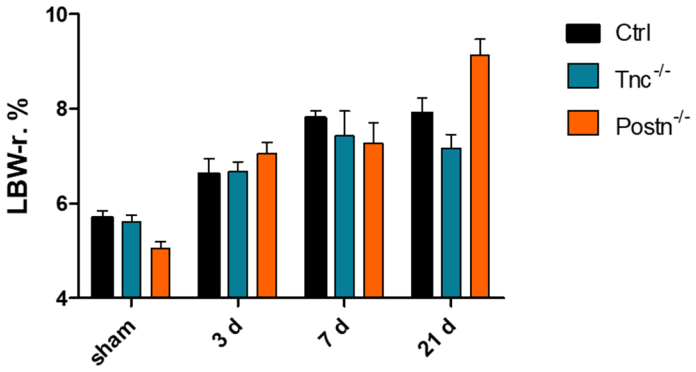

Fig. 10: Increasing LBW-r. % after the BDL. After 21 days, Postn$^{-/-}$ mice showed a higher, Tnc$^{-/-}$ mice a lower LBW-r. % as control mice. Data are expressed as means ± SEM (n=5-6), Kruskal-Wallis test.

1.2. Results of the histological stainings

Different histological stainings for the characterization of the liver tissue in course of a cholestatic injury were evaluated. All sham operated mice showed a normal liver tissue without any evidence for an inflammatory or fibrotic process (data not shown).

1.2.1. Inflammation analysis

In the HE staining, control mice showed a mild portal inflammation with occasionally focal interface hepatitis in a few portal tracts three days after the BDL. Besides occasional single cell necroses, multiple confluent necroses were observed. Seven days after the operation, the mice showed an increased portal inflammation as well as more focal interface hepatitis spots. The amount of confluent necroses decreased, whereas the number of single-cell necroses increased. Finally, after 21 days, the portal inflammation was still moderate. The

interface hepatitis increased and was occasionally continuously around the portal tracts. The amount of confluent necrosis further decreased, and the number of single-cell necroses slightly increased (Fig. 12 B, E). To sum it up, the mHAI Score continuously increased with progressive damage to a mean mHAI of 7.83 (Fig. 11).

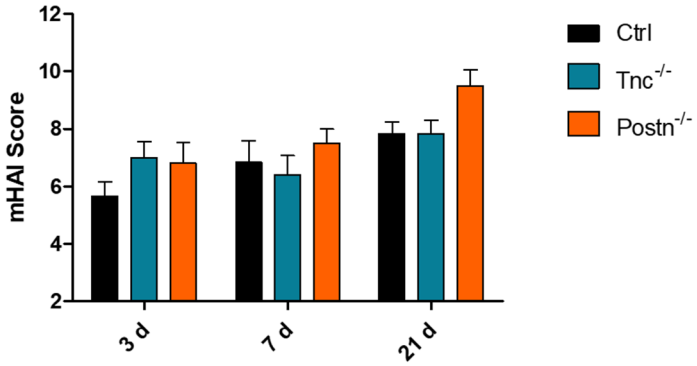

Fig. 11: Increased inflammatory activity after BDL. Degree of inflammation was evaluated by using the mHAI Score. After 21 days, Postn$^{-/-}$ mice showed a higher mHAI Score due to more remaining necrotic spots. Tnc$^{-/-}$ mice showed a similar inflammatory activity compared to control mice. Data are expressed as means ± SEM (n=5-6), Kruskal-Wallis test.

Postn$^{-/-}$ mice showed the same inflammatory pattern. In comparison to control mice, they had a slightly higher inflammatory activity due to larger necrotic area three and seven days after the BDL. After 21 days, Postn$^{-/-}$ mice had more remaining necrotic spots (Fig. 12 A, D). Therefore, in general they showed a higher degree of inflammation and a mean mHAI Score of 9.5 after 21 days (Fig. 11).

Tnc$^{-/-}$ mice showed the same inflammatory pattern as well. Like Postn$^{-/-}$mice, they had a stronger inflammatory activity compared to control mice at day three because of confluent necroses. With progressive liver damage, the mHAI Score further increased to a mean mHAI Score of 7.83 after 21 days (Fig. 11). Finally, no difference in the inflammatory reaction was observed in comparison to control mice (Fig. 12 C, F).

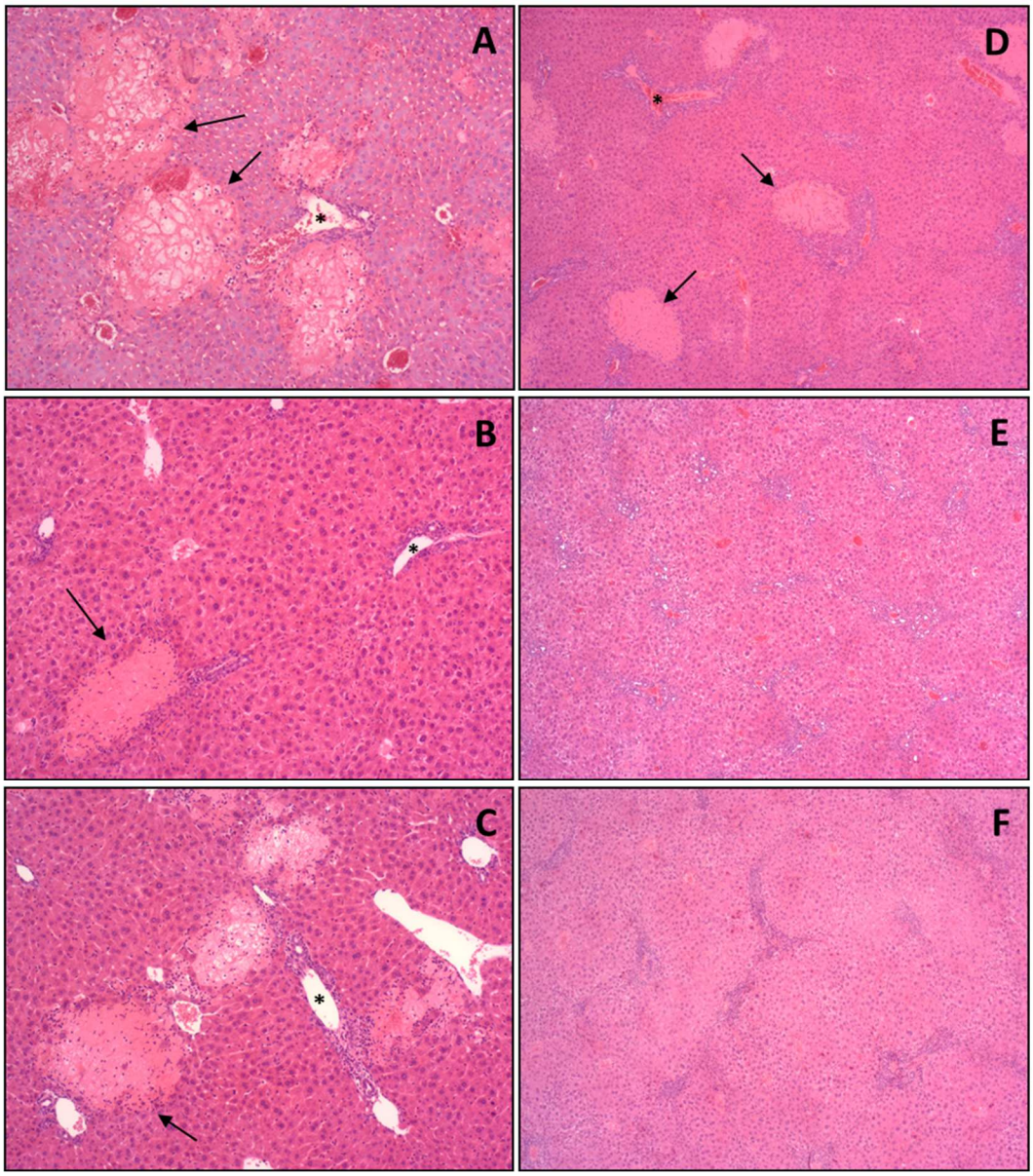

Fig. 12: Increased inflammatory activity after 3 (A-C, 10x) and 21 days (D-F, 5x). Representative HE stainings illustrate necrotic spots (arrows) and inflammatory cells around portal tracts (asterisks). Postn$^{-/-}$ mice showed after 3 days (A) and 21 days (D) a higher inflammatory response and remaining confluent necroses compared to control mice (B, E). Tnc$^{-/-}$ mice showed after 3 days (C) a higher and after 21 days (F) a similar inflammatory response as control mice.

1.2.2. ECM analysis

The composition of the ECM was characterized by using the Movat Pentachrome staining. Control mice showed mild enlarged portal tracts three days after the operation. An increased amount of blue stained ground substance was present. After seven days, the portal tracts were fibrous extended, and the amount of ground substance further increased with progressive liver damage. Gradually, the composition of the ECM changed as well. Yellow dyed collagen fibers could be

occasionally observed in larger portal tracts. After 21 days, control mice showed a moderate to severe fibrosis with marked septa and occasional disorders in the architecture of the liver parenchyma. The composition of the ECM was predominantly yellow dyed collagen with occasionally blue dyed ground substance (Fig. 13). The mean Desmet Score was 2.83 after 21 days (Fig. 14 A, D). $Postn^{-/-}$ and $Tnc^{-/-}$ mice showed a similar trend in the composition of the ECM and in fibrogenesis. After 21 days, $Postn^{-/-}$ mice had a higher portion of blue dyed ground substance left when compared to control mice. Furthermore, they showed a weaker fibrotic response with partially complete portoportal septa and a mean Desmet Score of 2.17 at day 21 (Fig. 14 C, D). In $Tnc^{-/-}$ mice, the major portion of the ECM was yellow dyed collagen fibers with occasionally blue dyed ground substance after 21 days. They showed a moderate to strong fibrosis pattern with occasional disorders in architecture with a mean Desmet Score of 2.67 (Fig. 14 B, D).

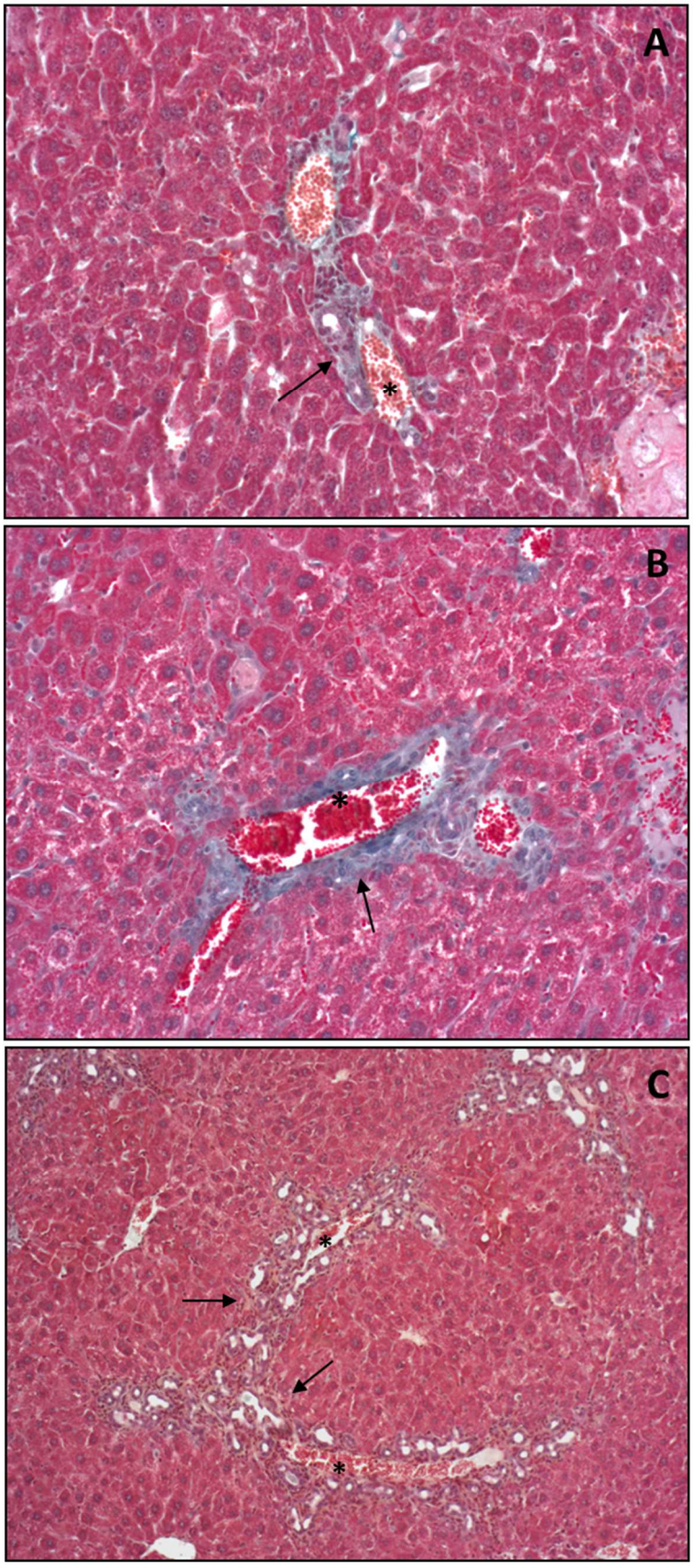

Fig. 13: The composition of the ECM of control mice after BDL. Representative Movat stainings after 3 (A, 20x), 7 (B, 20x) and 21 days (C, 10x). The composition and the amount of ECM (arrows) around portal tracts (asterisks) changed with progressive cholestatic damage. Portal tracts got enlarged and fibrous extended. The amount of ground

substance and of collagen-rich ECM increased.

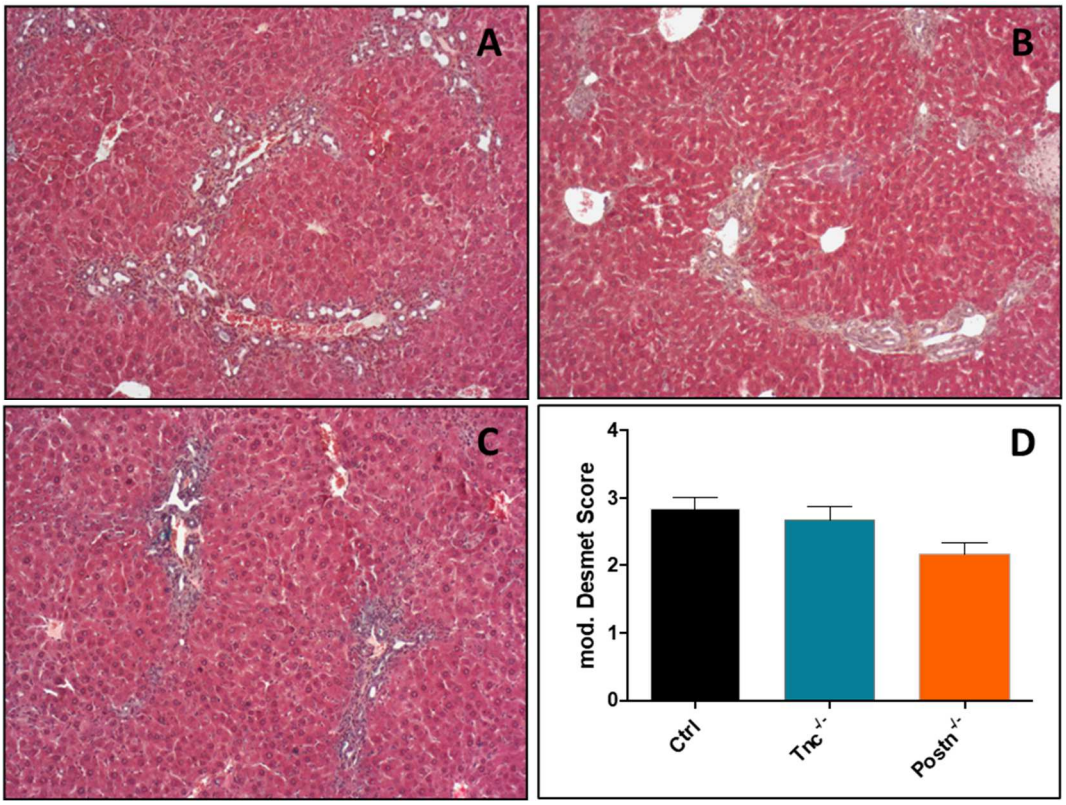

Fig. 14: The composition of the ECM 21 days after BDL. Representative Movat stainings of Ctrl (A), Tnc$^{-/-}$ (B) and Postn$^{-/-}$ mice (C). Staging according to the modified Desmet Score after 21 days (D). Control and Tnc$^{-/-}$ mice showed a similar composition as well as a similar fibrotic response. Postn$^{-/-}$ mice showed a higher portion of blue dyed ground substance and a reduced fibrotic response. A-C: 10x. D: Data are expressed as means ± SEM (n=5-6), Kruskal-Wallis test.

1.2.3. Analysis of fibrosis stage

The fibrosis stages after seven and 21 days were determined by using the PSR staining. Seven days after the BDL, control mice showed an increased deposition of collagens in the portal/periportal area, mainly around the bile ducts. The fibrous expansion was detectable in less than 50% of the portal tracts. The collagen deposition increased with progressive liver damage, predominantly in the portal and periportal tract. After 21 days, an increased collagen deposition was also occasional observed in the perisinusoidal space. Moreover, more than 50% of the portal tracts showed a fibrous expansion. The increased collagen deposition led to multiple fibrous septa, isolated portoportal bridges and complete nodules (Fig. 15; Fig. 16 B). Finally, control mice showed a mean Ishak Score of 2.33 after 21 days (Fig. 15 D).

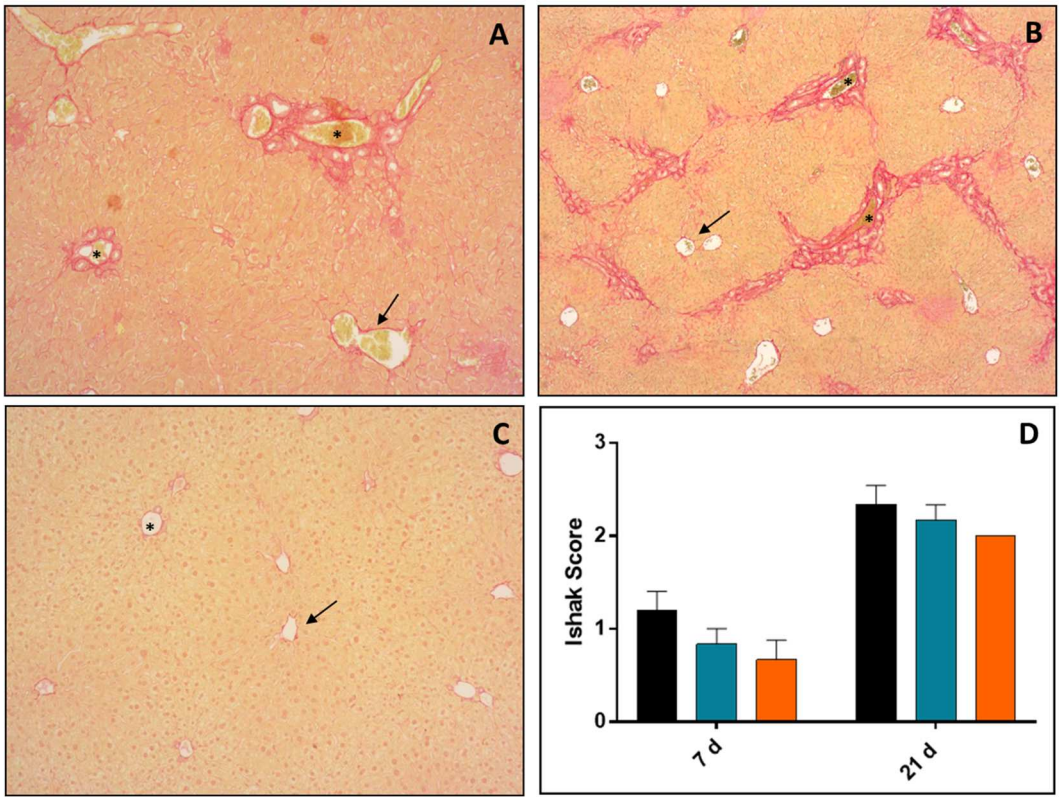

Fig. 15: Increased deposition of Collagen I and III after BDL. Representative PSR stainings of control mice after 7 (A, 10x), 21 days (B, 5x) and of a sham operated mouse (C, 5x). The collagen deposition increased around portal tracts (asterisks). The area around the central veins (arrows) showed a normal collagen deposition. D: Staging according to the Ishak Score. Black bars: Ctrl, blue bars: $Tnc^{-/-}$, orange bars: $Postn^{-/-}$. Data are expressed as means ± SEM (n=5-6), Kruskal-Wallis test.

$Postn^{-/-}$ and $Tnc^{-/-}$ mice depicted the same fibrosis pattern as control mice. Compared to control mice, $Postn^{-/-}$ mice had less fibrous expanded portal tracts after seven days. After 21 days, they had less marked septa and portoportal bridges. (Fig. 16 A). Finally, $Postn^{-/-}$ mice showed a lower deposition of collagens in the perisinusoidal space as well as in the portal tracts with a mean Ishak score of 2.0 after 21 days (Fig. 15 D). In $Tnc^{-/-}$ mice, a general slightly lower collagen deposition was observed with a mean Ishak score of 2.17 after 21 days (Fig. 16 C; Fig. 15 D).

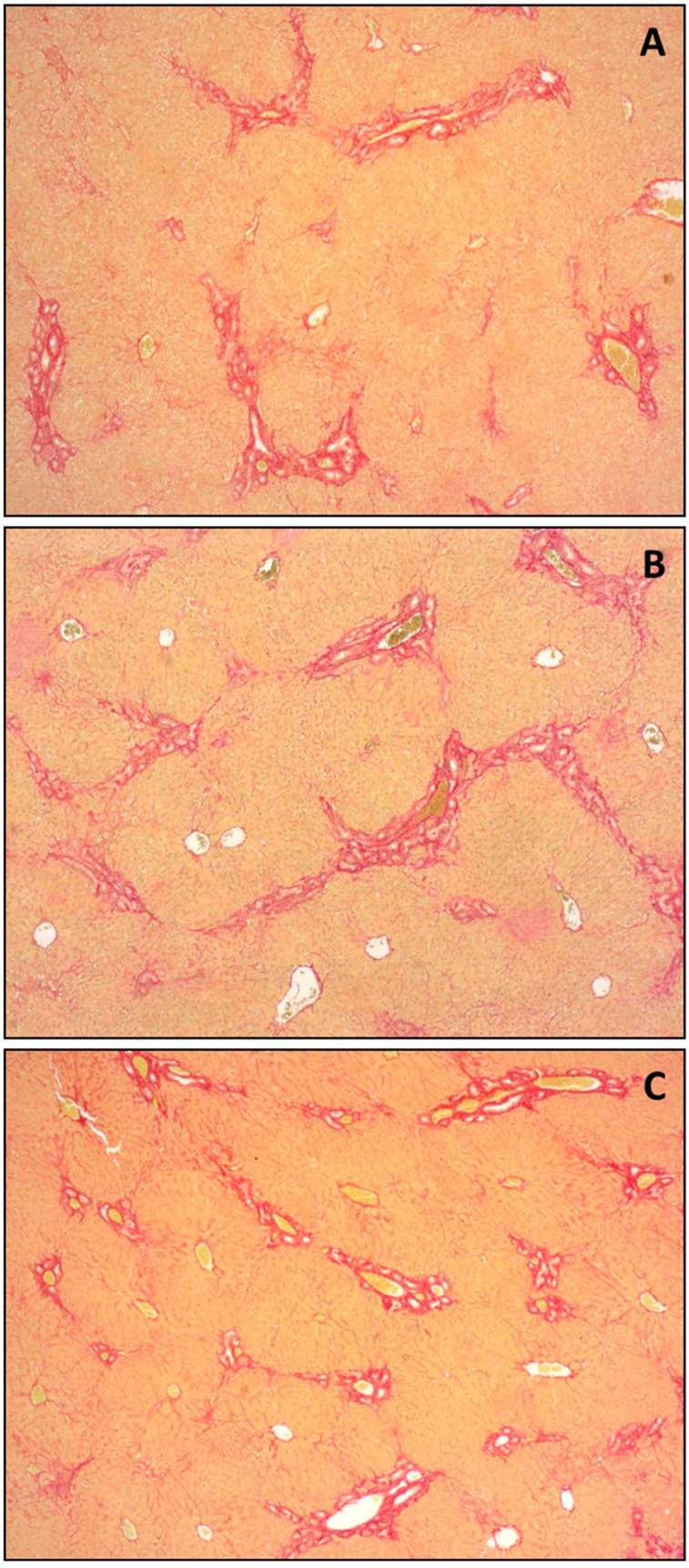

Fig. 16: Collagen deposition 21 days after BDL. Representative PSR stainings of Postn$^{-/-}$ (A), control (B) and Tnc$^{-/-}$ mice (C). Postn$^{-/-}$ mice showed a lower collagen deposition and less septa as control mice. Tnc$^{-/-}$ mice showed a similar collagen deposition as control

mice. A-C: 5x.

In conclusion, the histological stainings reveal that Postn$^{-/-}$ mice tend to a higher inflammatory reactivity and a reduced fibrotic response, whereas Tnc$^{-/-}$ mice show predominantly the same degree of inflammation and fibrosis as control mice. However, the differences do not achieve statistical significance.

1.3. Results of the immunohistochemistry and corresponding qRT-PCR

Different markers for the immunohistochemistry and the qRT-PCR were used for a more detailed characterization of the liver tissue.

1.3.1. Periostin

Control mice showed a predominant mild expression of POSTN in less than 50% of the portal tracts three days after the BDL. POSTN was located directly around bile ducts. With progressive damage, the expression of POSTN increased. After seven days, it was expressed in more than 50% of the portal tracts. It was predominant detectable around bile ducts, but not in the parenchyma. After 21 days, the POSTN expression further increased to mean POSTN Score of 4.67 (Fig. 17). It was mainly located around bile ducts with occasional diffuse extensions in the perisinusoidal space of the parenchyma (Fig. 19 A-C).

Tnc$^{-/-}$ mice showed the same pattern and progression of POSTN expression as control mice (Fig. 19 D-F). After 21 days, they showed a mean POSTN Score of 4.6 (Fig. 17).

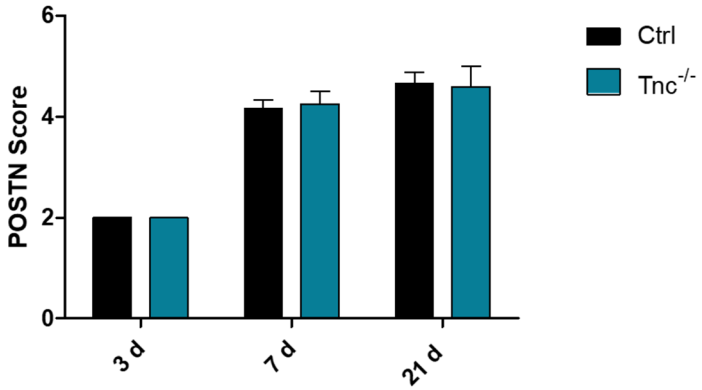

Fig. 17: Increased POSTN expression in control and Tnc$^{-/-}$ mice after BDL. POSTN expression was quantified by using a total score of intensity and distribution. It increased continuously in both genotypes. Data are expressed as means ± SEM (n=5-6),

Kruskal-Wallis test.

Similar results can be observed on the mRNA level. In control and Tnc$^{-/-}$ mice, the gene expression of *Postn* increased continuously with progressive liver damage (Fig. 18).

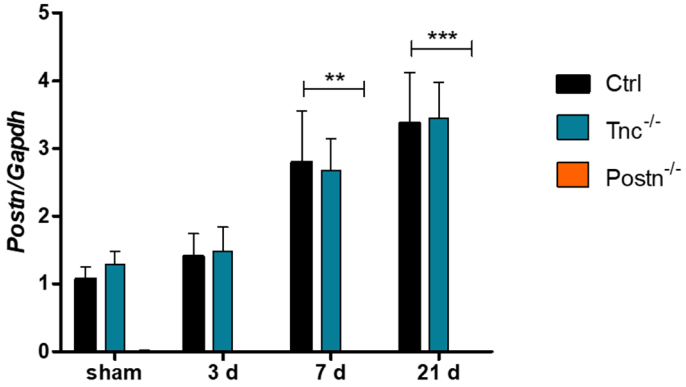

Fig. 18: Increasing mRNA expression level of *Postn* after BDL. In control and Tnc$^{-/-}$ mice the *Postn* mRNA expression increased with progressive liver damage. Relative quantification of gene expression was calculated with ΔΔCT-method to *Gapdh* and normalized to Ctrl sham mice. Data are expressed as means ± SEM (n=5-6), Kruskal-Wallis test, * $P< 0.05$, ** $P< 0.01$, *** $P< 0.001$.

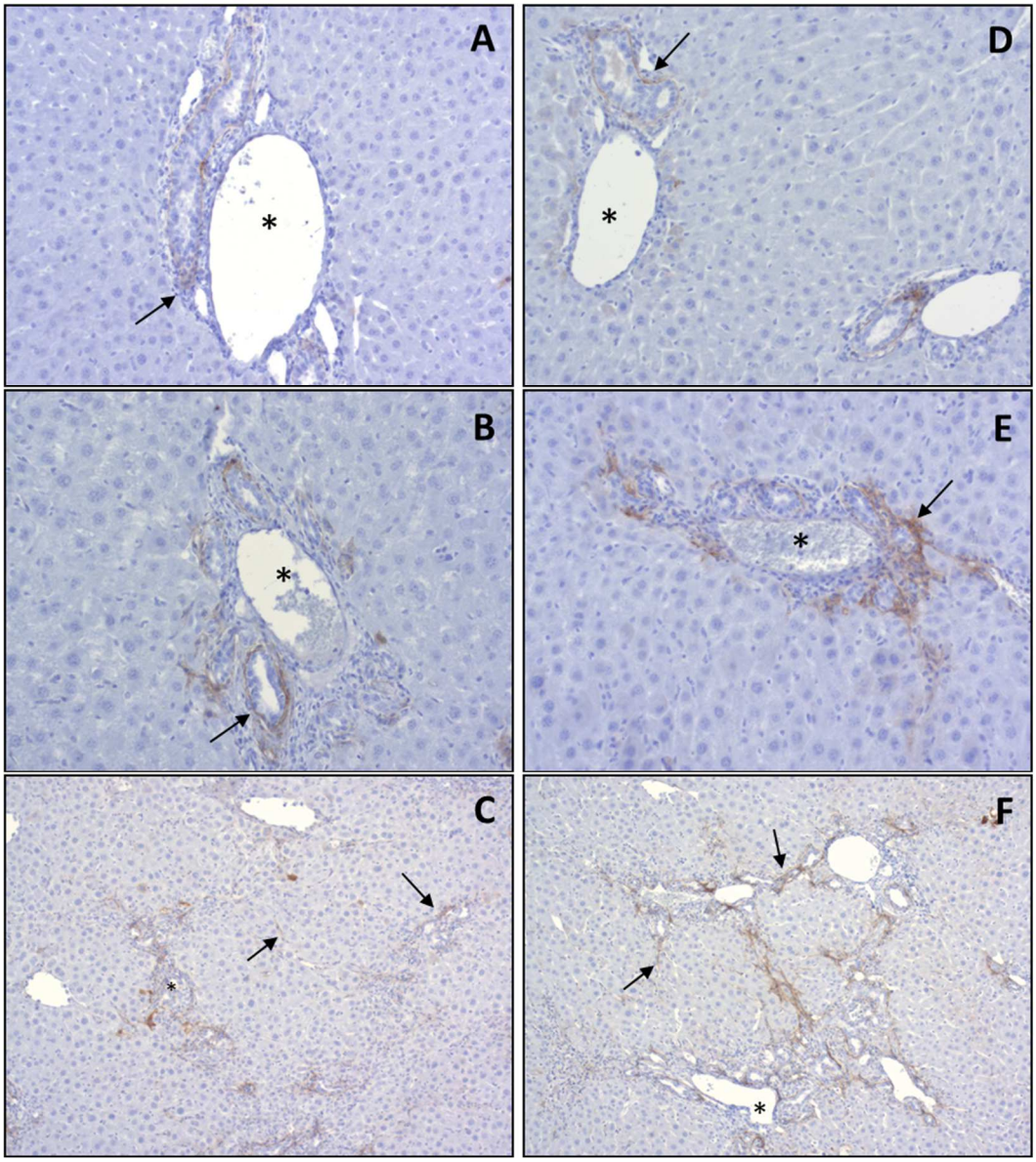

Fig. 19: Increased POSTN expression in the liver of control (A-C) and Tnc$^{-/-}$ mice (D-F) after BDL. Representative POSTN stainings after 3 (A, D), 7 (B, E) and 21 days (C, F). Increasing POSTN expression (arrows) around bile ducts of the portal tract (asterisks) as well as in the parenchyma. A, B, D, E: 20x, C, F: 10x.

1.3.2. Tenascin C

Control mice showed a predominant mild expression of TNC in more than 50% of the portal tracts three days after the BDL. The expression was limited to the portal and periportal area. With progressive damage, the TNC expression increased and became more moderate in the portal tracts. After seven days, it was also slightly detectable in the perisinusoidal space in the parenchyma. TNC was still expressed predominantly portal/periportal with an involvement of less than 50% of the

parenchyma. After 21 days, the TNC expression in the parenchyma increased as well to a more moderate state and was occasionally diffuse in more than 50% of the parenchyma (Fig. 21 A-C). Altogether, the expression of TNC increased continuously to mean TNC Score of 5.5 after 21 days (Fig. 20).

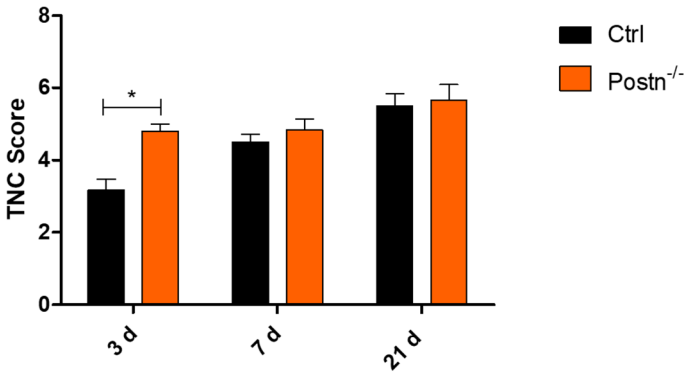

Fig. 20: Increased TNC expression in control and Postn$^{-/-}$ mice after BDL. TNC expression was quantified by using a total score of intensity and distribution. Postn$^{-/-}$ mice showed an earlier increased TNC expression compared to control mice. Data are expressed as means ± SEM (n=5-6), Kruskal-Wallis test, * $P< 0.05$.

Postn$^{-/-}$ mice showed a significant higher and more moderate expression of TNC compared to control mice three days after the BDL. It was already expressed diffusely in the perisinusoidal space of less than 50% of the parenchyma. The TNC expression increased with progressive liver damage. After 21 days, the TNC expression was comparable with the expression in control mice and the mean TNC Score was 5.67 (Fig. 20; Fig. 21 D-F).

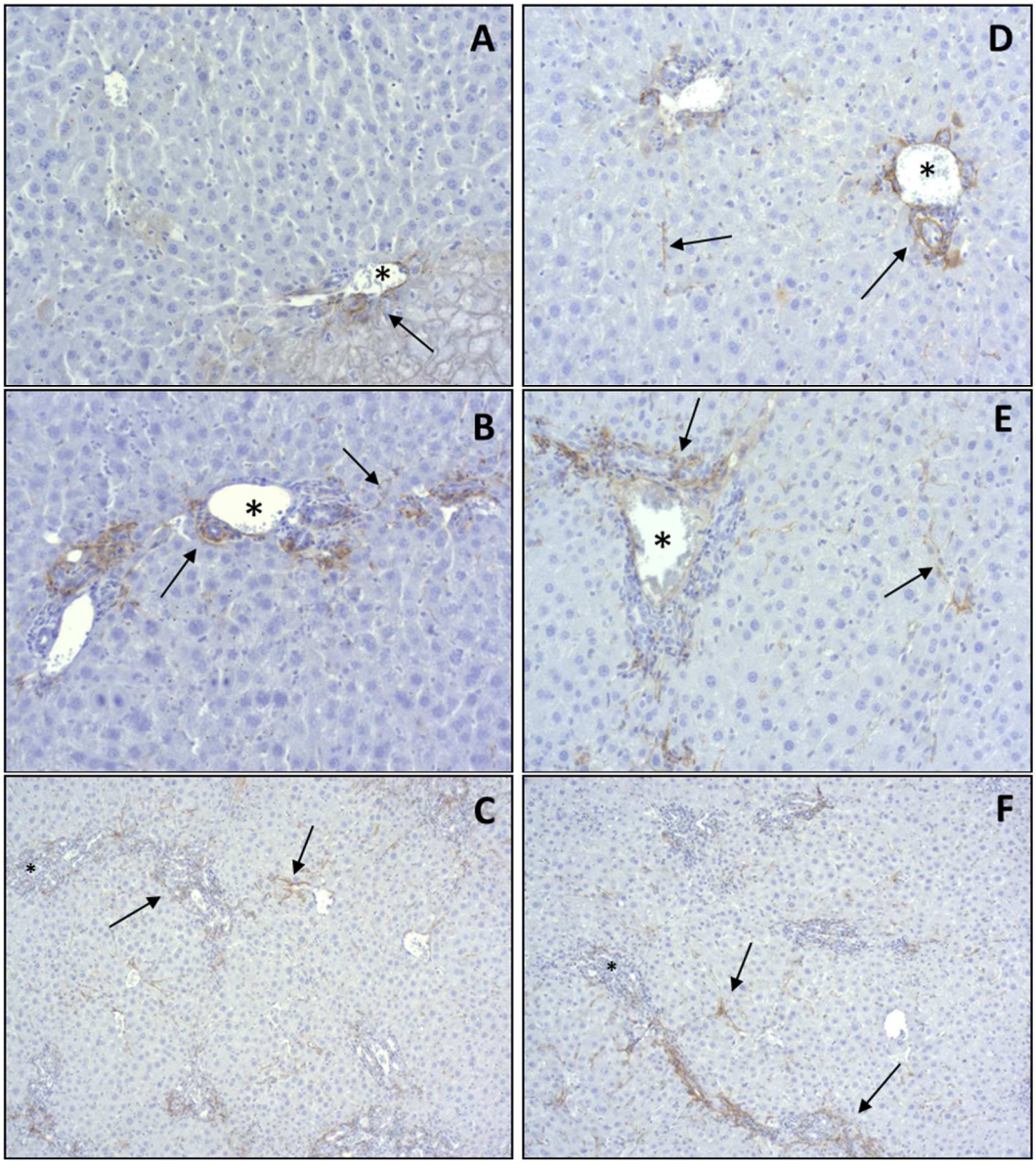

Fig. 21: Increased TNC expression in the liver of control (A-C) and Postn$^{-/-}$ mice (D-F) after BDL. Representative TNC stainings after 3 (A, D), 7 (B, E) and 21 days (C, F). TNC expression (arrows) increased around bile ducts of the portal tract (asterisks) and in the parenchyma with progressive liver damage. In contrast to control mice, showed Postn$^{-/-}$ mice already after three days a perisinusoidal expression in the parenchyma. A, B, D, E: 20x. C, F: 10x.

Similar results can be observed on the mRNA level. In control mice, the gene expression of *Tnc* increased continuously with progressive liver damage. In Postn$^{-/-}$ mice, the expression was already increased in the sham operated mice. Furthermore, Postn$^{-/-}$ mice showed a higher *Tnc* mRNA expression after three and seven days, which further increased with progressive injury (Fig. 22).

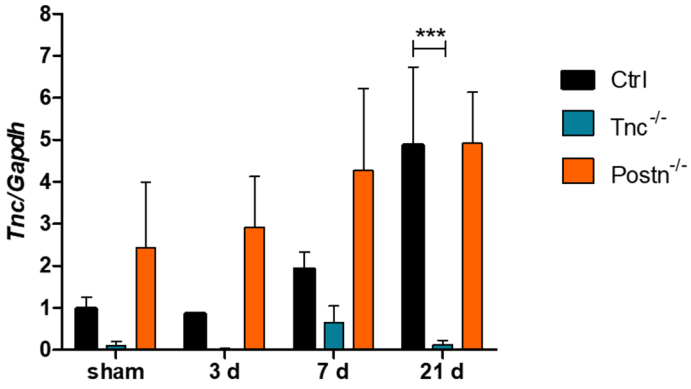

Fig. 22: Increased mRNA level of *Tnc* after BDL. In control and Postn$^{-/-}$ mice the *Tnc* mRNA expression increased with increasing liver damage. Postn$^{-/-}$ showed a higher *Tnc* mRNA expression in the sham group as well as in the early phase after BDL. Relative quantification of gene expression was calculated with ΔΔCT-method to *Gapdh* and normalized to control sham mice. Data are expressed as means ± SEM (n=5-6), Kruskal-Wallis test, * $P< 0.05$, ** $P< 0.01$, *** $P<0.001$.

1.3.3. Analysis of aMF

The localization and number of aMF was determined by using ACTA2. In control mice, aMF were mainly located in portal tracts and around necrotic areas three days after the BDL. With progressive liver damage, the portal tracts enlarged and the amount of aMF increased. Activated MF were predominantly portal/periportal and around the DR with additional extension in the perisinusoidal space of the parenchyma. After 21 days, there was a strong portal/periportal expression as well as a more diffuse extension along marked porto-portal septa in the parenchyma (Fig. 24 B, E). The mean histopathologic Score was 14.67 (Fig. 23).

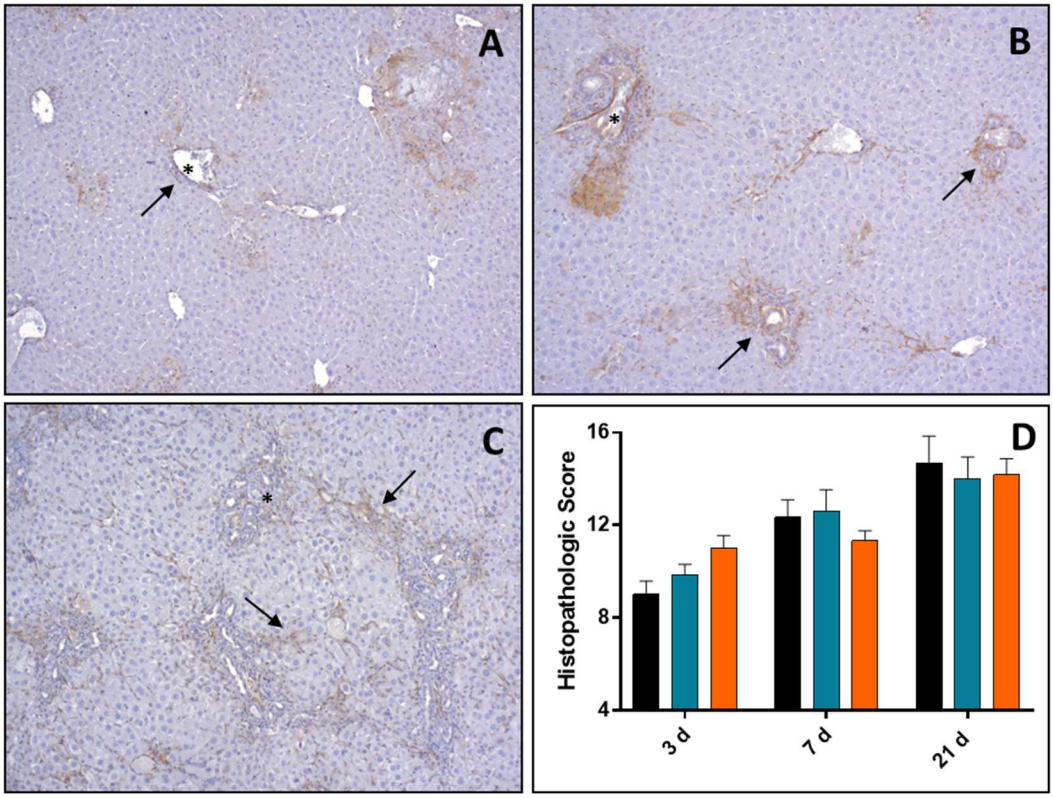

Fig. 23: Increased amount of aMF after BDL. Representative ACTA2 stainings of control mice after 3 (A), 7 (B) and 21 days (C). Activated MF (arrows) were mainly located in/around portal tracts (asterisks). With progressive liver damage, the amount of aMF increased and were also detectable in the parenchyma. The aMF accumulate around the bile ducts and along fibrotic septa. Quantification of aMF based on the intensity and extent of immunoreactivity for ACTA2 (D). Both parameters were added to a total histopathologic Score, black bars: Ctrl, blue bars: $Tnc^{-/-}$, orange bars: $Postn^{-/-}$. Data are expressed as means ± SEM (n=5-6), Kruskal-Wallis test. A-C: 10x.

$Postn^{-/-}$ and $Tnc^{-/-}$ mice showed the same expression pattern of ACTA2 as control mice. After three days, $Postn^{-/-}$ mice showed a slightly higher amount of aMF in portal tracts with occasional ACTA2 positive cells in the parenchyma compared to control mice. After 21 days, the amount of aMF was slightly lower compared to control mice, mainly because of a lower expression in the parenchyma (Fig. 24 A, D). The mean histopathologic Score increased to 14.17 (Fig. 23 D). At the beginning, $Tnc^{-/-}$ mice showed a slightly higher number of aMF than control mice. However, after 21 days the number was lower and the mean histopathological Score was 14.0 (Fig. 23; Fig. 24 C, F).

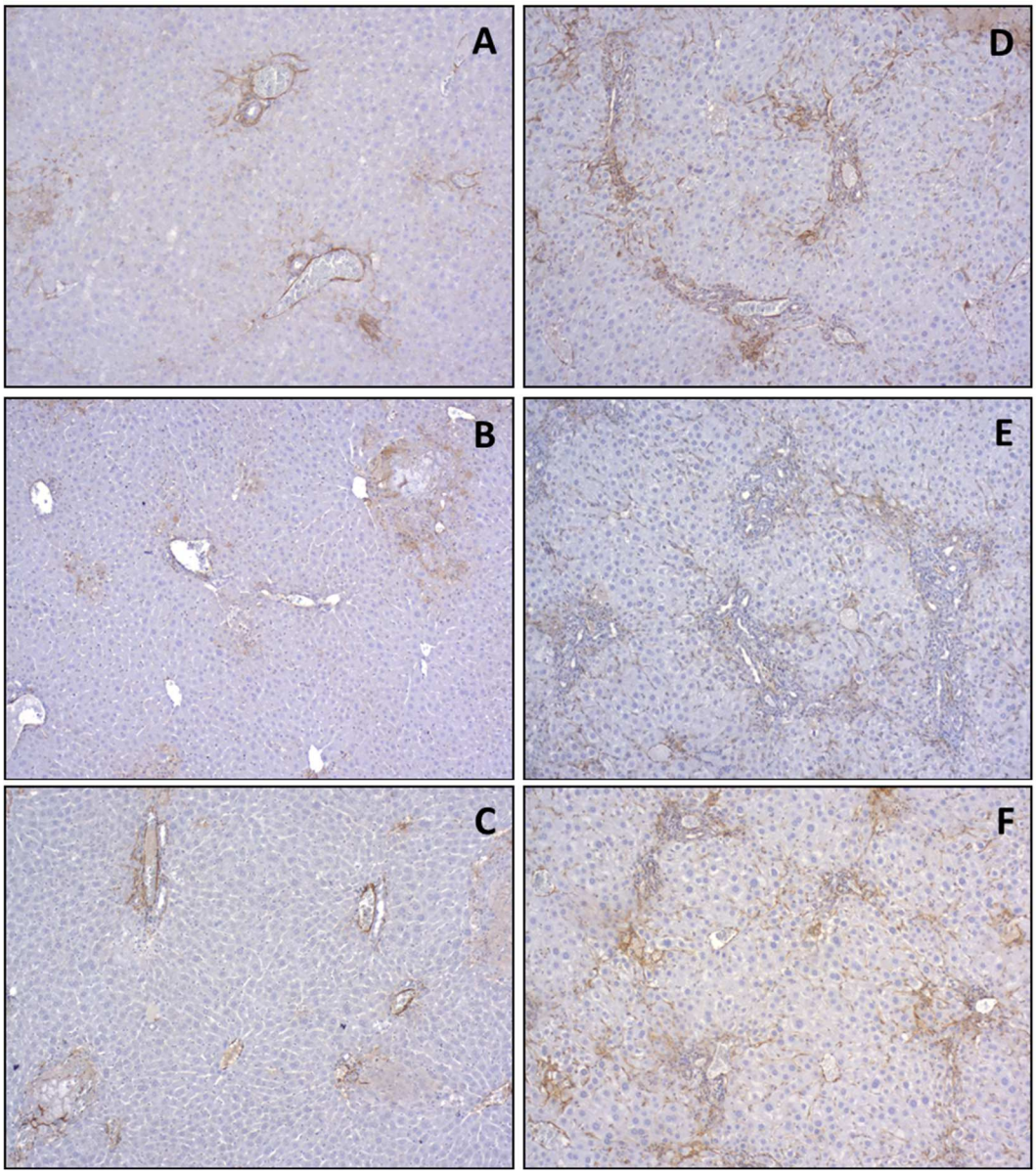

Fig. 24: Increased expression of ACTA2 three (A-C) and 21 days (D-F) after the BDL. Representative ACTA2 stainings of Postn$^{-/-}$ (A, D), control (B, E) and Tnc$^{-/-}$ mice (C, F). After three days, Postn$^{-/-}$ and Tnc$^{-/-}$ mice showed a higher expression of ACTA2, mainly around portals tracts compared to control mice. After 21 days, both knockout mice showed a lower amount of aMF as control mice. A-F: 10x.

The *Acta2* mRNA level increased in control mice and Tnc$^{-/-}$ mice continuously with progressive injury. In Postn$^{-/-}$ mice, the expression of *Acta* increased after the BDL as well but was more constant. After three and seven days, Postn$^{-/-}$ mice demonstrated a higher *Acta2* mRNA level and after 21 days a lower level than control mice. In Tnc$^{-/-}$ mice, the mRNA level was higher than in control mice after seven and 21 days (Fig. 25).

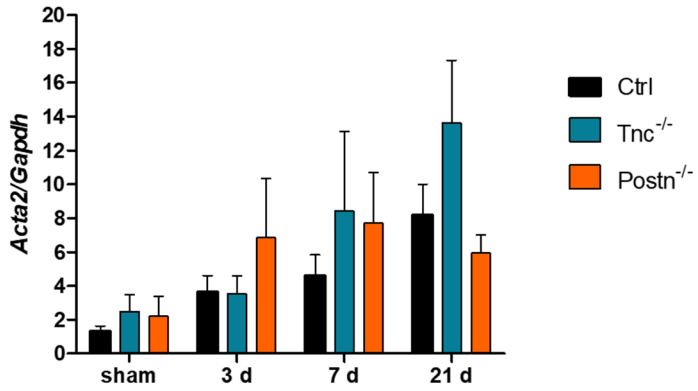

Fig. 25: Increased mRNA level of *Acta2* after BDL. Upregulation of *Acta2* after BDL. In control and Tnc$^{-/-}$, the *Acta2* mRNA level increased continuously. In Postn$^{-/-}$ mice, the *Acta2* mRNA level was quite constant increased. Relative quantification of gene expression was calculated with ΔΔCT-method to *Gapdh* and normalized to Ctrl sham mice. Data are expressed as means ± SEM (n=5-6), Kruskal-Wallis test.

1.3.4. Analysis of the DR

The analysis of the K1C19 expression showed that the DR is limited to the portal and periportal area at all time points. Three days after the BDL, control mice showed new biliary cells in the portal tract. With increasing liver damage, the amount of new bile ducts increased. The DR was clearly visible in the enlarged portal tracts on day seven. After 21 days, the amount of the DR further increased and the morphology changed as well (mean BD/PT: 4.55; Fig. 26). The new bile ducts were larger and well formed (Fig. 27 B).

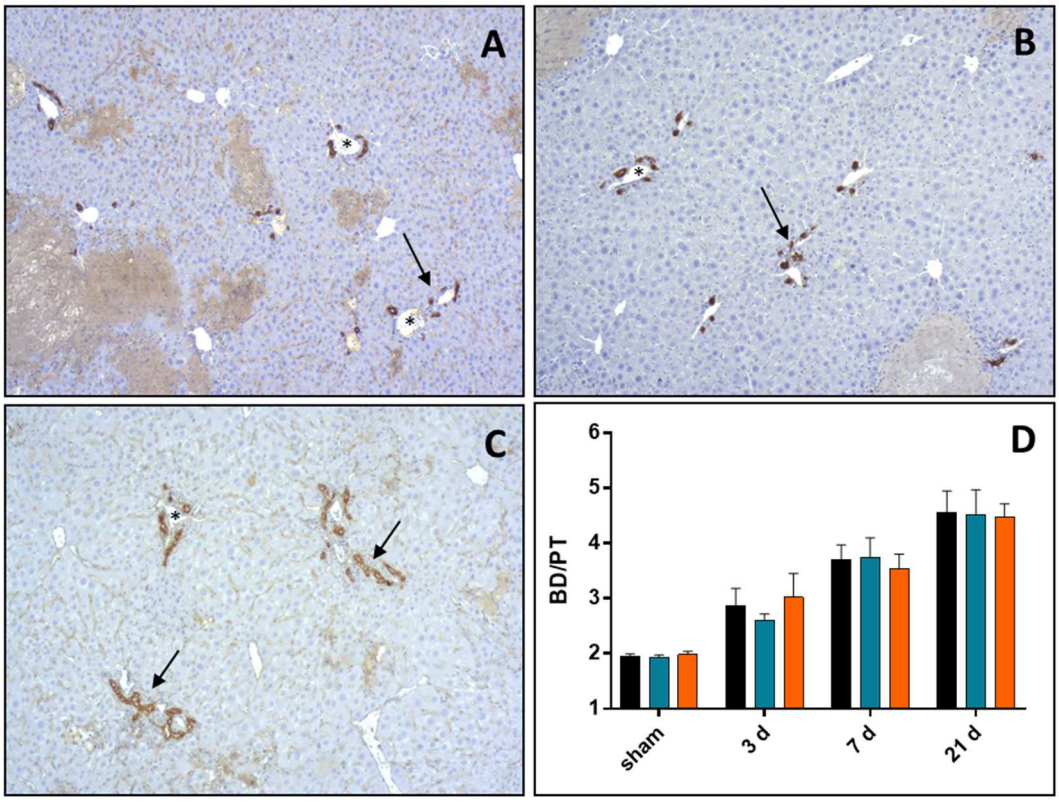

Fig. 26: Increased DR after BDL. Representative K1C19 stainings of control mice after 3 (A), 7 (B) and 21 days (C). The DR (arrows) started in the portal/periportal area. With progressive liver damage, the DR increased and portal tracts (asterisks) got enlarged. New bile ducts got larger and were well formed. Quantification of BD/PT based on the immunoreactivity for K1C19, black bars: Ctrl, blue bars: $Tnc^{-/-}$, orange bars: $Postn^{-/-}$. Data are expressed as means ± SEM (n=5-6), Kruskal-Wallis test (D). A-C: 10x.

In the liver of $Postn^{-/-}$ mice, the DR was limited to the portal tract just as in control mice. They also showed small new bile ducts in the portal tract after three days. After seven days, the DR was slightly lower compare to control mice. On day 21, the amount of new bile ducts was similar (mean BD/PT: 4.47; Fig. 26), the only differences were observed in the architecture. In general, new bile ducts were smaller and appeared with a more irregular shape compared to control mice (Fig. 27 A).

$Tnc^{-/-}$ mice showed the same distribution pattern and morphology of the DR as control mice. After three days, the amount of new bile ducts was slightly lower, but with increasing liver damage, it further increased as well. Therefore, $Tnc^{-/-}$ mice showed the same amount of bile ducts (mean BD/PT: 4.52; Fig. 26) after 21 days nearly. The morphology of new bile ducts was like the DR in control mice (Fig. 27 C).

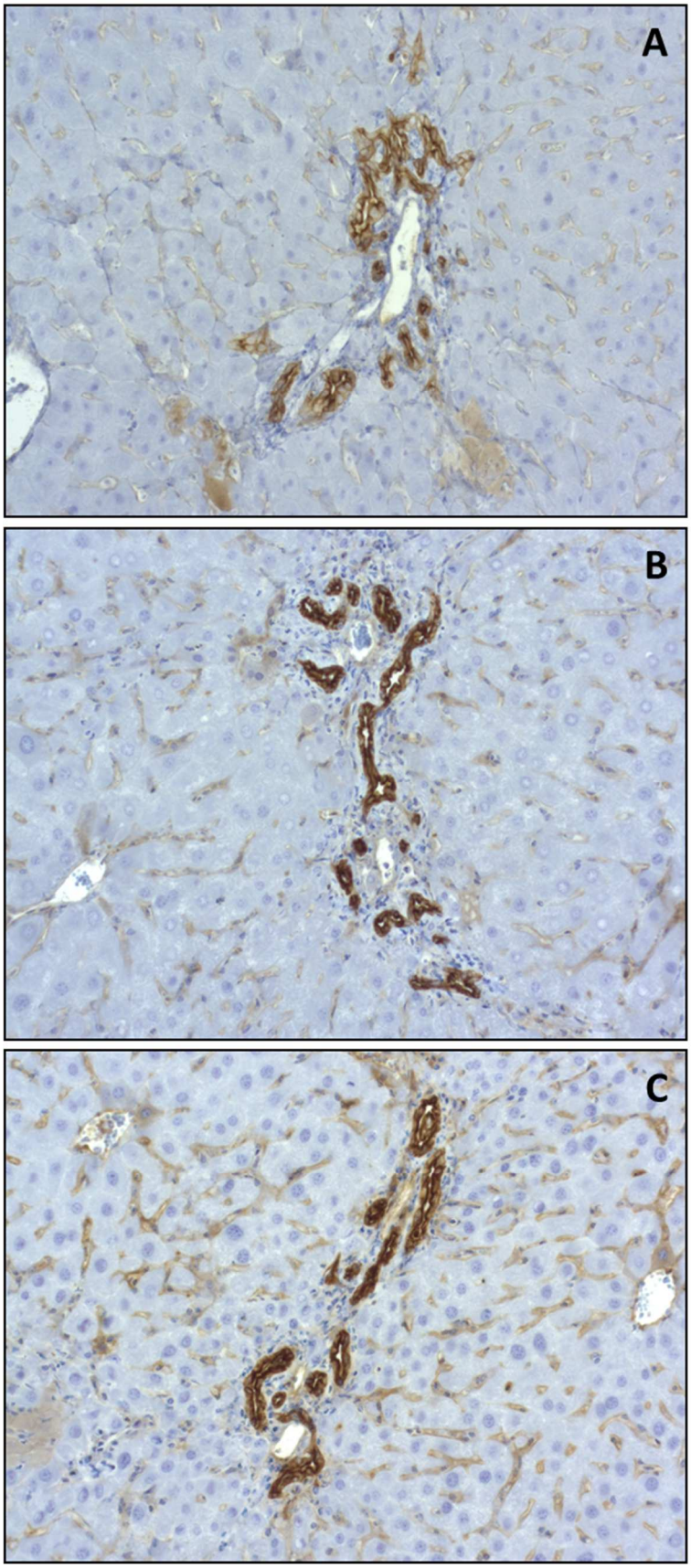

Fig. 27: DR 21 days after BDL. Representative K1C19 stainings of Postn$^{-/-}$ (A), control (B) and Tnc$^{-/-}$ mice (C). Postn$^{-/-}$ mice showed average smaller BD with a more irregular shape compared to Tnc$^{-/-}$ and control mice. A-C: 20x.

The mRNA level of *K1c19* was increased after BDL. In control mice, the gene expression of *K1c19* increased and was quite constant until seven days after BDL. Afterwards the *K1c19* mRNA level increased to a maximum on day 21. The same trend was observed in Postn$^{-/-}$ mice, though the mRNA expression was always lower compared to control mice. Compared to that in Tnc$^{-/-}$ mice, the *K1c19* expression level continuously increased. After three and 21 days, the expression was lower and after seven days higher compared to control mice. Finally, there was no significant difference observed among the three genotypes at any time point (Fig. 28).

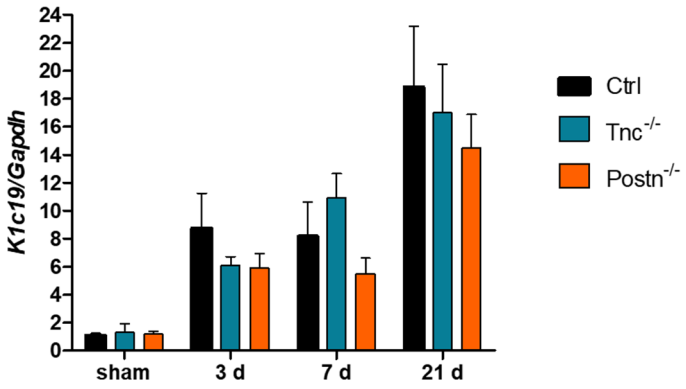

Fig. 28: Increased mRNA level of *K1c19* after BDL. In control and Postn$^{-/-}$ mice, the *K1c19* mRNA expression was quite constant increased after three and seven days and further increased on day 21. In Tnc$^{-/-}$ the *K1c19* mRNA level increased continuously. Relative quantification of gene expression was calculated with ΔΔCT-method to *Gapdh* and normalized to Ctrl sham mice. Data are expressed as means ± SEM (n=5-6), Kruskal-Wallis test.

1.3.5. HPC analysis

The SOX9 expression was evaluated to analyze the amount and distribution of HPC. Three days after the BDL, control mice expressed SOX9 in biliary cells as well as in hepatocytes. SOX9^{+} hepatocytes were mainly located in zone one and around necrotic areas. Furthermore, SOX9 was expressed with a portal to central gradient: hepatocytes in the periportal area were strongly stained whereas hepatocytes closer to the CV were stained weaker. Biliary cells were always strongly stained. The gradient was also present after seven days, but the SOX9 expression was in general slightly decreased. Periportal hepatocytes were still the strongest stained cells as well as the cells of the DR. After 21 days, the intensity of SOX9 in hepatocytes further decreased and the mean H-Score was 69.3. Biliary cells were

the predominant cells, which expressed SOX9 (Fig. 29; Fig. 30 A, D).

Postn$^{-/-}$ and Tnc$^{-/-}$ mice showed the same expression pattern of SOX9 than control mice. Compared to control mice, Postn$^{-/-}$ mice showed a lower expression at any time (Fig. 30 C, D). Tnc$^{-/-}$ mice showed first a higher but, in the end, a lower SOX9 expression in hepatocytes than control mice (Fig. 30 B, D). After 21 days, the H-Score in Postn$^{-/-}$ mice decreased to 52.9 and in Tnc$^{-/-}$ mice to 63.1 (Fig. 30 D).

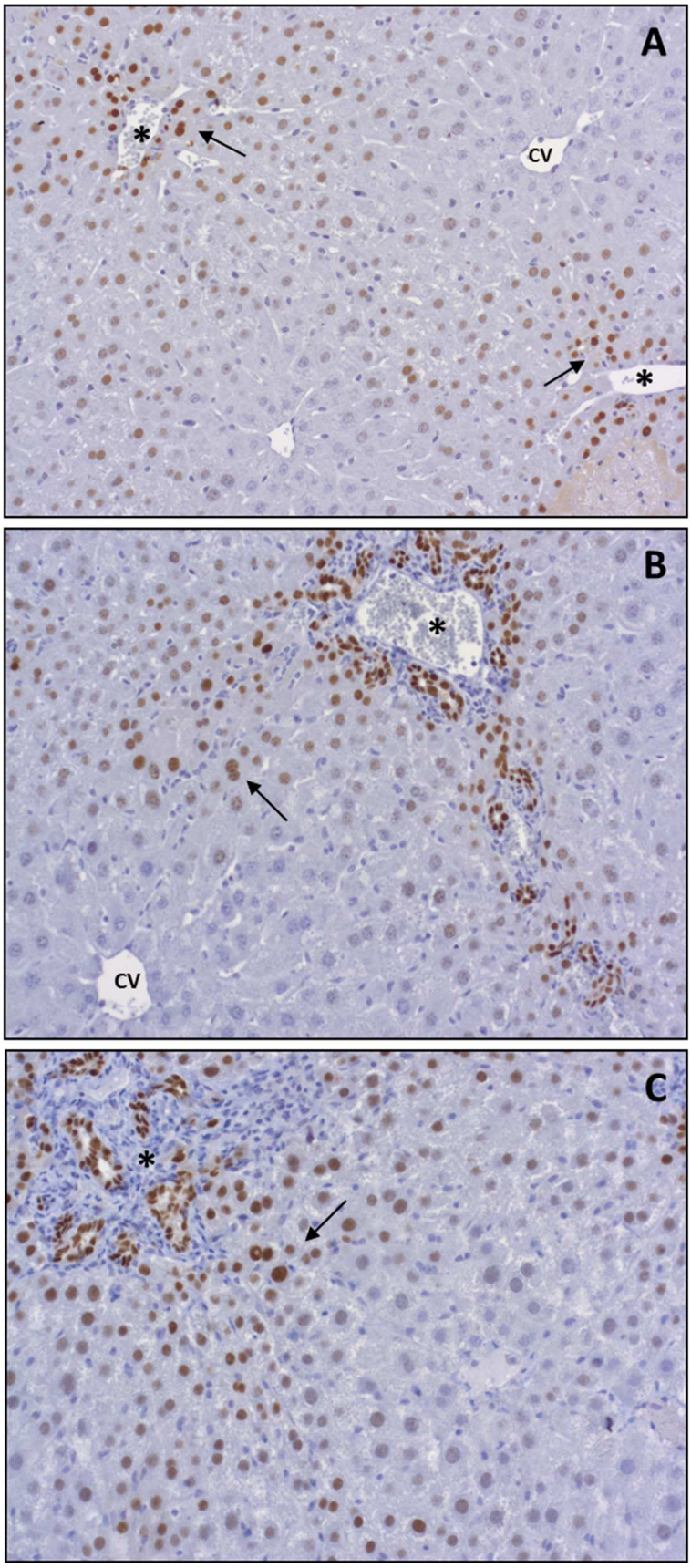

Fig. 29: SOX9 expression in control mice after BDL. Representative SOX9 stainings after 3 (A), 7 (B) and 21 days (C). SOX9 was expressed in hepatocytes (arrows) with a porto-central gradient at any timepoint. The intensity decreased from the portal tracts

(asterisks) to the central vein (CV). A-C: 20x.

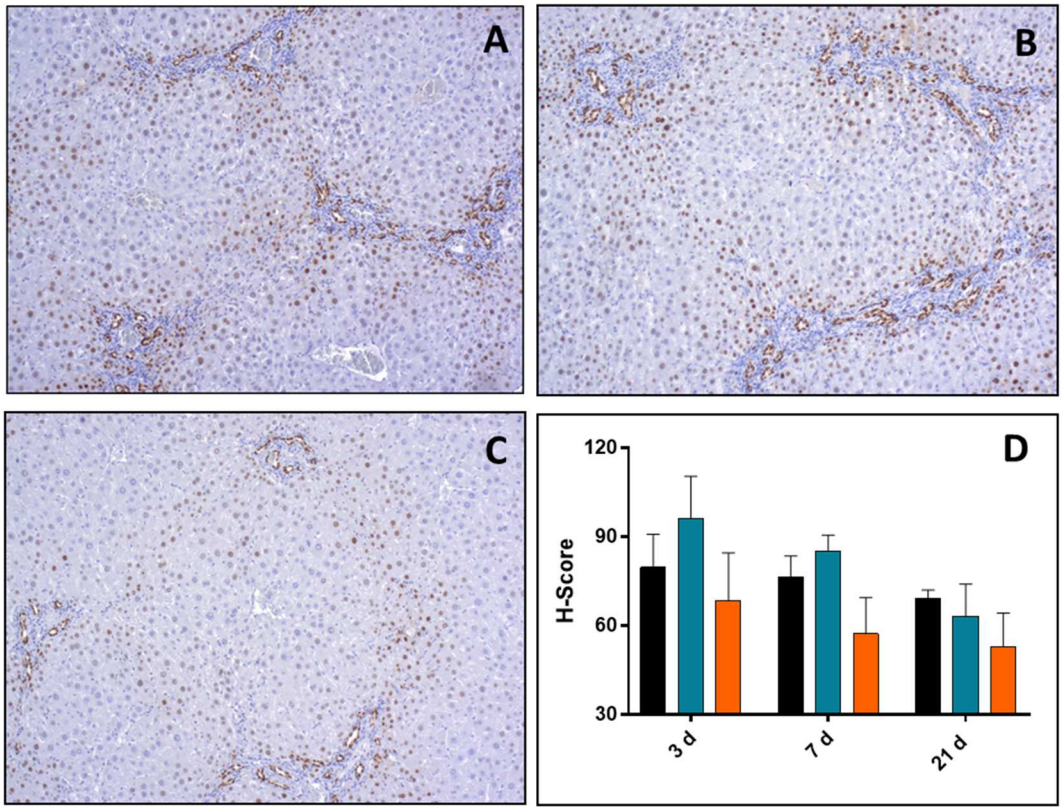

Fig. 30: SOX9 expression 21 days after BDL. Representative SOX9 stainings of control (A), $Tnc^{-/-}$ (B) and $Postn^{-/-}$ mice (C). After 21 days, $Tnc^{-/-}$ and $Postn^{-/-}$ mice showed a weaker expression of SOX9 in hepatocytes as control mice. Quantification of HPC by using the H-Score, based on the immunoreactivity of hepatocytes (D). Black bars: Ctrl, blue bars: $Tnc^{-/-}$, orange bars: $Postn^{-/-}$. Data are expressed as means ± SEM (n=5-6), Kruskal-Wallis test. A-C: 10x.

The mRNA level of *Sox9* in control mice was quite constant increased with a maximum after 21 days. In $Postn^{-/-}$ mice, the *Sox9* mRNA just slightly increased. After three and seven days, it was always lower compared to control mice. After 21 days, the mRNA expression was comparable to control mice. $Tnc^{-/-}$ mice always showed a higher *Sox9* mRNA level as control mice. It was quite constant with a peak after three days (Fig. 31).

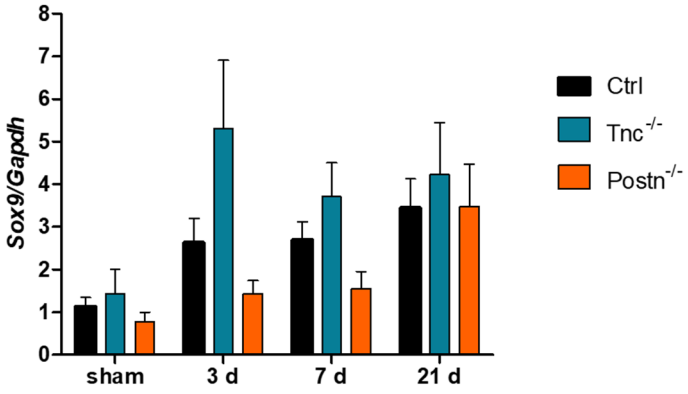

Fig. 31: Increased mRNA level of *Sox9* after BDL. In control mice, the *Sox9* mRNA expression was quite constant increased with a maximum 21 days after BDL. Compared to control mice, Postn$^{-/-}$ showed a lower *Sox9* expression after three and seven and a similar after 21 days. Tnc$^{-/-}$ mice showed a quite constant increased *Sox9* level, which was always a higher as in control mice. Relative quantification of gene expression was calculated with ΔΔCT-method to *Gapdh* and normalized to Ctrl sham mice. Data are expressed as means ± SEM (n=5-6), Kruskal-Wallis test.

1.3.6. Analysis of the HPI

The analysis of the MKI67 expression shows that the proliferation of the hepatocytes is a diffuse process in the parenchyma of the liver. It was diffusely expressed in the hepatocytes of any genotype at any point of time. Control mice showed a continuously increased hepatocellular proliferation rate until a peak of 16.8% on day seven. After 21 days, the HPI decreased to an average of 11.63% (Fig. 32; Fig. 33 B, E).

Postn$^{-/-}$ mice showed a different trend in the proliferation rate of hepatocytes. The HPI was always higher than in control mice. It was quite constant with a maximum of 23.4% at day seven. After 21 days, the HPI was 21.4% (Fig. 32, D; Fig. 33, A, C). Tnc$^{-/-}$ showed the same trend as control mice. The proliferation rate increased until 27.04% at day 7. Afterwards, the HPI was decreased on day 21 as well (HPI: 8.23%). Tnc$^{-/-}$ mice showed a higher HPI after three and seven days and after 21 days a lower HPI than control mice (Fig. 32 D; Fig. 33 C, F).

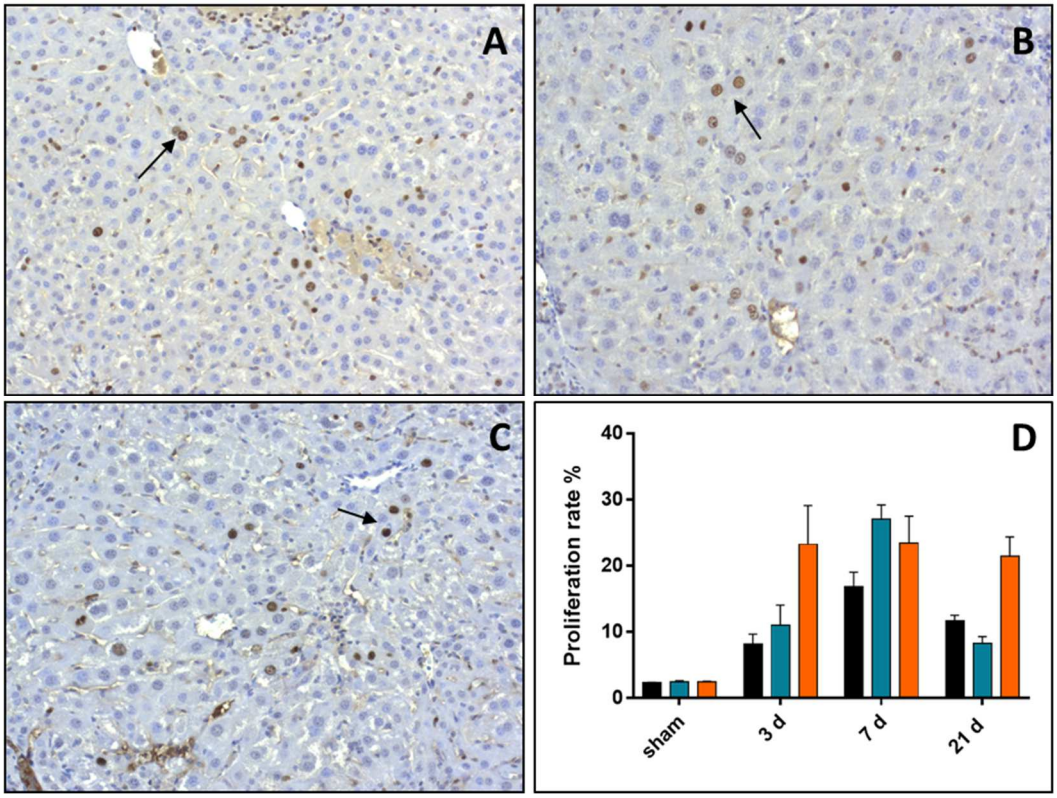

Fig. 32: Increased hepatocellular proliferation rate after BDL. Representative MKI67 stainings of control mice after 3 (A), 7 (B) and 21 days (C) demonstrate a diffuse proliferation of hepatocytes (arrows). D: Quantification of the HPI showed a peak after 7 days in control and $Tnc^{-/-}$ mice. $Postn^{-/-}$ mice showed a constant increased HPI. Black bars: Ctrl, blue bars: $Tnc^{-/-}$, orange bars: $Postn^{-/-}$. Data are expressed as means ± SEM (n=5-6), Kruskal-Wallis test. A-C: 20x.

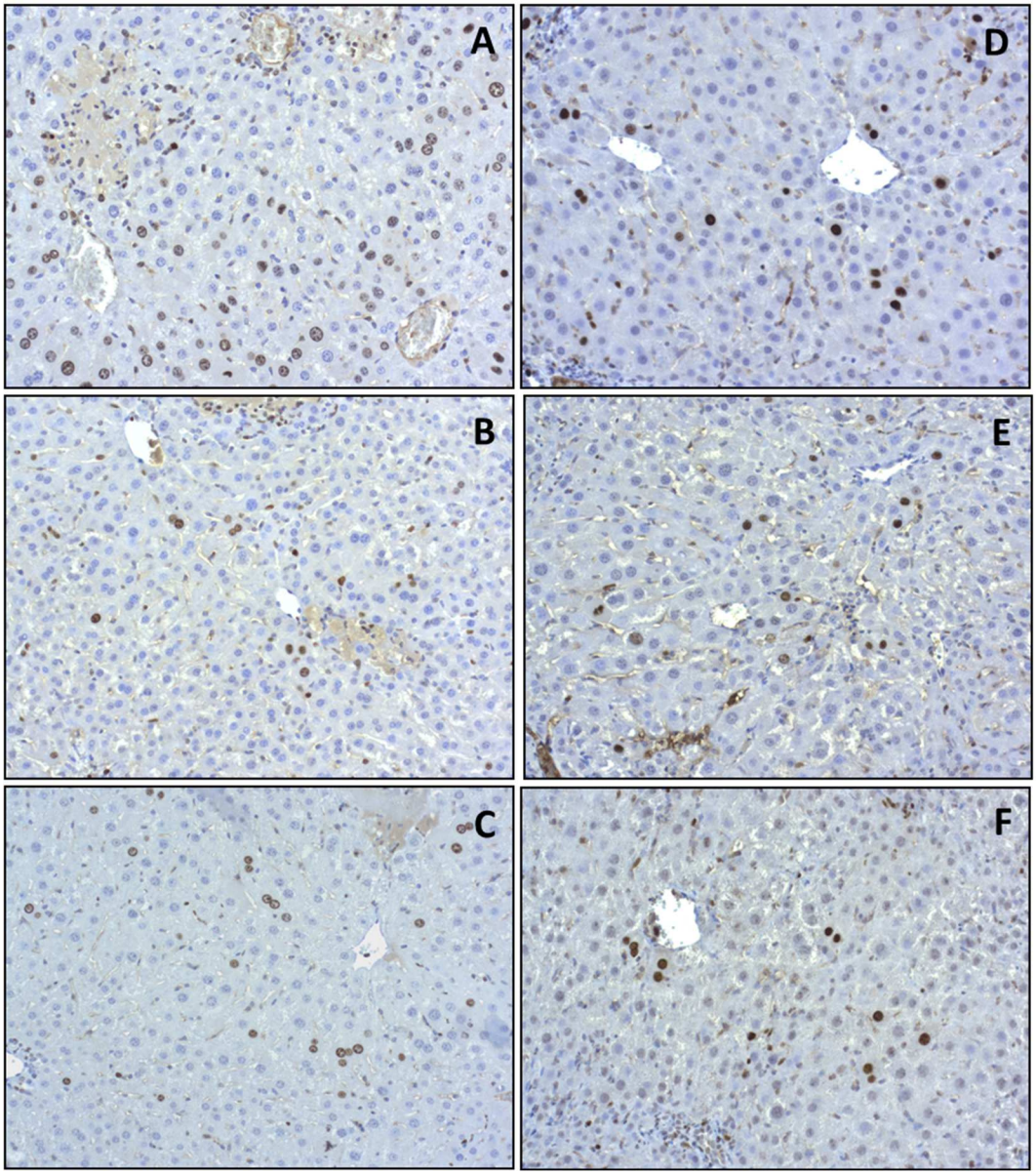

Fig. 33: Hepatocellular proliferation rate 3 (A-C) and 21 days (D-F) after the BDL. Representative MKI67 staining of $Postn^{-/-}$ (A, D), control (B, E) and $Tnc^{-/-}$ mice (C, F). $Postn^{-/-}$ mice showed after 3 and 21 days more proliferating hepatocytes as control mice. $Tnc^{-/-}$ showed after 3 less and after 21 days more proliferating hepatocytes compared to control mice. A-F: 20x.

In conclusion, the immunohistochemical analysis of the murine liver tissue reveal that POSTN and TNC are not expressed in the normal liver but increased with liver damage after BDL. The amount of aHSC and the DR increase as well in parallel with liver damage and fibrosis. Furthermore, the surgery induces a diffuse proliferation of mature hepatocytes and an expression of the progenitor marker SOX9. Although there are trends between the three genotypes in the respective stainings, the differences do not achieve statistical significance.

2. Results of the carbon tetrachloride model

The CCl_4-model was used to induce a toxin-mediated liver damage and to study the resulting fibrosis as well as the regeneration afterwards.

2.1. Results of the CCl_4 "Fibrosis" model

The mice used in this model were sacrificed after 2, 4 or 8 weeks of CCl_4 treatment.

2.1.1. Necroscopies

All sham mice showed no abnormalities of the general condition, of the peritoneal cavity as well as a normal liver and gallbladder. After two weeks of CCl_4 treatment the peritoneal cavity as well as the liver of all genotypes showed no evidence of a pathological condition. After four weeks of treatment, occasionally mild adhesions between the liver and intestine were observed among all genotypes. The liver was slightly lighter, and the surface was rougher. After eight weeks, the adhesions got worse and both knockouts showed less abdominal adhesions compared to control mice (Fig. 34).

The analyses of the LBW-r. % identified a mild increase after eight weeks of CCl_4 treatment among all three genotypes without a significant difference (Fig. 35).

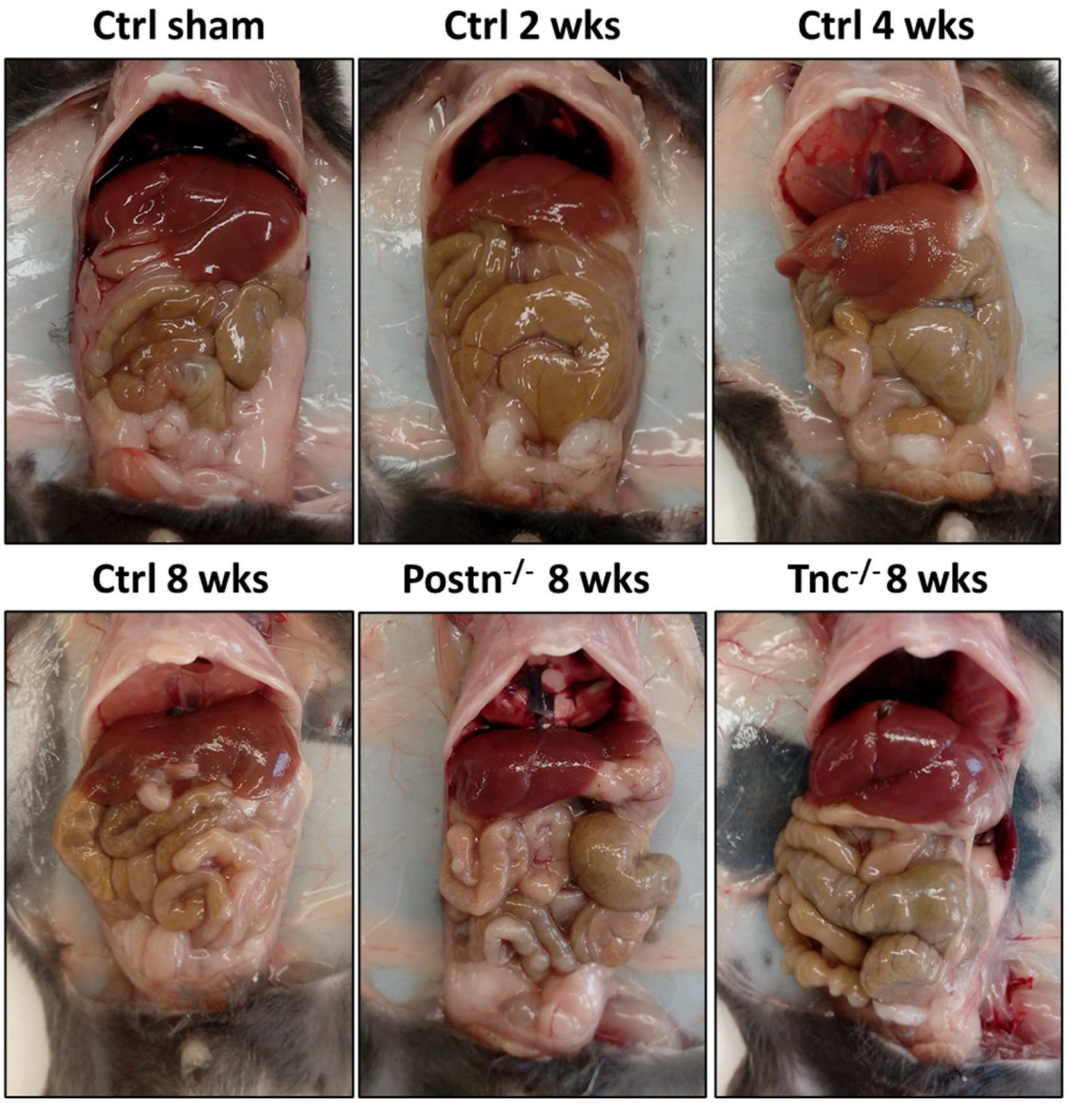

Fig. 34: The liver after the CCl_4 treatment. The surface of the liver got rougher with progressive liver damage. After 8 weeks, $Postn^{-/-}$ and $Tnc^{-/-}$ mice showed less abdominal adhesions compared to control mice.

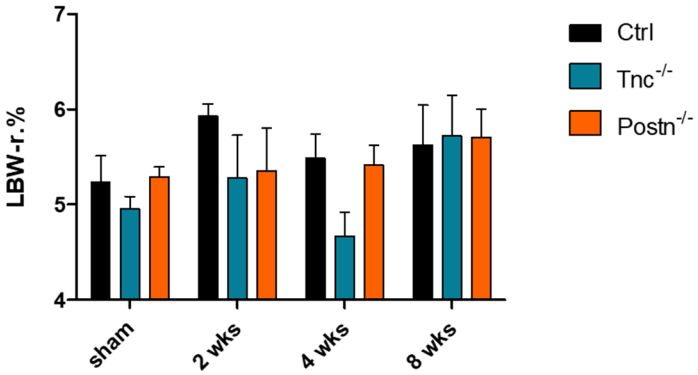

Fig. 35: LBW-r. % after the CCl_4 treatment. The LBW-r. % was increased among all genotypes after eight weeks. Data are expressed as means ± SEM (n=3-6), Kruskal-Wallis

test.

2.1.2. Results of the histological stainings

Different histological stainings were evaluated for the characterization of the liver tissue after a toxic injury. All mice from the sham groups showed a normal liver tissue (data not shown).

2.1.2.1. Inflammation analysis

In the HE staining, control mice showed a moderate inflammation of the liver tissue after two weeks of CCl_4 treatment. Inflammatory cells and necrotic hepatocytes were localized around the central vein. With progressive liver damage, the area of confluent necroses and number of single-cell necroses increased. Thereby, occasional bridges of necrotic hepatocytes were formed after the eight weeks CCl_4 treatment. There was no interface hepatitis or inflammation of the portal tracts observed at any point of time. The inflammatory activity increased with ongoing liver injury to a mean mHAI Score of 5.33 and was moderate at any time (Fig. 36; Fig. 37 B).

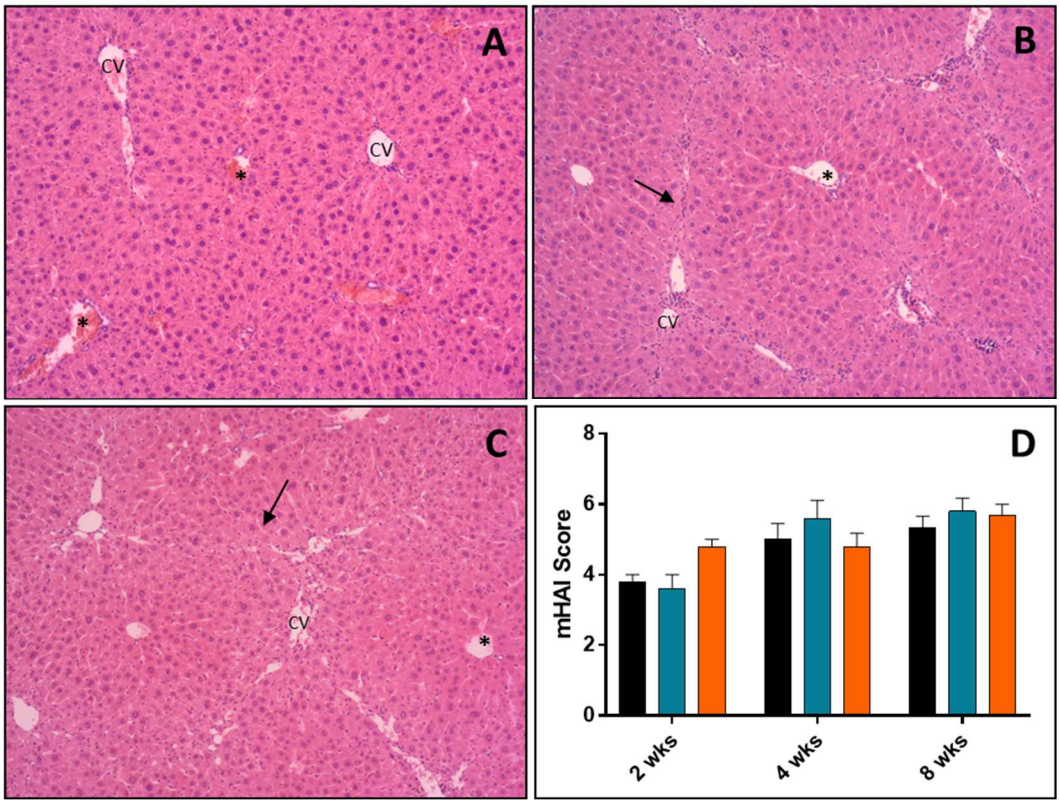

Fig. 36: Increased inflammatory activity during the CCl_4 treatment. Representative HE stainings of control mice after 2 (A), 4 (B) and 8 weeks (C). Necrotic hepatocytes (arrows) are around central veins (CV) and form occasional centro-central bridges. There was no

inflammation in the portal tract (asterisk) observed. Grading by using the mHAI Score, black bars: Ctrl, blue bars: $Tnc^{-/-}$, orange bars: $Postn^{-/-}$. Data are expressed as means ± SEM (n=3-6), Kruskal-Wallis test (D). A-C: 10x

Both knockout mice showed the same pattern of inflammatory activity. $Postn^{-/-}$ mice showed a slightly higher amount of necrotic and inflamed tissue compared to control mice after two and eight weeks. The mHAI Score increased up to a mean of 5.67 after eight weeks (Fig. 36 D; Fig. 37 A). $Tnc^{-/-}$ mice showed a mildly higher inflammatory activity as control mice after four and eight weeks. Thereby, the mHAI Score increased up to 5.8 (Fig. 36 D; Fig. 37 C).

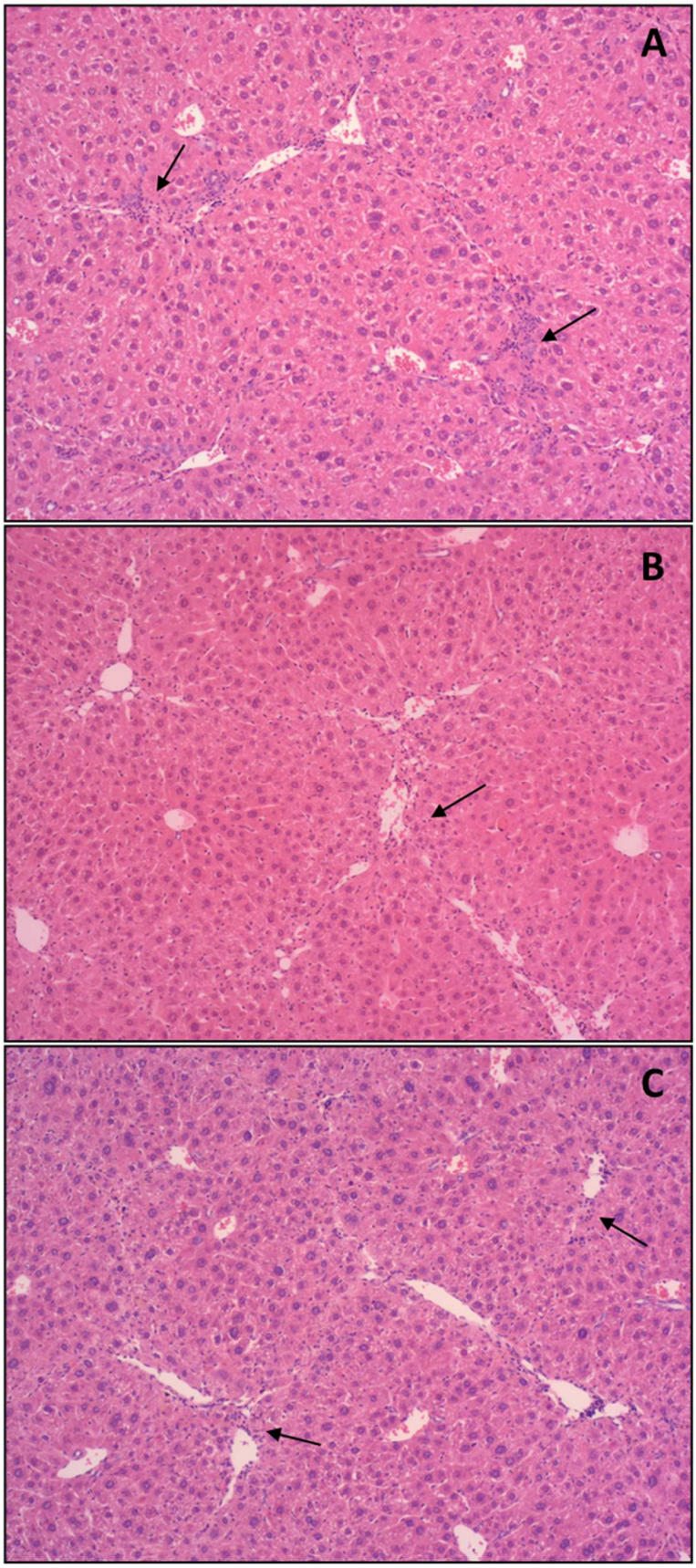

Fig. 37: Increased inflammatory activity after eight weeks CCl_4 treatment. Representative HE stainings of Postn$^{-/-}$ (A), control (B) and Tnc$^{-/-}$ mice (C). Postn$^{-/-}$ and Tnc$^{-/-}$ mice showed a slightly higher inflammation of the liver tissue compared to control

mice. A-C: 10x.

2.1.2.2. Analysis of fibrosis stage

The fibrosis stages during the CCl_4 treatment were determined by using the PSR staining. Control mice showed radial collagen fibers around the CV after two weeks. These fibers form thin and predominantly incomplete centro-central septa. Occasional, complete septa could be observed. With ongoing liver injury, more collagen was accumulating. Therefore, an increased amount of complete fibrous septa was present and isolated complete nodules were formed after four weeks of CCl_4. After eight weeks of CCl_4 treatment, the septa were thick and clearly marked. The fibrous scar formed multiple nodules and control mice showed a mean modified Ishak Score of 7.17 (Fig. 38; Fig. 39 B, E).

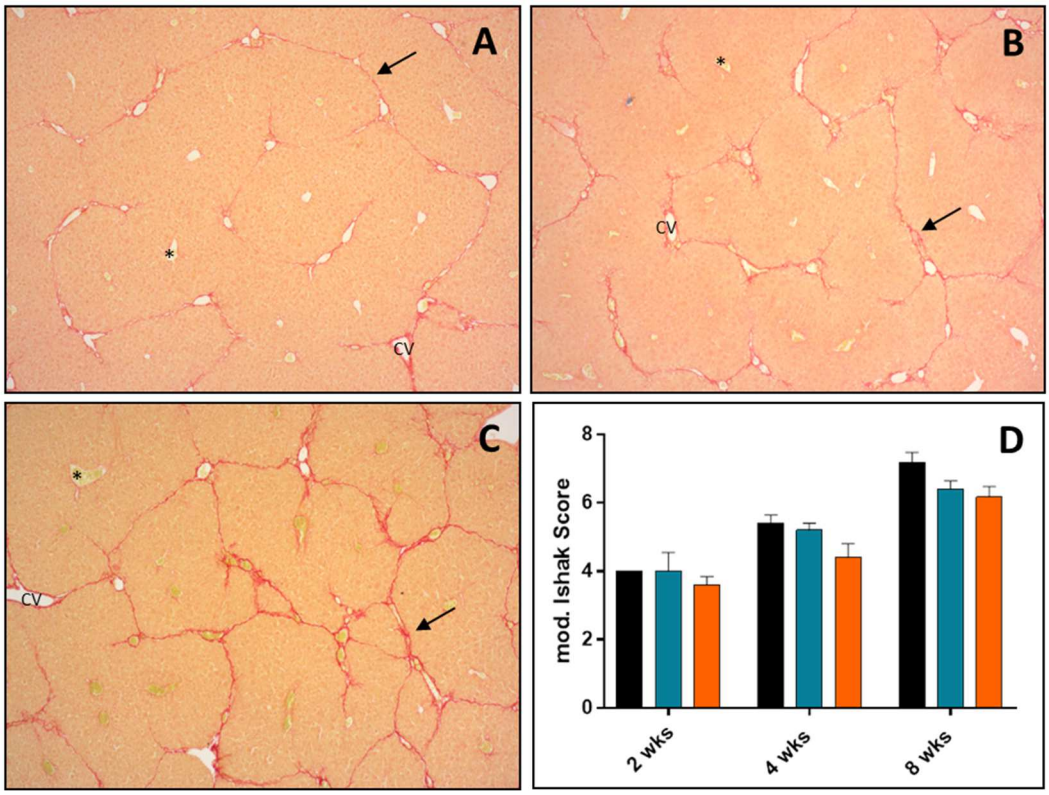

Fig. 38: Increased deposition of Collagen I and III after CCl_4 treatment. Representative PSR stainings of control mice after 2 (A), 4 (B) and 8 weeks (C). Increased collagen deposition (arrows) around central veins (CV). A normal collagen expression was observed in portal tracts (asterisks). D: Staging according to the modified Ishak Score. Black bars: Ctrl, blue bars: $Tnc^{-/-}$, orange bars: $Postn^{-/-}$. Data are expressed as means ± SEM (n=3-6), Kruskal-Wallis test. A-C: 5x.

Postn$^{-/-}$ and Tnc$^{-/-}$ mice showed the same fibrosis pattern as control mice. In Postn $^{-/-}$ mice, the collagen deposition was always lower than in control mice. After eight weeks of CCl_4, they had thinner septa and less complete nodules. The mean modified Ishak Score amounts to 6.17 (Fig. 38 D; Fig. 39 A, D). Tnc$^{-/-}$ mice presented a similar fibrotic response after two and four weeks. After eight weeks of treatment, Tnc$^{-/-}$ mice showed a lower amount of collagen compared to control mice with a mean modified Ishak Score of 6.2 (Fig. 38 D; Fig. 39 C, F).

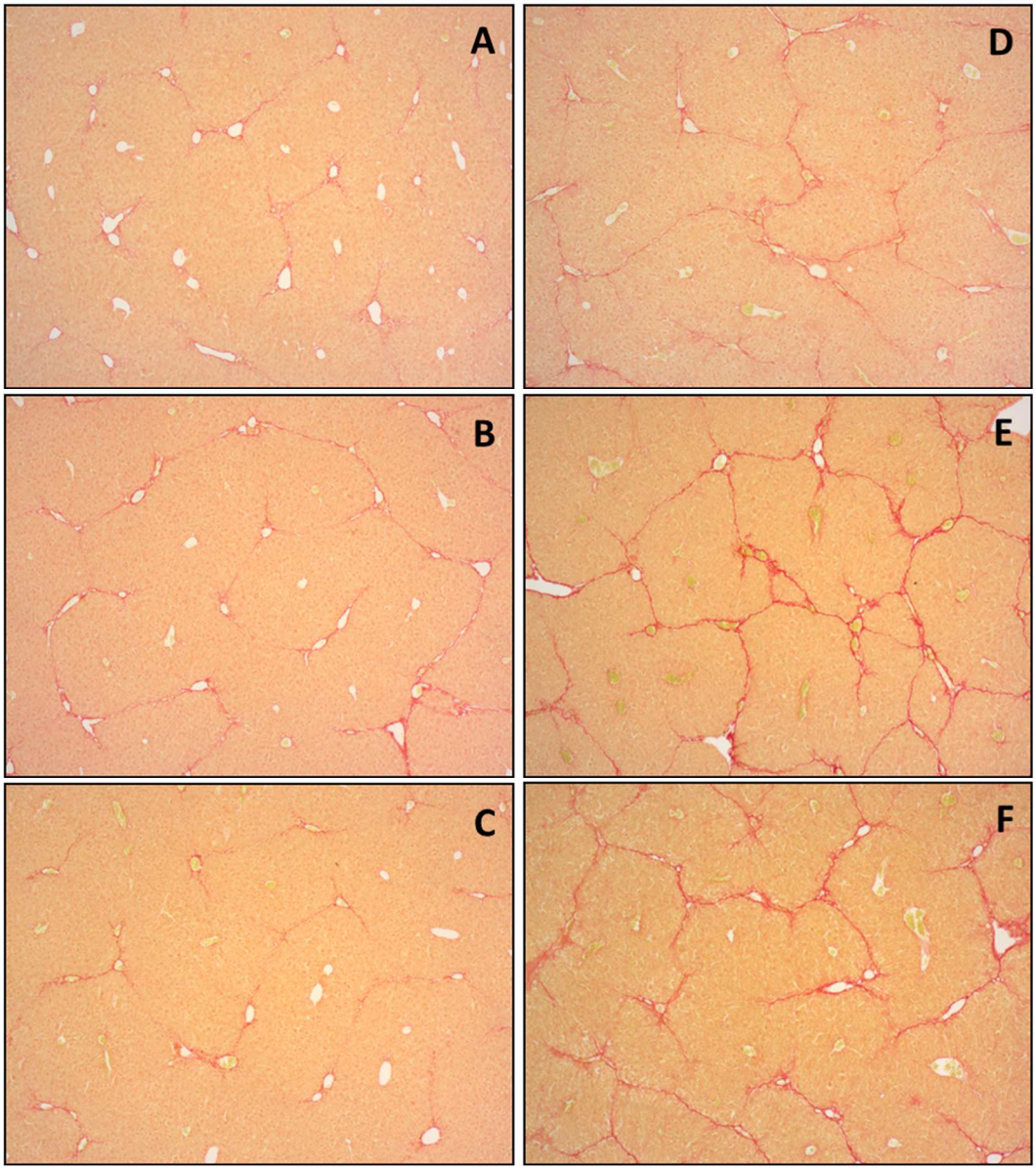

Fig. 39: Collagen deposition after a two (A-C) and eight weeks (D-F) CCl_4 treatment. Representative PSR stainings of Postn$^{-/-}$ (A, D), control (B, E) and Tnc$^{-/-}$ mice (C, F). The collagen deposition increased with ongoing treatment. Postn$^{-/-}$ mice showed always lower collagen deposition compared to control mice. Tnc$^{-/-}$ mice showed after two weeks a similar and after eight weeks a slightly lower collagen deposition as control mice. A-F: 5x.

In conclusion, Postn$^{-/-}$ and Tnc$^{-/-}$ mice predominantly show the same trend of the inflammatory reaction, but the tendency towards a reduced fibrotic reaction after eight weeks of CCl_4 compared to control mice.

2.1.3. Results of the immunohistochemistry and corresponding qRT-PCR

Different markers for the immunohistochemistry and the qRT-PCR were used for a more detailed characterization of the liver tissue in course of a toxic damage.

2.1.3.1. Periostin

After two weeks of CCl_4 treatment, control mice showed predominantly no POSTN expression. It was only occasionally detectable in or around the wall of less than 25% of the CV. After four weeks, the POSTN expression slightly increased. Its expression was still limited to the wall of less than 25% of the CV. With ongoing liver damage, its expression increased. POSTN was detectable in/around the wall of 25-50% of the CV. Thereby, thin lines around CV with occasional mild extensions in the parenchyma were observed after eight weeks (Fig. 41 A-C). Altogether, the expression of POSTN increased continuously to a mean POSTN Score of 2.5 (Fig. 40).

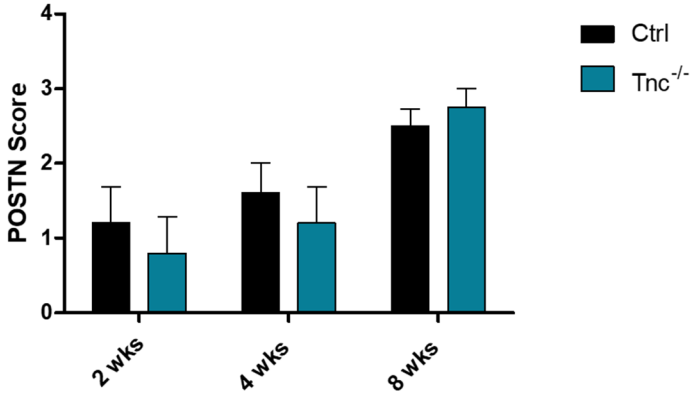

Fig. 40: Increased POSTN expression in control and Tnc$^{-/-}$ mice after CCl_4 treatment. POSTN expression was quantified by using a total score of intensity and distribution. After two and four weeks, Tnc$^{-/-}$ mice showed a lower POSTN expression as control mice, whereas it was slightly higher after eight weeks of CCl_4. Data are expressed as means ± SEM (n=3-6), Kruskal-Wallis test.

Tnc$^{-/-}$ mice showed the same pattern and progression of POSTN expression as control mice. After two and four weeks, the expression of POSTN was slightly

lower than in control mice. After eight weeks of the CCl_4, $Tnc^{-/-}$ mice showed a slightly higher expression with a mean POSTN Score of 2.75 (Fig. 40, Fig. 41 D-F).

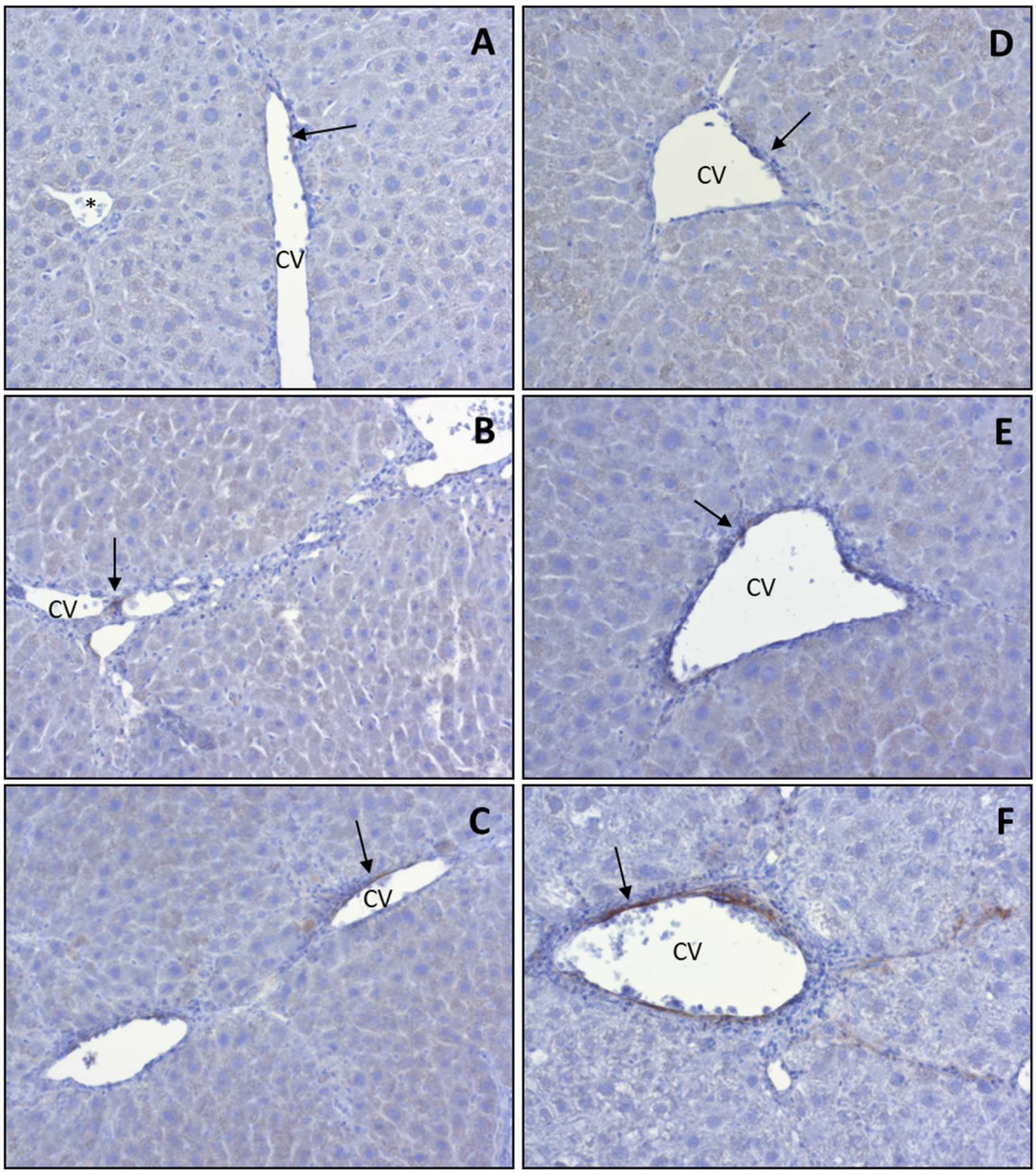

Fig. 41: Increased POSTN expression in control (A-C) and $Tnc^{-/-}$ mice (D-F) after CCl_4 treatment. Representative POSTN stainings after 2 (A, D), 4 (B, E) and 8 weeks (C, F). POSTN (arrows) was predominantly expressed in/around the wall of central veins (CV). $Tnc^{-/-}$ mice showed after two and four a lower and after eight weeks a slightly higher POSTN expression compared to control mice. Portal vein (asterisk). A-F: 20x.

The mRNA level of *Postn* continuously increased in control mice. In $Tnc^{-/-}$ mice, the *Postn* expression increased in the first four weeks and afterwards it was quite constant. The *Postn* expression was always higher compared to control mice (Fig. 42).

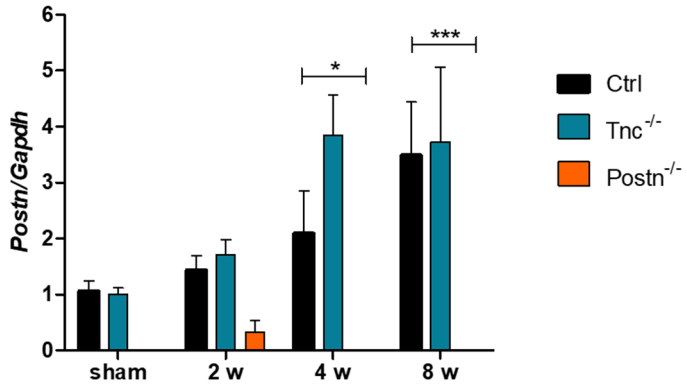

Fig. 42: Increased mRNA level of *Postn* after CCl_4 treatment. The *Postn* mRNA level increased continuously in control mice. In $Tnc^{-/-}$ mice it increased until four weeks and was afterwards quite constant, but in general always higher compared to control mice. Relative quantification of gene expression was calculated with ΔΔCT-method to *Gapdh* and normalized to Ctrl sham mice. Data are expressed as means ± SEM (n=3-6), Kruskal-Wallis test, * $P< 0.05$, ** $P< 0.01$, *** $P< 0.001$.

2.1.3.2. Tenascin C

After two weeks of CCl_4 treatment, control mice showed a weak and focal TNC expression. It was around of less than 50% of the CV with occasional radial extensions along fibrotic septa. After four weeks, the TNC expression increased around the CV and the fibrotic septa. With ongoing injury, TNC was also diffuse expressed in the parenchyma after eight weeks of treatment (Fig. 44 A-C). Altogether, the TNC expression increased continuously to a mean TNC Score of 4.5 (Fig. 43).

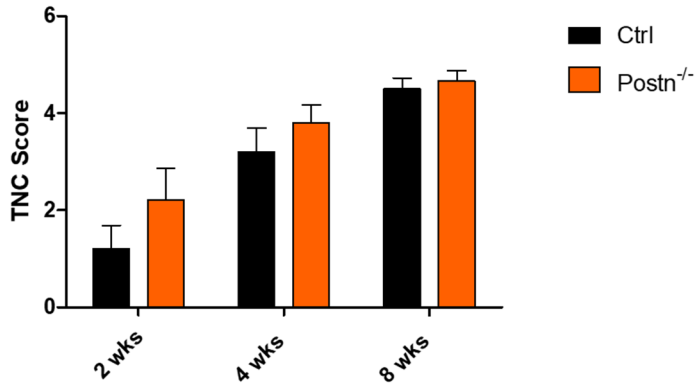

Fig. 43: Increasing TNC expression in control and $Postn^{-/-}$ mice after CCl_4 treatment. TNC expression was quantified by using a total score of intensity and distribution. $Postn^{-/-}$ mice showed an earlier increased TNC expression compared to control mice. Data are expressed as means ± SEM (n=3-6), Kruskal-Wallis test.

Postn$^{-/-}$ mice showed a higher expression of TNC in the early phase. After two weeks, TNC occurred occasionally diffuse in the parenchyma around the CV with a stronger expression along the fibrotic septa. The TNC expression further increased around the CV and along the fibrotic septa. After eight weeks, TNC was additionally expressed more diffusely in the parenchyma and the mean TNC Score increased to 4.67 (Fig. 43, Fig. 44 D-F).

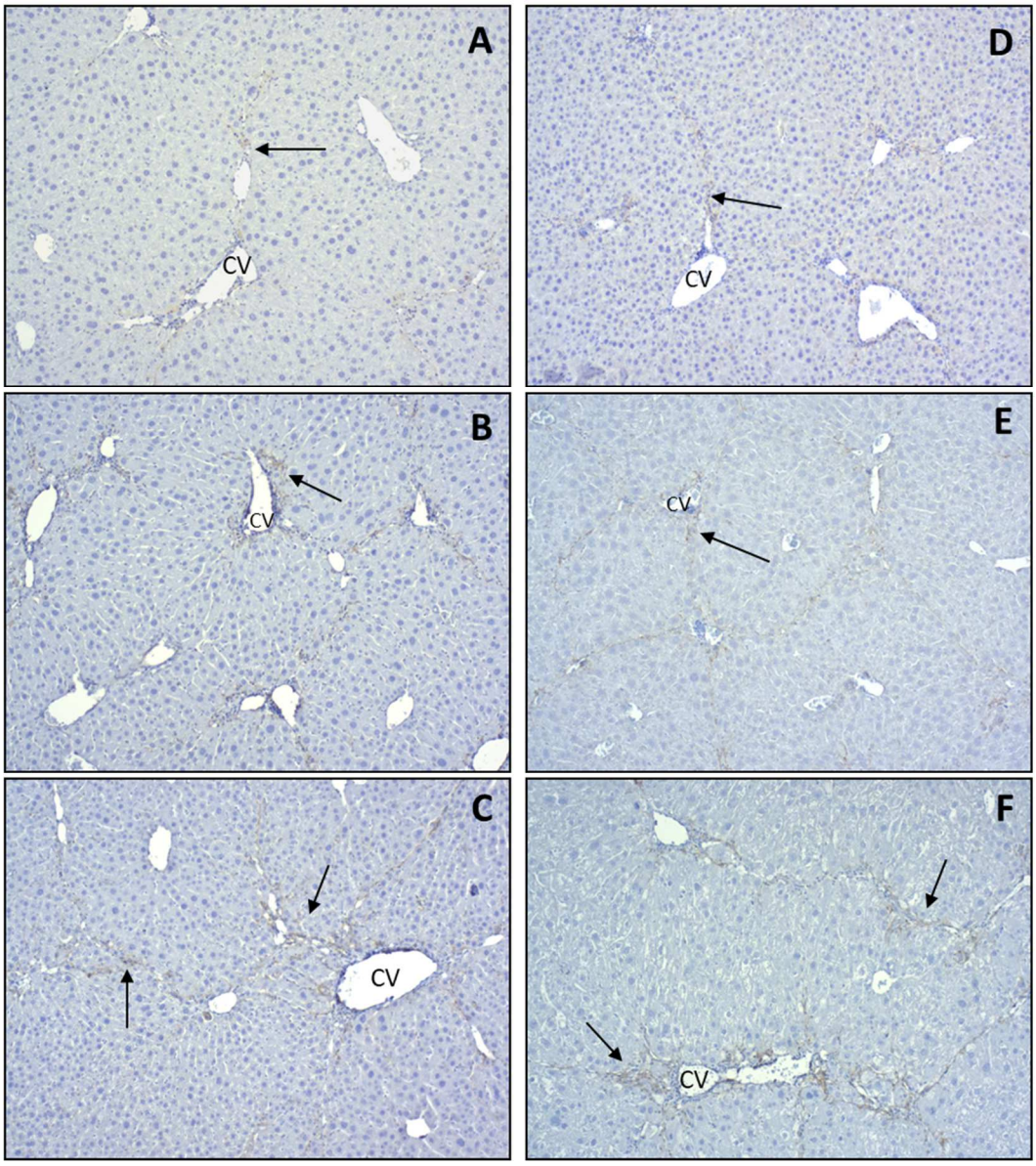

Fig. 44: Increasing TNC expression in control (A-C) and Postn$^{-/-}$ mice (D-F) after CCl_4 treatment. Representative TNC stainings after 2 (A, D), 4 (B, E) and 8 weeks (C, F). TNC expression (arrows) around central veins (CV) and along fibrotic septa in the parenchyma increased continuously with progressive liver damage. A-F: 10x.

The mRNA level of *Tnc* in control mice was only increased after eight weeks. In Postn$^{-/-}$ mice, the *Tnc* expression was already increased after two weeks. Afterwards, it slightly decreased and was quite constant over the time (Fig. 45).

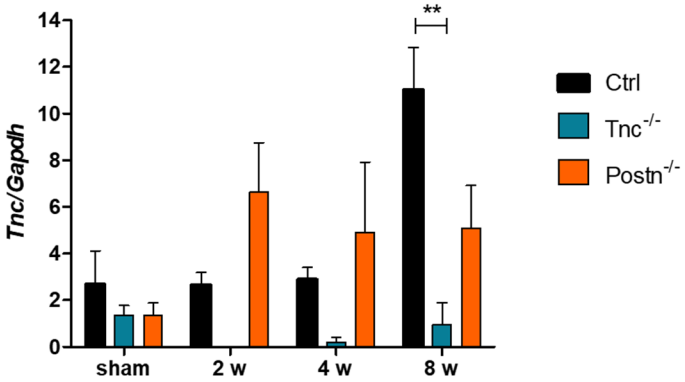

Fig. 45: Increased mRNA level of *Tnc* after CCl_4 treatment. In control mice, the *Tnc* expression was increased after eight weeks. In Postn$^{-/-}$ mice, the *Tnc* expression was increased after two weeks. Afterwards it slightly decreased and was more constant. Relative quantification of gene expression was calculated with ΔΔCT-method to *Gapdh* and normalized to Ctrl sham mice. Data are expressed as means ± SEM (n=3-6), Kruskal-Wallis test, * $P< 0.05$, ** $P< 0.001$.

2.1.3.3. Analysis of aMF

The localization and amount of aMF was determined by using ACTA2. The pattern of aMF differs in this toxic model compared to the cholestatic BDL model. After two weeks of CCl_4 treatment, control mice expressed ACTA2 mainly around CV with radial extension in the parenchyma. Multiple incomplete as well as complete centro-central septa of aMF have been observed. Moreover, occasional diffuse scattered ACTA2 positive cells have been identified in the parenchyma. During the treatment, the number of aMF increased. Therefore, multiple complete centro-central septa of aMF and a higher number in the parenchyma were detected after four weeks of CCl_4. After eight weeks, the number of aMF increased mainly in the parenchyma and the mean histopathologic Score increased to 17.5 (Fig. 46; Fig. 47 B, E).

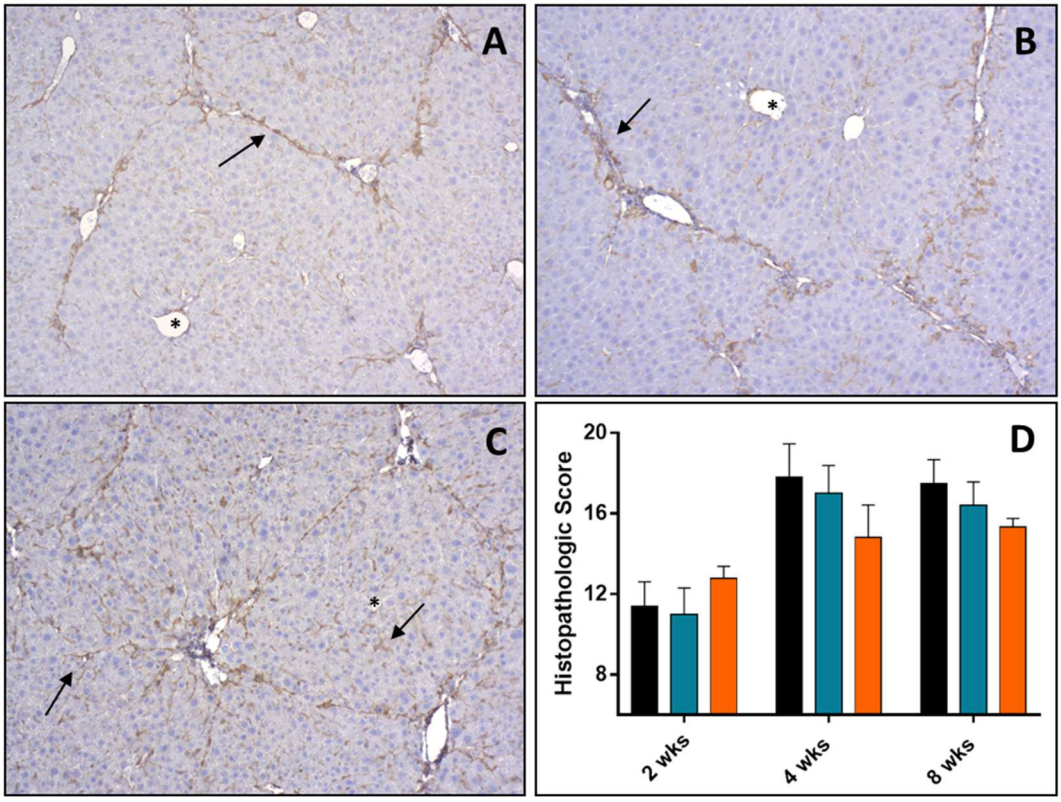

Fig. 46: Increased amount of aMF after the CCl_4 treatment. Representative ACTA2 stainings of control mice after 2 (A), 4 (B) and 8 weeks (C). Portal tracts (asterisks) showed the normal immunoreactivity for ACTA2. Activated MF (arrows) were mainly located in/around central veins. With progressive liver damage, the amount of aMF increased also in the parenchyma and they accumulated along fibrotic septa. D: Quantification of aMF based on the histopathologic Score. Black bars: Ctrl, blue bars: $Tnc^{-/-}$, orange bars: $Postn^{-/-}$. Data are expressed as means ± SEM (n=3-6), Kruskal-Wallis test. A-C: 10x.

$Postn^{-/-}$ and $Tnc^{-/-}$ mice showed the same expression pattern of ACTA2 as control mice. After two weeks, $Postn^{-/-}$ mice showed a slightly higher number of aMF. Compared to control mice, the increase of aMF was lower. Therefore, $Postn^{-/-}$ mice showed a lower amount of ACTA2 positive cells after four and eight weeks (Fig. 47 A, D). $Tnc^{-/-}$ mice showed about the same amount of aMF after two weeks as control mice. Instead, after four and eight weeks, a slightly lower amount of aMF was observed (Fig. 47 C, F). In the end, the ACTA2 expression increased to a mean histopathologic Score of 16.33 in $Postn^{-/-}$ mice and to 16.4 in $Tnc^{-/-}$ mice (Fig. 46 D).

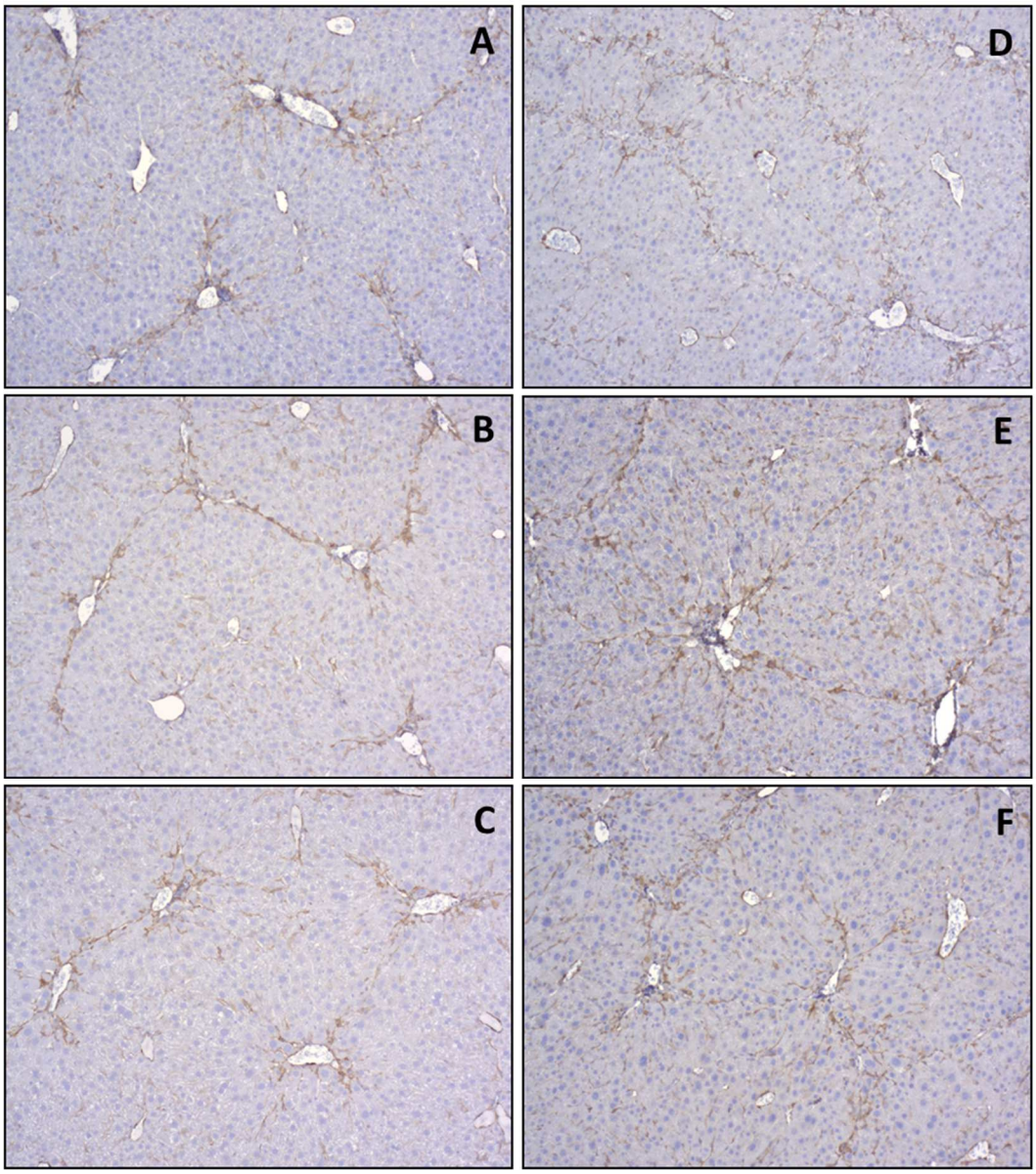

Fig. 47: Increased expression of ACTA2 after a two (A-C) and eight weeks (D-F) CCl_4 treatment. Representative ACTA2 stainings of $Postn^{-/-}$ (A, D), control (B, E) and $Tnc^{-/-}$ mice (C, F). $Postn^{-/-}$ mice showed after two weeks a higher and after eight weeks a lower amount of aMF compared to control mice. $Tnc^{-/-}$ mice showed after two weeks a similar and after eight weeks a lower amount of aMF as control mice. A-F: 10x.

The *Acta2* mRNA level in control mice only increased after eight weeks of CCl_4 treatment. In $Postn^{-/-}$ mice, the *Acta2* expression did not increase after the CCl_4 treatment and was significant lower after eight weeks compared to control mice. *Acta2* mRNA level in $Tnc^{-/-}$ mice just slightly decreased after two weeks and decreased afterwards (Fig. 48).

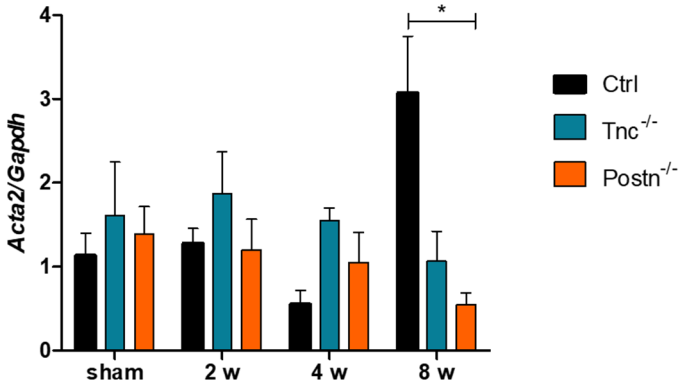

Fig. 48: The mRNA level of *Acta2* after CCl_4 treatment. In control mice, *Acta2* expression was only increased after eight weeks. In $Tnc^{-/-}$ and $Postn^{-/-}$ mice, *Acta2* was not or only minimal increased. Relative quantification of gene expression was calculated with ΔΔCT-method to *Gapdh* and normalized to Ctrl sham mice. Data are expressed as means ± SEM (n=3-6), Kruskal-Wallis test, * $P< 0.05$.

2.1.3.4. Analysis of the DR

The analysis of the K1C19 expression showed that the DR is a diffuse process in the parenchyma. An average between 40.33 and 42.83 bile ducts were detected and considered as normal. New scattered bile ducts cannot clearly allocate to a certain portal tract. In this toxic model, the DR increased with progressive fibrosis among all three genotypes. After two weeks of CCl_4 treatment, control mice showed an increased amount of new biliary cells predominantly around portal tracts. After four weeks, the pattern was more diffuse, and the DR increased. Finally, control mice showed an continuously increased amount with an average of 153.17 bile ducts after eight weeks of CCl_4 (Fig. 49, Fig. 50 B,E).

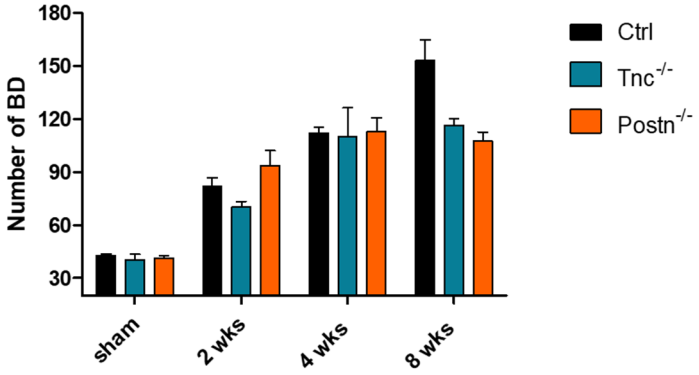

Fig. 49: Increased number of bile ducts after the CCl_4 treatment. In control mice, the DR increased continuously. In both knockout mice, the DR was lower after the eight weeks treatment compared to control mice. Data are expressed as means ± SEM (n=3-6),

Kruskal-Wallis test.

Postn$^{-/-}$ mice showed a higher number of new bile ducts than control mice after two weeks. However, the DR did not increase as strong as in control mice. Thus, Postn$^{-/-}$ mice showed a lower amount of bile ducts after eight weeks with an average of 111.14 new bile ducts (Fig. 49; Fig. 50 A, D). Tnc$^{-/-}$ showed a slightly lower number of bile ducts than control mice after two weeks. With ongoing treatment, the DR increased continuously to an average maximum of 116.6 bile ducts. Therefore, they showed less DR after an eight-weeks-CCl_4-treatment than control mice (Fig. 49; Fig. 50 C, F).

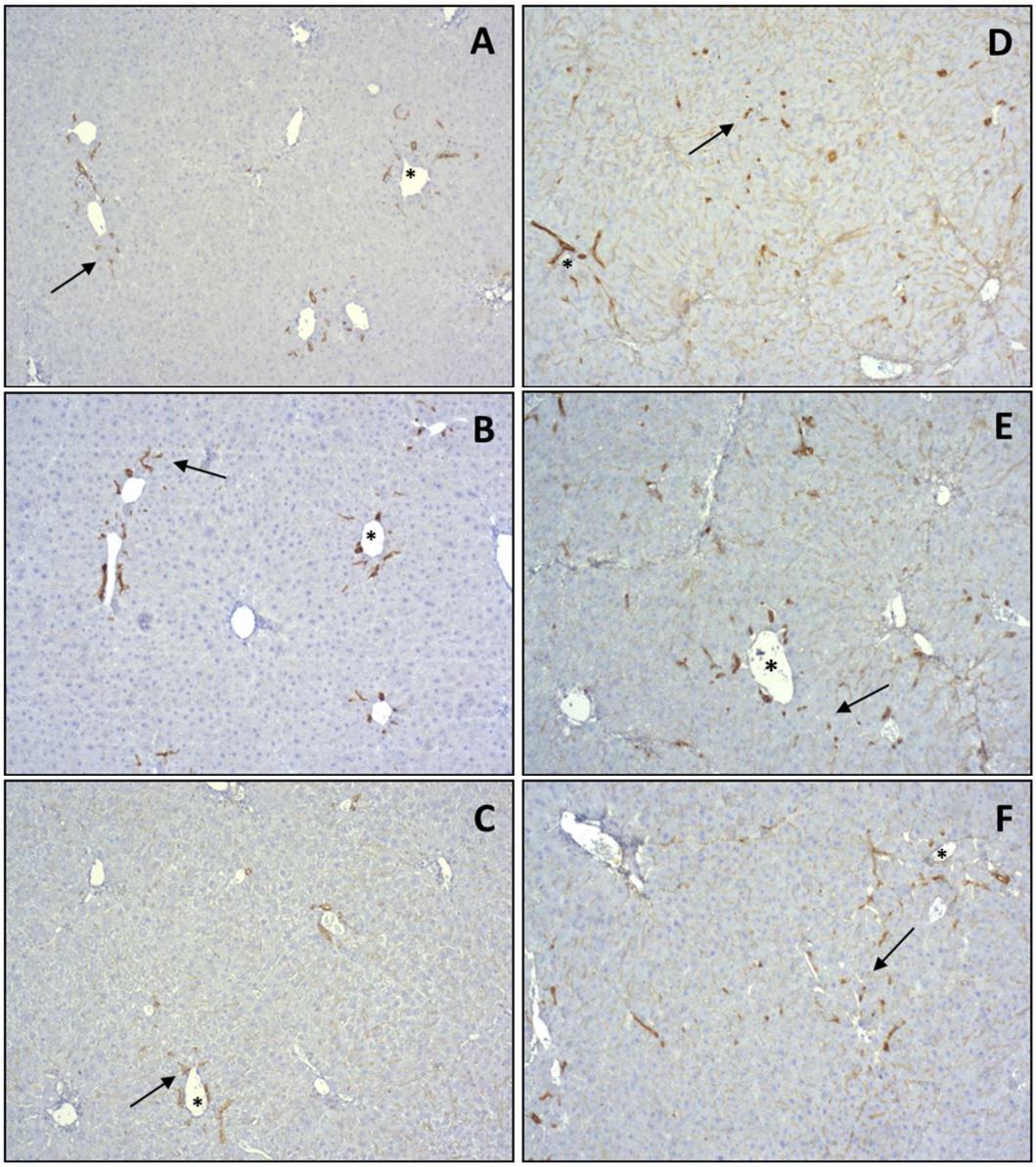

Fig. 50: Increased DR after a two (A-C) and eight weeks (D-F) CCl_4 treatment. Representative K1C19 stainings of Postn$^{-/-}$ (A, D), control (B, E) and Tnc$^{-/-}$ mice (C, F).

Postn$^{-/-}$ mice showed after two weeks a higher and after eight weeks a lower amount of new bile ducts compared to control mice. Tnc$^{-/-}$ mice showed after two and after eight weeks a lower DR as control mice. A-F: 10x.

The mRNA level of *K1c19* continuously increased in control mice after the CCl_4 treatment. In Postn$^{-/-}$ mice, *K1c19* expression was increased to a maximum after two weeks. Afterwards it continuously decreased. The mRNA of *K1c19* in Tnc$^{-/-}$ mice was constantly increased after two and four weeks and slightly decreased after eight weeks. Finally, there was no significant difference observed among the three genotypes at any point of time (Fig. 51).

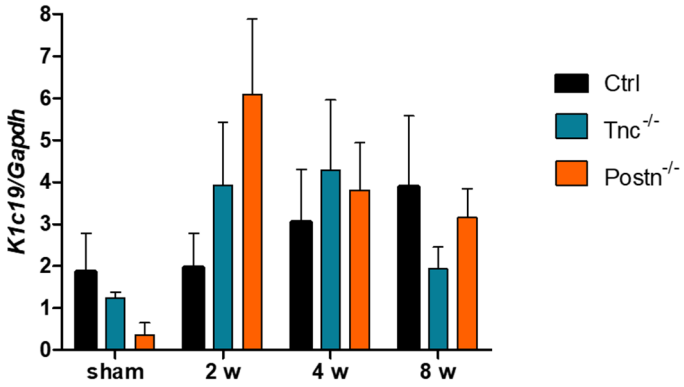

Fig. 51: Increased mRNA level of *K1c19* after CCl_4 treatment. In control mice, the *K1c19* mRNA level increased continuously, whereas in Postn$^{-/-}$ mice, the expression decreased with progressive liver damage. In Tnc$^{-/-}$ mice, the *K1c19* mRNA level was constant increased after two and four weeks and subsequently decreased. Relative quantification of gene expression was calculated with ΔΔCT-method to *Gapdh*. Data are expressed as means ± SEM (n=3-6), Kruskal-Wallis test.

2.1.3.5. HPC analysis

The progenitor marker SOX9 was not expressed in hepatocytes. In this toxic model, its expression was limited to biliary cells. Therefore, the immunohistological stainings were not further analyzed.

The mRNA level of *Sox9* in control mice was only increased after eight weeks. In Postn$^{-/-}$ mice, the *Sox9* expression was constantly slightly increased after the CCl_4 treatment. Tnc$^{-/-}$ mice showed only a minimal increased *Sox9* mRNA level after eight weeks of CCl_4 (Fig. 52).

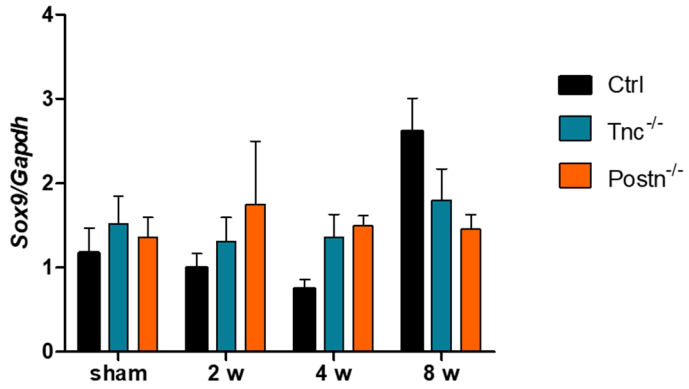

Fig. 52: mRNA level of *Sox9* after CCl_4 treatment. Control and $Tnc^{-/-}$ mice showed only after eight weeks an increased *Sox9* expression. $Postn^{-/-}$ mice showed a slightly constant increase of *Sox9* mRNA level. Relative quantification of gene expression was calculated with ΔΔCT-method to *Gapdh* and normalized to Ctrl sham mice. Data are expressed as means ± SEM (n=3-6), Kruskal-Wallis test.

2.1.3.6. Analysis of the HPI

The MKI67 expression shows that the proliferation of the hepatocytes is a diffuse process in response to a toxic liver injury. MKI67 was diffusely expressed in hepatocytes of any genotype at any point of time. An HPI between 2.26% and 2.4% was considered as normal. Control mice showed a constant increased proliferation rate after two and four weeks. After an eight-weeks-treatment, the HPI further increased until a mean score of 16% (Fig. 53; Fig. 54 B, E).

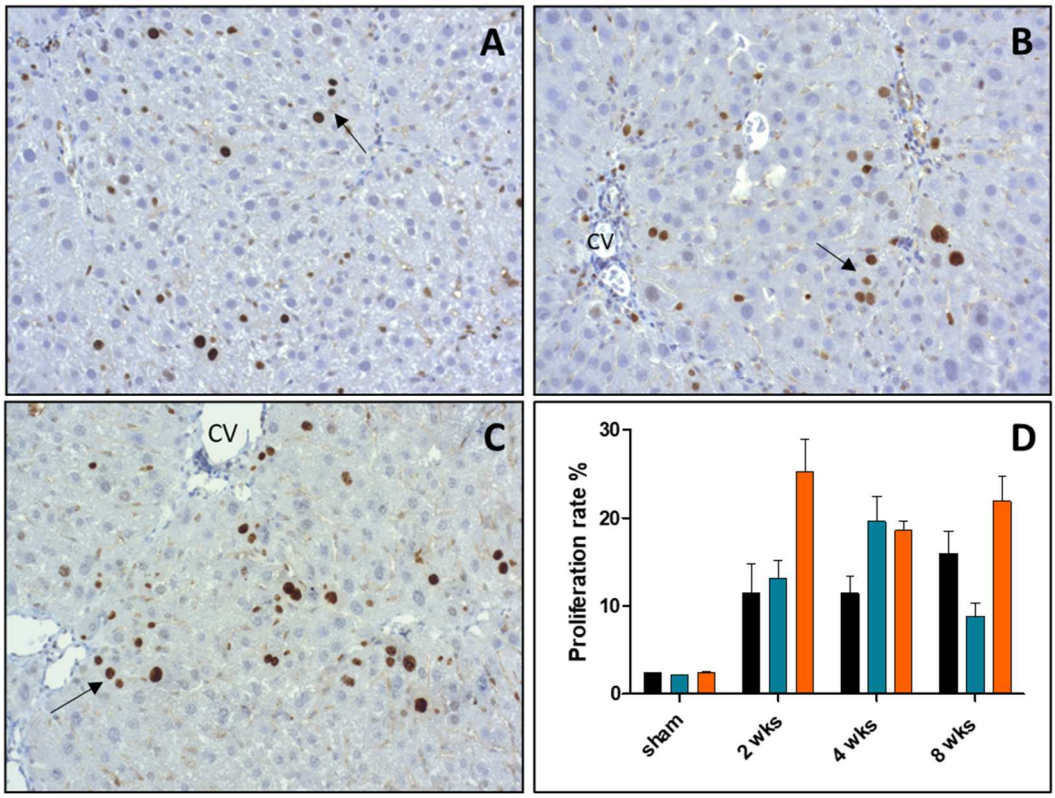

Fig. 53: Increased hepatocellular proliferation rate after the CCl_4 treatment. Representative MKI67 stainings of control mice after 2 (A), 4 (B) and 8 weeks (C). D: Quantification of the HPI by MKI67 expression in hepatocytes (arrows). Black bars: Ctrl, blue bars: $Tnc^{-/-}$, orange bars: $Postn^{-/-}$. Data are expressed as means ± SEM (n=3-6), Kruskal-Wallis test. A-C: 20x

$Postn^{-/-}$ mice always showed a higher HPI than control mice with an average maximum of 25.24% after two weeks. Afterwards, the HPI was slightly decreased after four weeks and increased again after eight weeks to an HPI of 21.93% (Fig. 53 D; Fig. 54 A, D). $Tnc^{-/-}$ mice showed a continuously increased HPI and a peak after four weeks with an average maximum of 19.64%. Subsequently, the proliferation rate was decreased to an HPI of 8.8% after eight weeks (Fig. 53 D; Fig. 54 C, F).

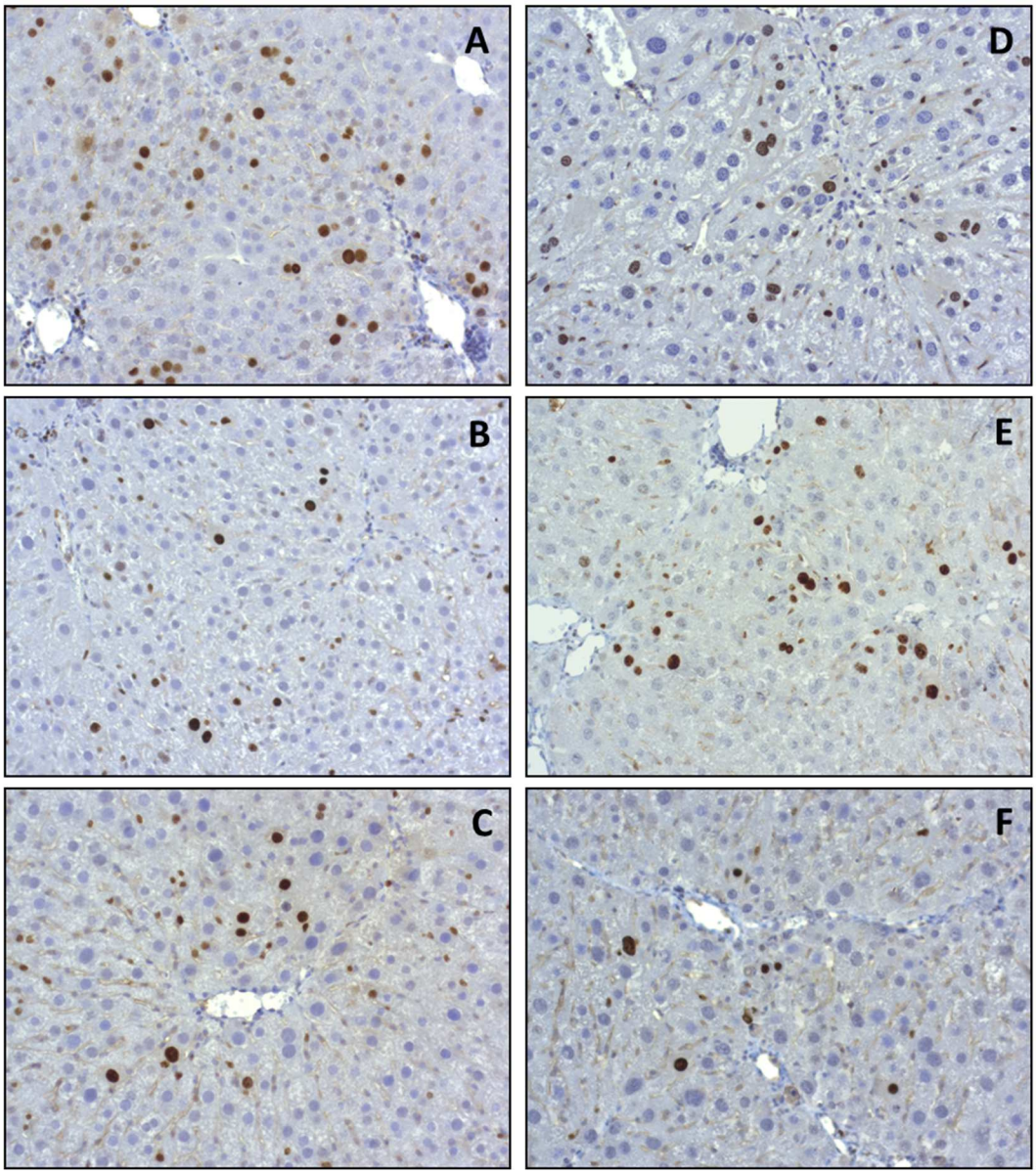

Fig. 54: HPI after a two (A-C) and eight (D-F) weeks CCl_4 treatment. Representative MKI67 stainings of $Postn^{-/-}$ (A, D), control (B, E) and $Tnc^{-/-}$ mice (C, F). $Postn^{-/-}$ mice showed always a higher HPI compared to control mice. $Tnc^{-/-}$ mice showed after two weeks a higher and after eight weeks a lower HPI as control mice. A-F: 20x.

In summary, POSTN and TNC are not expressed in the healthy liver but their expression increased with toxic liver damage. The amount of aHSC and the DR increased as well with liver damage and fibrosis. Furthermore, the surgery induced a diffuse proliferation of mature hepatocytes, whereas the expression of the progenitor marker Sox9 was limited to biliary cells. Although there are trends between the three genotypes in the respective stainings, the differences do not achieve statistical significance.

2.2. Results of the CCl_4 "Regeneration" model

The mice were treated for 12 weeks with CCl_4. Afterwards they could recover and were sacrificed 7, 14 or 21 days after the last injection.

2.2.1. Necroscopies

All sham mice showed no abnormalities of the general condition, of the peritoneal cavity as well as a normal liver and gallbladder. After twelve weeks of CCl_4 treatment, the mice often showed a spherical abdomen with an inconspicuous condition. Seven days after the last CCl_4 injection, the mice showed strong abdominal adhesions of the liver with the intestine and the diaphragm. The necroscopies 14 and 21 days after the last CCl_4 injection demonstrated, that the adhesions in general did not decrease. Regardless of the point of time, all mice showed moderate to strong adhesions which complicated to remove the liver without any further damaging. Both knockout mice showed in general weaker adhesions (Fig. 55).

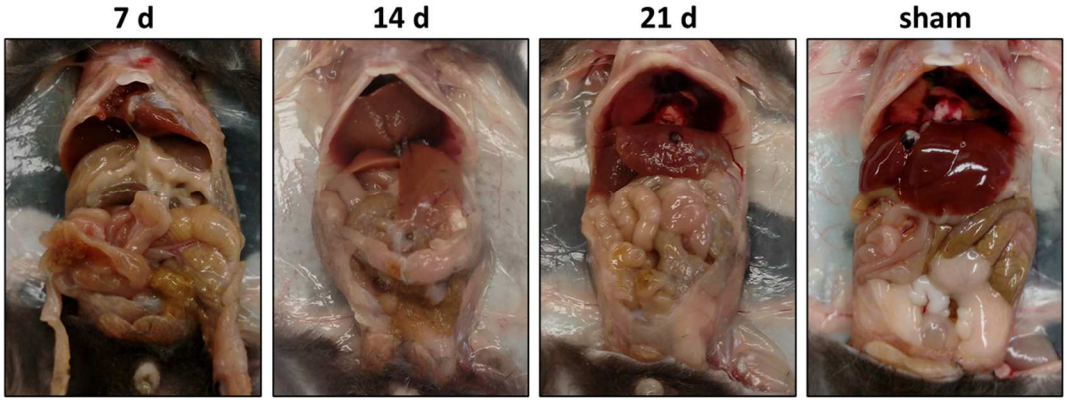

Fig. 55: The abdominal cavity with the liver of control mice during the regenerative phase after the CCl_4 treatment. Treated mice showed moderate to strong adhesions at any time.

The analysis of the LBW-r. % identified a mild increase after the CCl_4 treatment among the three genotypes. The adhesions made the removal of the liver difficult, which led to a possible falsification of the results. Therefore, possible differences were not considered (Fig. 56).

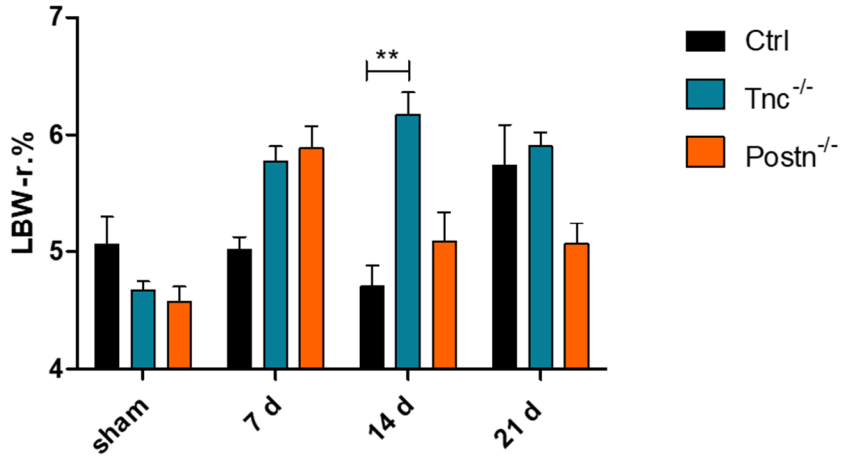

Fig. 56: LBW-r. % during liver regeneration. The LBW-r. % was increased during the regenerative phase. Data are expressed as means ± SEM (n=4-6), Kruskal-Wallis test, * *P*< 0.05, ** *P*< 0.001.

2.2.2. Results of the histological stainings

For the characterization of the liver tissue during the regenerative phase after a toxic injury, different histological stainings were evaluated.

2.2.2.1. Inflammation analysis

Seven days after the last CCl_4 injection, control mice still showed a moderate inflammatory activity. Multiple necroses around the CV with occasional bridges of necrotic hepatocytes were detectable. During the regenerative phase, the necroses were removed and the liver parenchyma regenerated. After 21 days only a mild inflammation was observed and the mean mHAI Score was 3.75 (Fig. 57; Fig. 58 B).

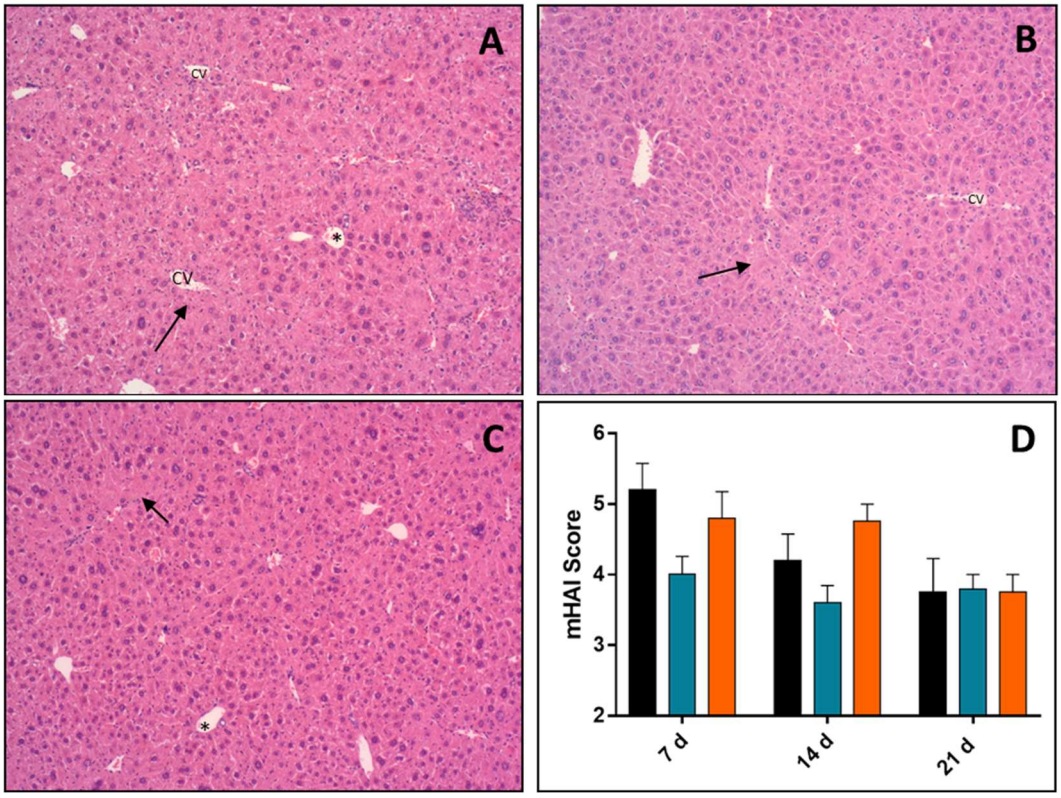

Fig. 57: Decreasing inflammatory activity during the regenerative phase after the CCl_4 treatment. Representative HE stainings of control mice 7 (A), 14 (B) and 21 days (C) after the last CCl_4 injection. With progressive regeneration, the number of necrotic hepatocytes (arrows), predominantly located around central veins (CV), decreased. There was no inflammation in the portal tract (asterisk) observed. D: Grading by using the mHAI Score. Black bars: Ctrl, blue bars: $Tnc^{-/-}$, orange bars: $Postn^{-/-}$. Data are expressed as means ± SEM (n=4-6), Kruskal-Wallis test. A-C: 10x.

The $Postn^{-/-}$mice showed a prolonged inflammatory reactivity until day 14. After 21 days, the mHAI of $Postn^{-/-}$ mice decreased to 3.75 and they only showed a mild inflammation like control mice (Fig. 57 D; Fig. 58 A). The $Tnc^{-/-}$ showed a quite constant mild inflammatory reactivity. After 21 days, the inflammatory activity was similar to control mice and the mean mHAI Score was 3.8 (Fig. 57 D; Fig. 58 C).

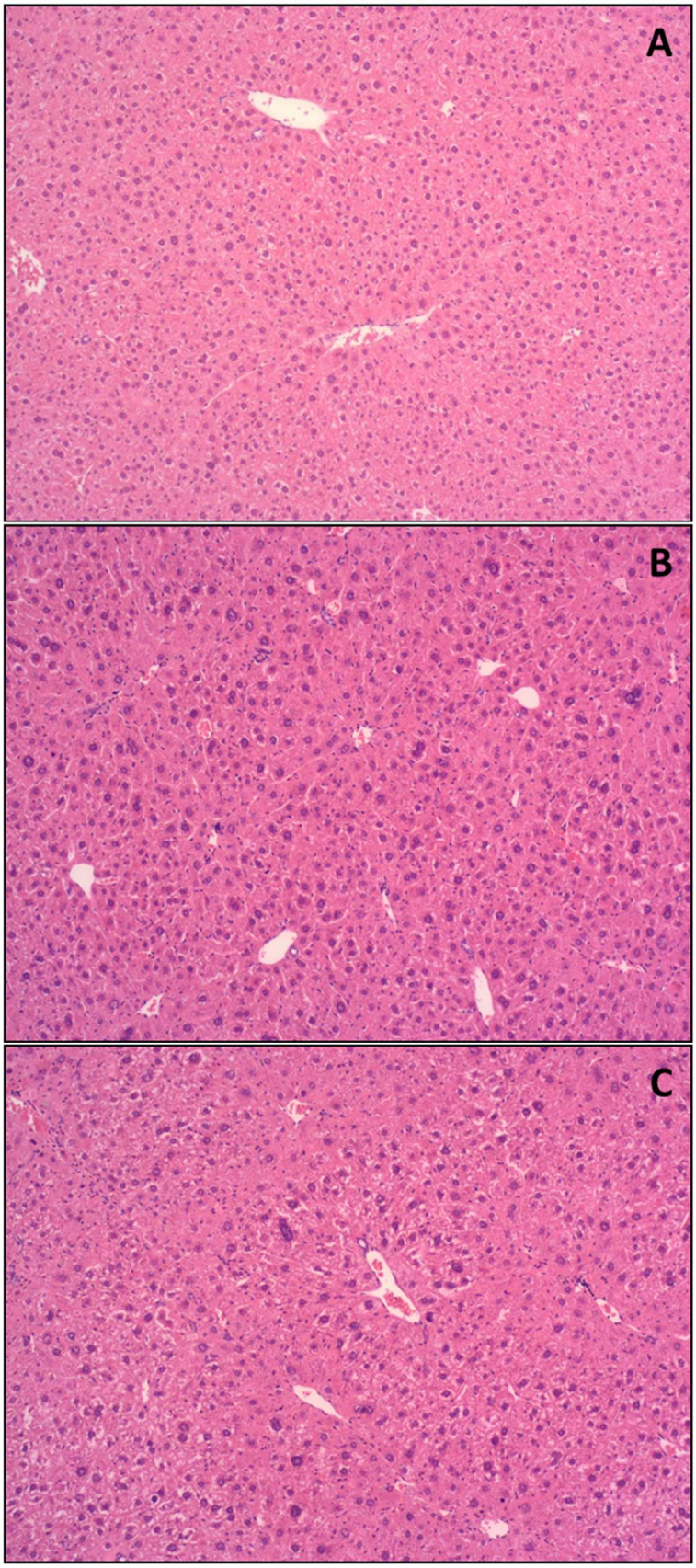

Fig. 58: Mild inflammatory activity 21 days after the last CCl_4 injection. Representative HE stainings of $Postn^{-/-}$ (A), control (B) and $Tnc^{-/-}$ mice (C). All mice showed only a mild

inflammation in the liver tissue. A-C: 10x.

2.2.2.2. Analysis of fibrosis stage

The collagen degradation in the regenerative phase was determined by using the PSR staining. In the liver of control mice, a continuous degradation of the ECM was observed. Seven days after the last CCl_4 injection, they occasionally showed complete nodules as well as complete and incomplete thick septa. With progressive degradation of the ECM, the fibrous septa got thinner and occasionally interrupted. After 21 days, thin and incomplete septa as well as isolated remaining collagen fibers were left in the parenchyma. Finally, the mean mIS decreased from 7.0 to 6.25 (Fig. 59; Fig. 60 B).

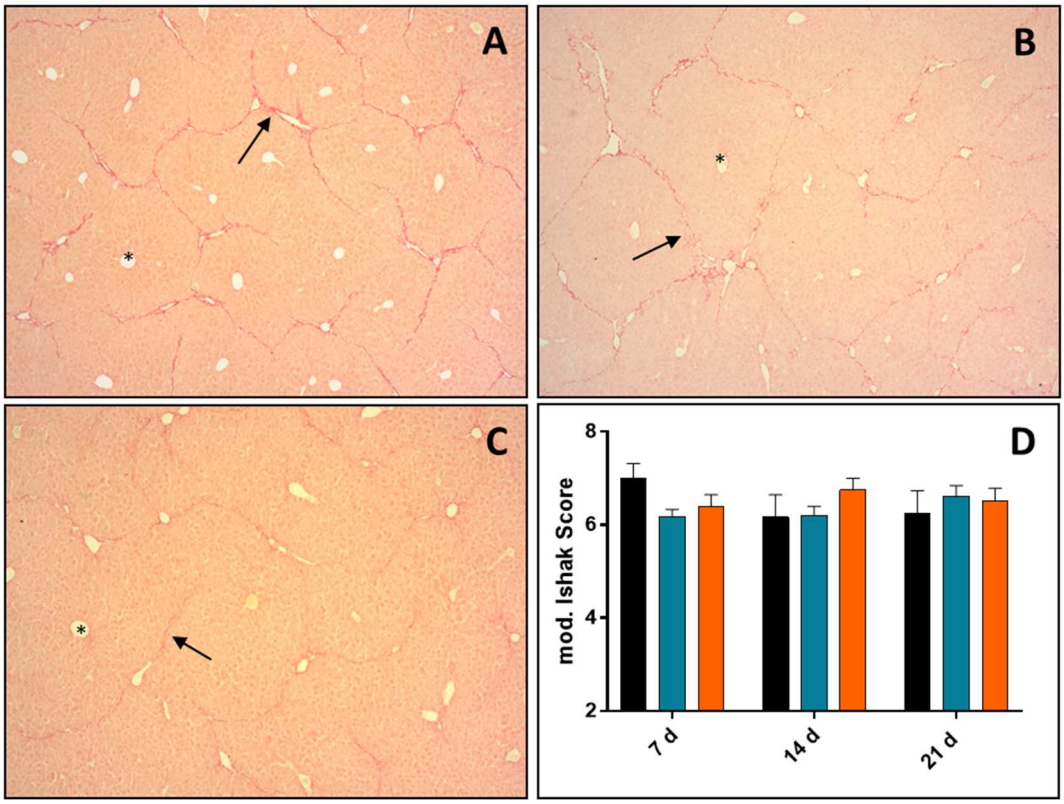

Fig. 59: Degradation of Collagen I and III during liver regeneration after the CCl_4 treatment. Representative PSR stainings of control mice after 7 (A), 14 (B) and 21 days (C) after the last CCl_4 injection. Continuous collagen degradation (arrows) around central veins (CV). Normal collagen expression in portal tracts (asterisks). D: Staging according to the mIS. Black bars: Ctrl, blue bars: $Tnc^{-/-}$, orange bars: $Postn^{-/-}$. Data are expressed as means ± SEM (n=4-6), Kruskal-Wallis test. A-C: 5x.

$Postn^{-/-}$ and $Tnc^{-/-}$ mice showed a lower collagen degradation with a more constant amount of collagen fibers during the regenerative phase. $Postn^{-/-}$ mice showed multiple complete septa after seven days. After 14 days, complete and partial thick

septa were still present. The amount of collagen decreased slightly, but $Postn^{-/-}$ mice presented remaining complete septa and a mean mIS of 6.75 after 21 days (Fig. 59 D; Fig. 60 A). $Tnc^{-/-}$ mice showed complete nodules seven days after the last CCl_4 injection. With progressive regeneration, the septa got thinner and occasionally interrupted after 14 days. After 21 days, $Tnc^{-/-}$ mice still showed complete septa and a higher amount of collagen fibers compared to control mice with a mean mIS of 6.6 (Fig. 59 D; Fig. 60 C).

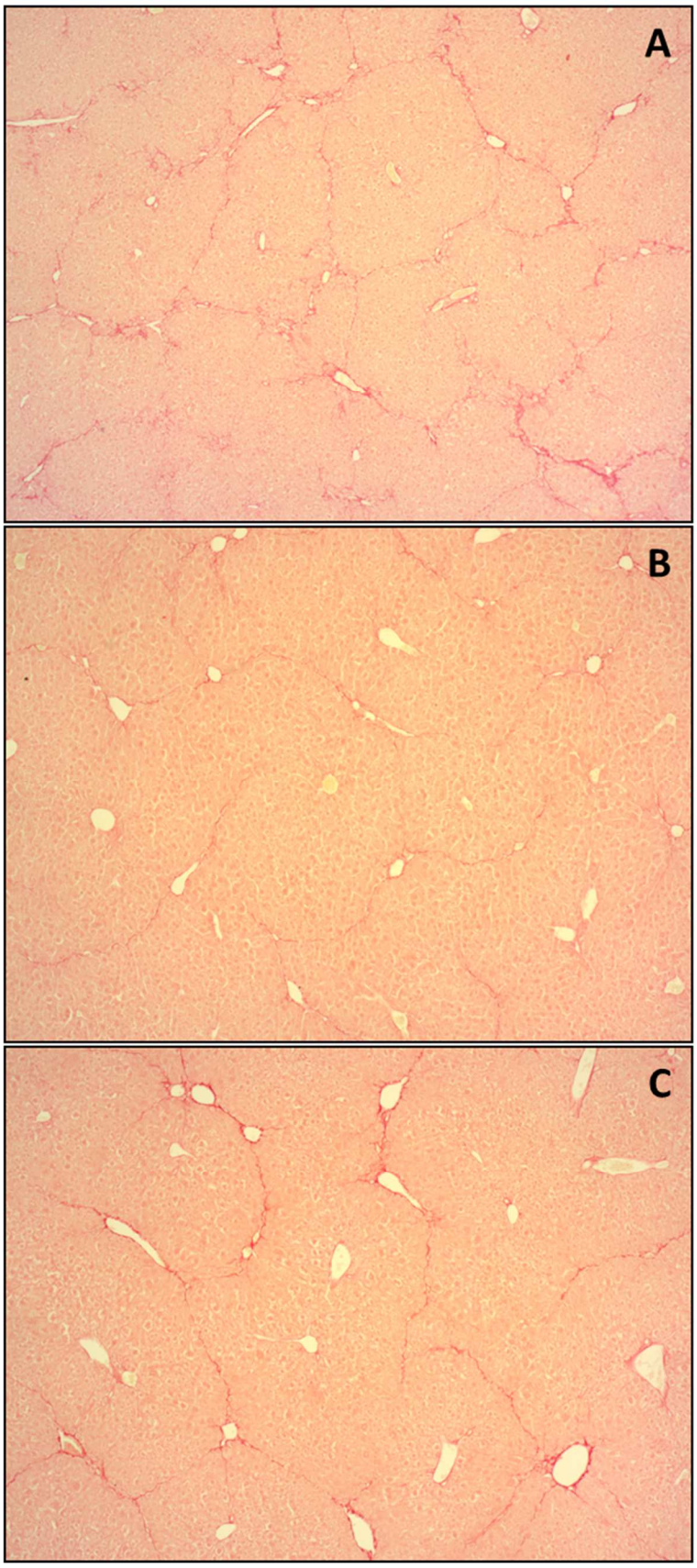

Fig. 60: Deposition of Collagen I and III 21 days after the last CCl_4 injection. Representative PSR stainings of $Postn^{-/-}$ (A), control (B) and $Tnc^{-/-}$ mice (C). Both knockout mice showed a higher amount of collagen. A-C: 5x.

In conclusion, Postn$^{-/-}$ mice showed a prolonged and Tnc$^{-/-}$ mice a reduced inflammatory reactivity. Furthermore, both knockouts showed a reduced collagen degradation compared to control mice. In the end, there was no significant difference among the three genotypes.

2.2.3. Results of the immunohistochemistry

Different markers for the immunohistochemistry were used for a more detailed characterization of the liver tissue during regeneration after a toxin-mediated fibrosis.

2.2.3.1. Periostin

Seven days after the last CCl_4 injection, control mice only showed a weak expression of POSTN in or around the wall of less than 25% of the CV. With ongoing regeneration, the POSTN expression further decreased. After 21 days, POSTN was only occasionally weakly expressed close to inflammatory cells in the wall of occasional CV and the mean POSTN Score decreased to 0.4 after 21 days of regeneration (Fig. 61; Fig. 62 A-C).

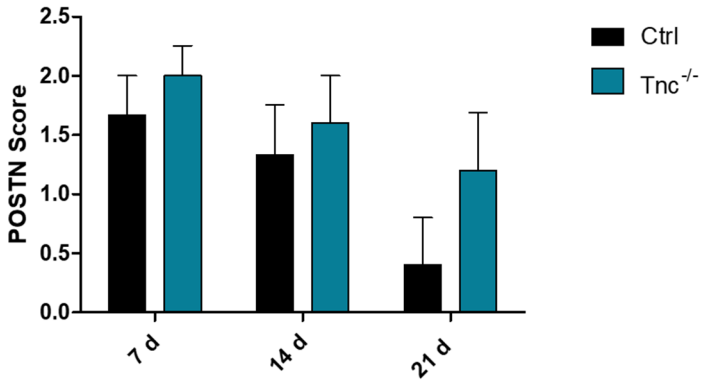

Fig. 61: Decreasing POSTN expression in control and Tnc$^{-/-}$ mice during liver regeneration. POSTN expression continuously decreased after the last CCl_4 injection. Tnc$^{-/-}$ mice showed a delayed reduction of POSTN compared to control mice. Data are expressed as means ± SEM (n=4-6), Kruskal-Wallis test.

Tnc$^{-/-}$ mice showed a slightly higher POSTN expression than control mice during the regenerative phase. The POSTN expression decreased more slowly and the mean POSTN Score decreased to 1.2 after 21 days (Fig. 61; Fig. 62 D-F).

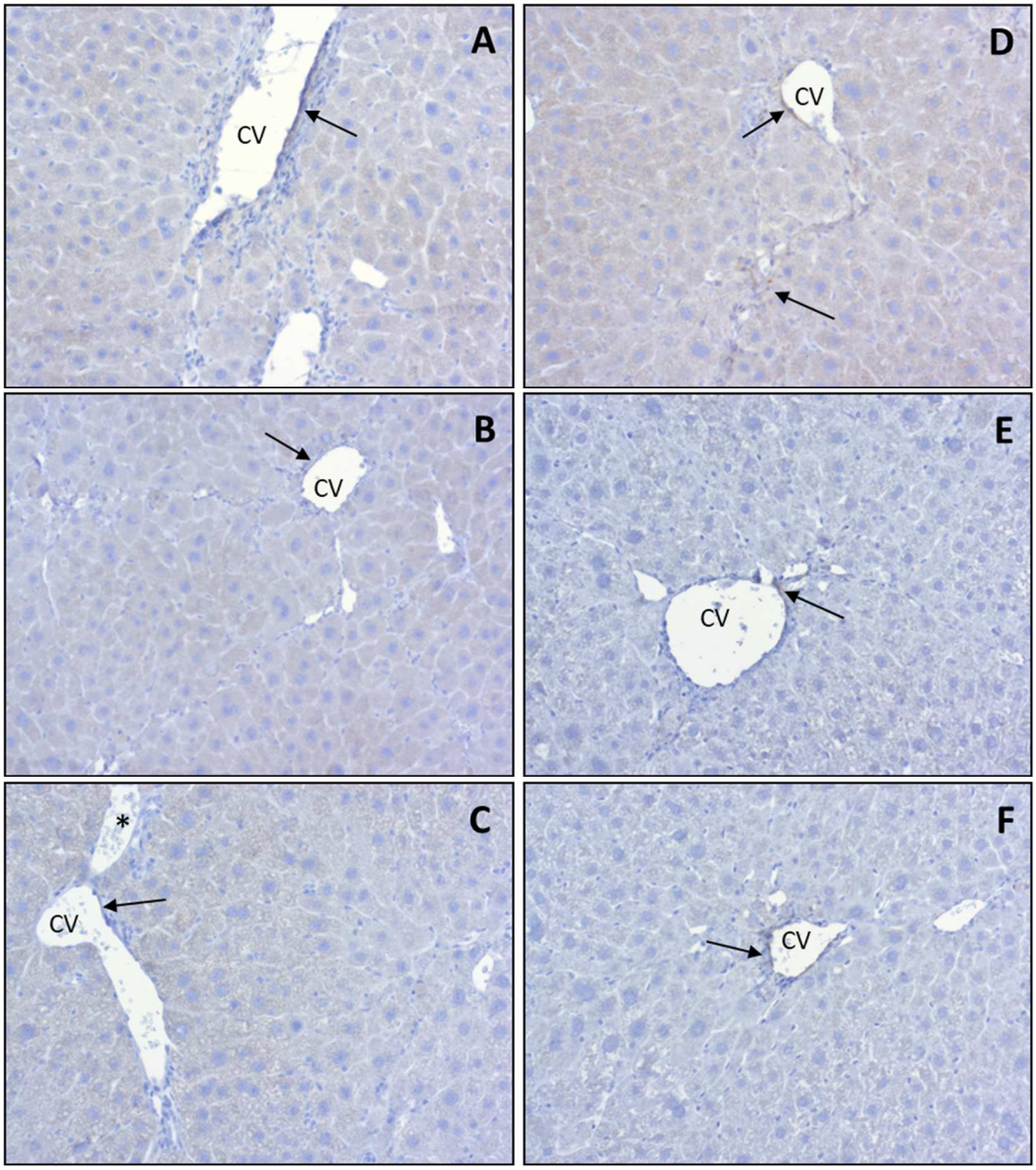

Fig. 62: Decreasing POSTN expression in control (A-C) and Tnc$^{-/-}$ mice (D-F) during liver regeneration. Representative POSTN stainings after 7 (A, D), 14 (B, E) and 21 days (C, F). POSTN (arrows) was only expressed in or around the wall of CV. Tnc$^{-/-}$ mice showed a prolonged expression of POSTN compared to control mice. A-F: 20x.

2.2.3.2. Tenascin C

Seven days after the last CCl_4 injection, control mice only showed a weak expression of TNC around CV and along fibrotic septa in more than 50% of the tissue. With ongoing regeneration, the TNC expression decreased, and less CV and septa were positively stained after 14 days. After 21 days, TNC was only occasionally weakly expressed around CV and the mean TNC Score decreased to 1.2 (Fig. 63; Fig. 64 A-C).

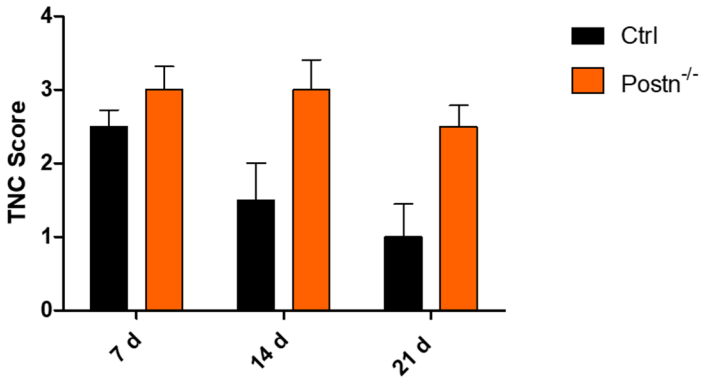

Fig. 63: Decreasing TNC expression in control and Postn$^{-/-}$ mice during liver regeneration. TNC expression continuously decreased after the last CCl_4 injection in control mice. Postn$^{-/-}$ mice showed a delayed reduction of TNC compared to control mice. Data are expressed as means ± SEM (n=4-6), Kruskal-Wallis test.

Postn$^{-/-}$ mice showed a slightly higher and prolonged TNC expression. Seven days after the last CCl_4 injection, TNC was still expressed more diffusely in the parenchyma. After 14 days, Postn$^{-/-}$ mice showed more positive cells around CV and along fibrotic septa. In the end, there were remaining positive CV and fibrotic septa and the mean TNC Score decreased to 2.5 (Fig. 63; Fig. 64 D-F).

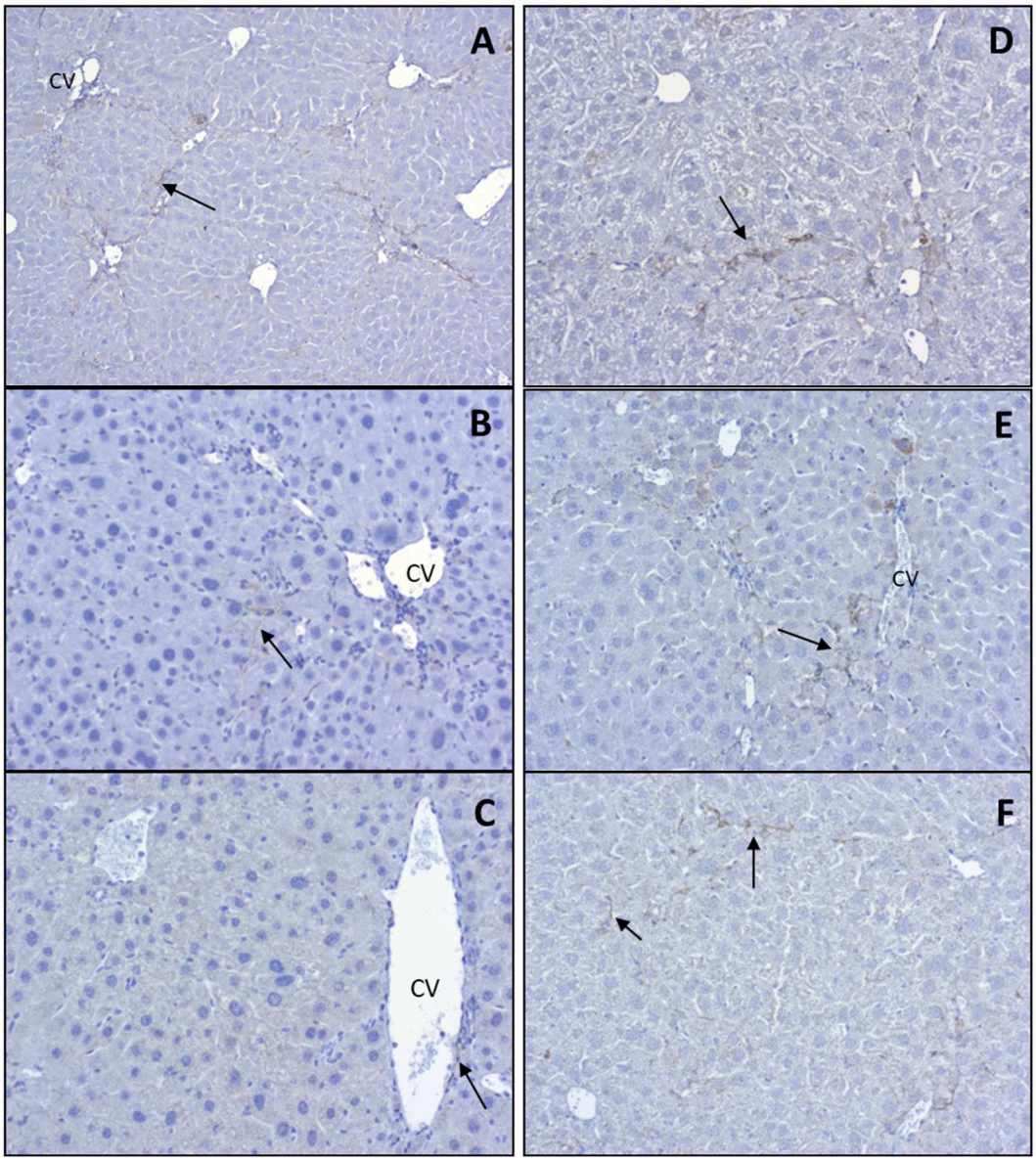

Fig. 64: Decreasing TNC expression in control (A-C) and Postn$^{-/-}$ mice (D-F) during liver regeneration. Representative TNC stainings after 7 (A, D), 14 (B, E) and 21 days (C, F). TNC (arrows) was expressed in or around the wall of CV and along fibrotic septa. Postn$^{-/-}$ mice showed a prolonged expression of TNC compared to control mice. A-F: 20x.

2.2.3.3. Analysis of aMF

The localization and amount of aMF during the regenerative phase was determined by using ACTA2. The pattern of the ACTA2 expression is like the pattern of the CCl_4 "Fibrosis" group. Seven days after the last CCl_4 injection, control mice showed a generally weak expression of ACTA2. It was mainly around CV, along fibrotic septa and occasional diffuse in the parenchyma. After 14 days, the amount of aMF decreased and the pattern was more diffuse without marked septa. With advanced regeneration, the number of aMF further decreased. After 21 days, only a few positive spots around the CV were left and the mean

histopathological Score decreased from 16.6 to 11.6 (Fig. 65, Fig. 66 B).

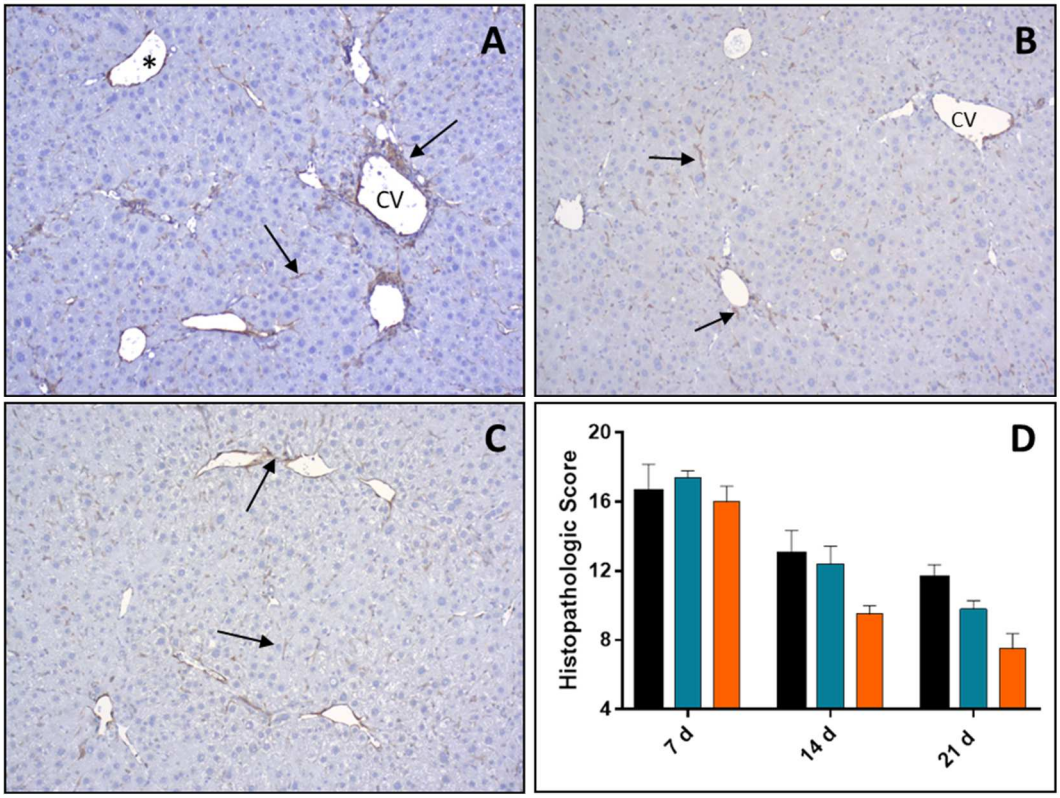

Fig. 65: Decreasing amount of aMF during liver regeneration after the CCl_4 treatment. Representative ACTA2 stainings of control mice after 7 (A), 14 (B) and 21 days (C). Activated MF (arrows) were located around CV and occasional diffuse in the parenchyma. The amount of aMF continuously decreased with proceeding regeneration. D: Quantification of aMF based on the histopathologic Score. Both knockout mice showed a faster depletion of aMF. Black bars: Ctrl, blue bars: $Tnc^{-/-}$, orange bars: $Postn^{-/-}$. Data are expressed as means ± SEM (n=4-6), Kruskal-Wallis test. A-C: 10x

In $Postn^{-/-}$ mice, the ACTA2 expression decreased faster than in control mice. After 14 and 21 days, they showed a lower expression. In the end, only a few positive spots were left (Fig. 66 A). $Tnc^{-/-}$ mice showed a similar trend in the ACTA2 expression as control mice. Seven days after the last CCl_4 injection the showed a slightly higher amount of ACTA2 positive cells, whereas it was lower after 14 and 21 days. Finally, they also had a few diffuse spots of aMF left (Fig. 66 C). The mean histopathological Score decreased from 16 to 7.5 in $Postn^{-/-}$ mice and from 17.4 to 9.8 in $Tnc^{-/-}$ mice (Fig. 65 D).

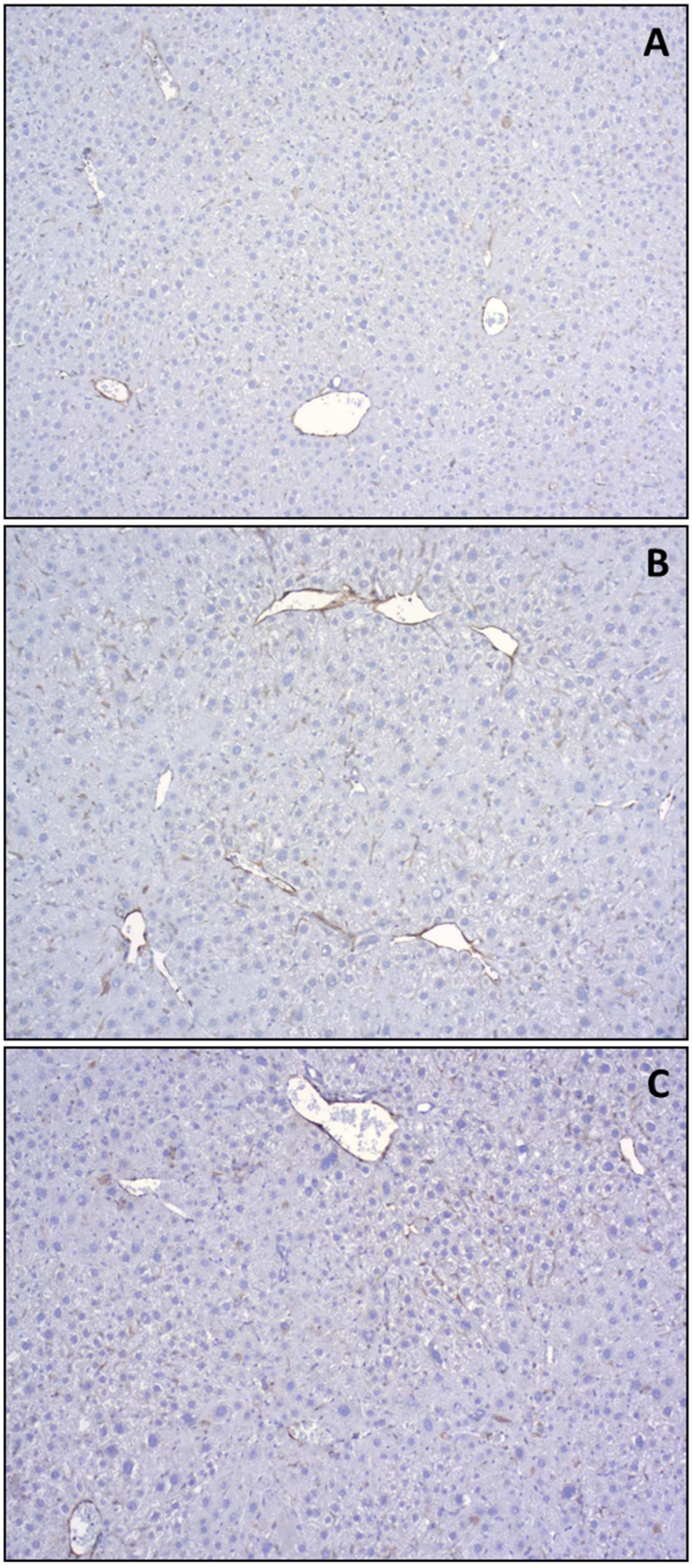

Fig. 66: Amount and localization of aMF 21 days after the last CCl_4 injection. Representative ACTA2 stainings of $Postn^{-/-}$ (A), control (B) and $Tnc^{-/-}$ mice (C). Both

knockout mice showed less aMF. A-C: 10x.

2.2.3.4. Analysis of the DR

The analysis of the K1C19 expression during the regenerative phase shows that the pattern of the DR is the same as in the "Fibrosis" group. New bile ducts are diffuse in the parenchyma of the liver and cannot allocate to a certain portal tract. Seven days after the last CCl_4 injection, control mice showed an increased number of bile ducts. During the regenerative phase, the amount of DR decreased continuously from mean 141.17 to 115.8 (Fig. 67; Fig. 68 B).

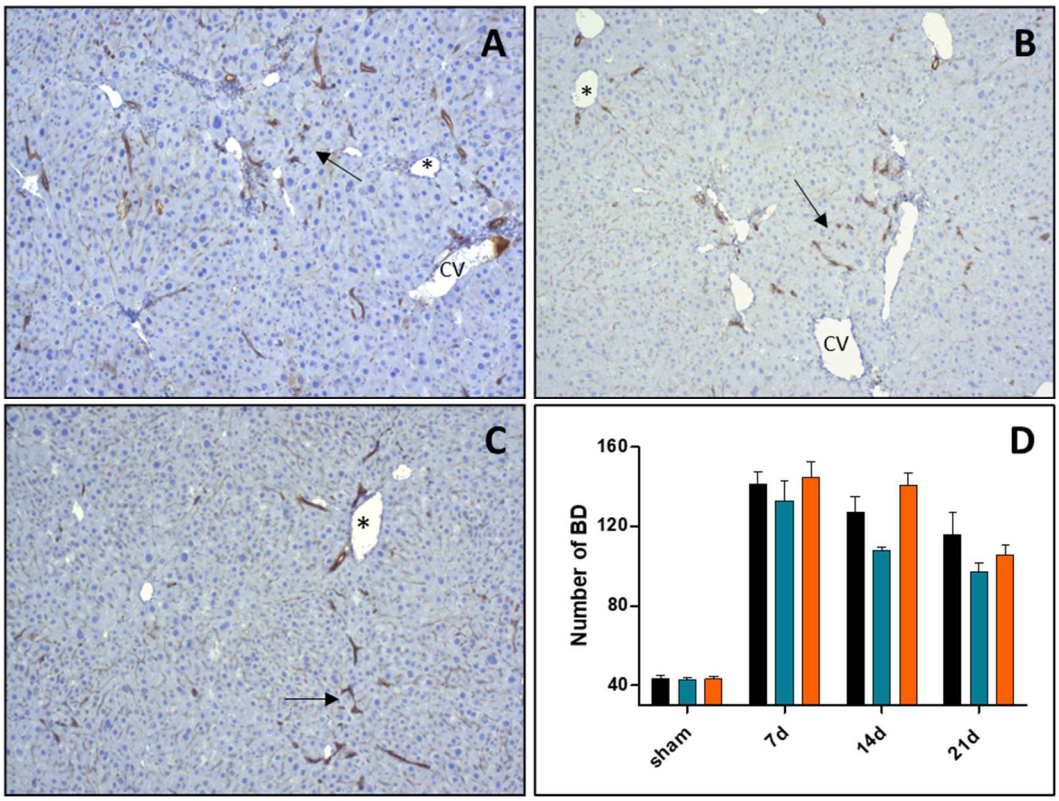

Fig. 67: Decreasing DR during liver regeneration after the CCl_4 treatment. Representative K1C19 stainings of control mice after 7 (A), 14 (B) and 21 days (C) of regeneration. BD (arrows) were diffuse in the parenchyma between CV and portal tracts (asterisks). D: Quantification of the DR by evaluating the number of BD. In control and $Tnc^{-/-}$ mice, the number of BD continuously decreased. $Postn^{-/-}$ showed an impaired decrease of BD. Black bars: Ctrl, blue bras: $Tnc^{-/-}$, orange bars: $Postn^{-/-}$. Data are expressed as means ± SEM (n=4-6), Kruskal-Wallis test.

$Postn^{-/-}$ mice showed about the same number of bile ducts as control mice 7 days after the last CCl_4 injection. In contrast to them, $Postn^{-/-}$ mice showed a constant increased amount of bile ducts after 14 days. Afterwards, the DR also decreased from 144.6 to an average score of 105.75 on day 21 (Fig. 67 D; Fig. 68 A). $Tnc^{-/-}$

mice showed the same course of the DR as control mice. The number of bile ducts decreased continuously. Compared to control mice, they showed a lower amount of DR at any point of time. In the end, the average score decreased from 133 to 97.2 (Fig. 67 D; Fig. 68 C).

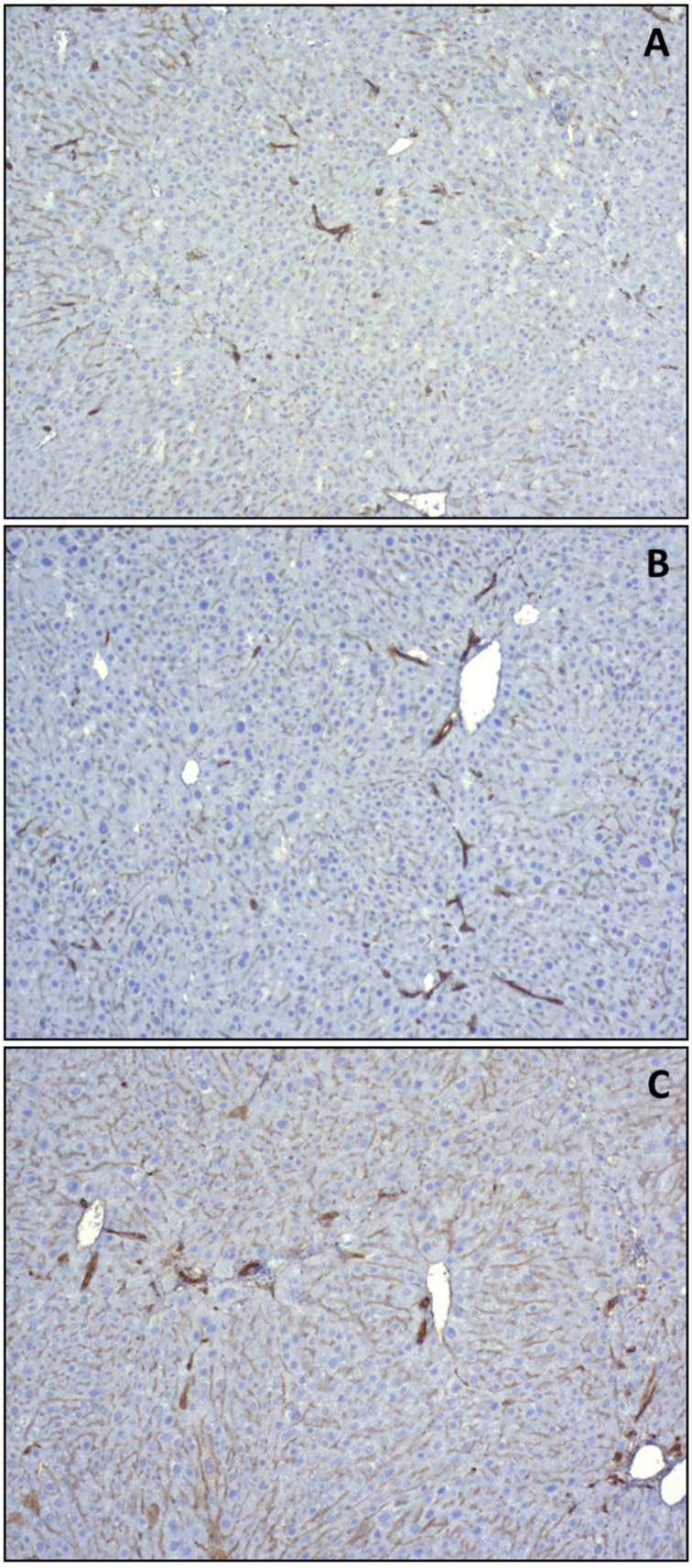

Fig. 68: Ductular reaction 21 days after the last CCl_4 injection. Representative K1C19 stainings of $Postn^{-/-}$ (A), control (B) and $Tnc^{-/-}$ mice (C). Both knockout mice showed a lower

amount of DR. A-C: 10x.

2.2.3.5. HPC analysis

The progenitor marker SOX9 was not expressed in hepatocytes. In this regeneration model, its expression was limited to biliary cells and therefore not further analyzed.

2.2.3.6. Analysis of the HPI

During the regenerative phase after a toxic liver damage, MKI67^{+} hepatocytes can -as well- be found diffusely in the parenchyma. Control mice showed a continuously decreasing HPI. Seven days after the last CCl_4 injection, they showed an average HPI of 11.27% which decreased to 6.2% after 21 days (Fig. 69; Fig. 70 B, E).

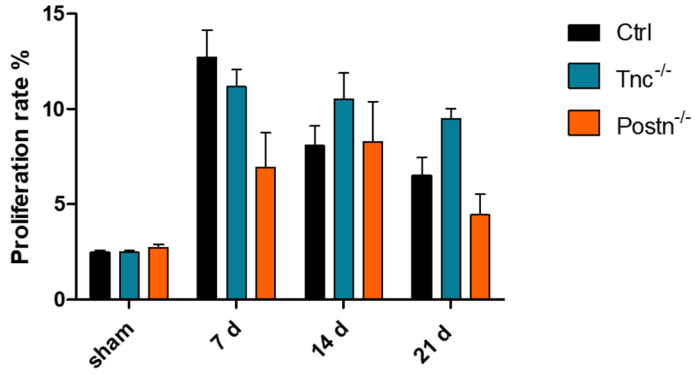

Fig. 69: Hepatocellular proliferation rate during liver regeneration after the CCl_4 treatment. The HPI decreased in control mice continuously. Tnc$^{-/-}$ mice showed a prolonged HPI, which was just slightly decreasing with progressive regeneration. In Postn$^{-/-}$ mice, the HPI slightly increased until day 14 and subsequently decreased. Data are expressed as means ± SEM (n=4-6), Kruskal-Wallis test.

Postn$^{-/-}$ and Tnc$^{-/-}$ mice showed a more constant HPI in the regenerative phase. The HPI in Postn$^{-/-}$ mice was always predominantly lower than in control mice (Fig. 70 A, D). In contrast to that, Tnc$^{-/-}$ mice showed a higher HPI after 14 and 21 days (Fig. 70 C, F). The HPI decreased to 4.45% in Postn$^{-/-}$ mice and to 9.48% in Tnc$^{-/-}$ mice on day 21 (Fig. 69).

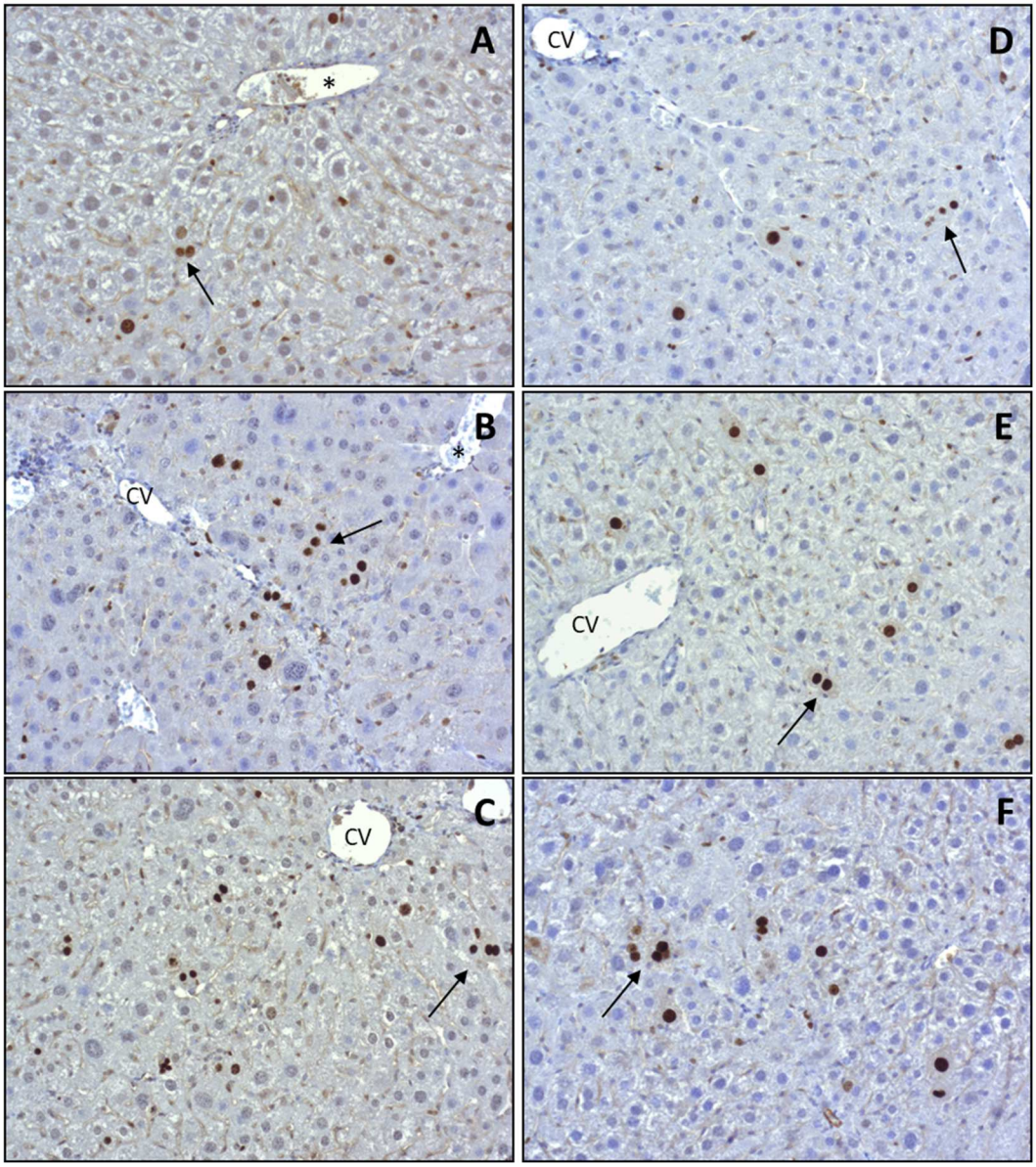

Fig. 70: Hepatocellular proliferation 7 (A-C) and 21 days (D-F) after the last CCl_4 injection. Representative MKI67 stainings of $Postn^{-/-}$ (A, D), control (B, E) and $Tnc^{-/-}$ mice (C, F). Proliferating hepatocytes (arrows) were diffusely distributed in the parenchyma between portal tracts (asterisk) and CV. $Postn^{-/-}$ mice showed always a lower HPI as control mice. $Tnc^{-/-}$ mice showed a lower HPI after 7 days and a higher after 21 days compared to control mice. A-F: 20x.

In summary, the immunohistochemistry reveals that the expression of POSTN and TNC as well as the amount of aHSC decreased and is almost no longer present during liver regeneration. $Postn^{-/-}$ mice showed a prolonged DR, whereas it decreased in $Tnc^{-/-}$ and control mice. The number of proliferating hepatocytes was increased in $Tnc^{-/-}$ mice. However, the differences between the genotypes do not achieve statistical significance.

3. Comparison of cholestatic versus toxic liver damage

The following tables illustrate the main differences of the histological analyses between Postn$^{-/-}$, Tnc$^{-/-}$ and control mice in consequence of the BDL and CCl_4 treatment.

In the BDL model, only Postn$^{-/-}$ mice showed a higher inflammatory activity, due to more necrotic hepatocytes, compared to control mice. Instead, in course of the CCl_4 treatment, Postn$^{-/-}$ as well as Tnc$^{-/-}$ mice showed a higher inflammatory activity. In general, the BDL leads to a greater inflammatory reaction than the CCl_4 treatment (Tab. 10).

Tab. 10: Inflammatory activity. Quantified by mHAI Score.

mHAI	BDL 21 d	CCl_4 "Fibrosis" 8 wks
Ctrl	7.83	5.33
Postn$^{-/-}$	9.50	5.67
Tnc$^{-/-}$	7.83	5.80

Furthermore, Postn$^{-/-}$ mice showed a weaker fibrotic reaction than Tnc$^{-/-}$ and control mice following BDL. In the CCl_4 model, both knockouts showed a reduced collagen deposition as well as a reduced degradation of collagen during the regenerative phase compared to control mice (Tab. 11).

Tab. 11: Fibrosis stage. Collagen deposition quantified by PSR staining. In the BDL model, the IS was used and in the CCl_4 the mIS was used.

IS	BDL 21 d
Ctrl	2.33
Postn$^{-/-}$	2.0
Tnc$^{-/-}$	2.17

mIS	CCl_4 "Fibrosis" 8 wks	CCl_4 "Regeneration" 21 d
Ctrl	7.17	5.0
Postn$^{-/-}$	6.17	6.5
Tnc$^{-/-}$	6.20	6.6

In both models, the collagen deposition correlates with the distribution pattern of ACTA2 positive aMF. Both knockouts showed less aMF during fibrogenesis and during the regenerative phase following CCl_4 treatment (Tab. 12).

Tab. 12: Histopathological Score. Quantified by intensity and distribution pattern of ACTA2 positive aMF.

HS	BDL 21 d	CCl_4 "Fibrosis" 8 wks	CCl_4 "Regeneration" 21 d
Ctrl	14.67	17.35	11.6
Postn$^{-/-}$	14.17	15.33	7.5
Tnc$^{-/-}$	14.0	16.0	9.8

The cholestatic BDL model induces a higher expression of POSTN than the toxic CCl_4 model. However, there was no difference among Tnc$^{-/-}$ and control mice in any fibrosis model (Tab. 13).

Tab. 13: Periostin expression. POSTN Score quantified by the intensity and distribution pattern.

POSTN Score	BDL 21 d	CCl_4 "Fibrosis" 8 wks
Ctrl	4.67	2.5
Tnc$^{-/-}$	4.60	2.75

Similarly, the TNC expression is higher in the cholestatic than in the toxic model. Furthermore, the Postn$^{-/-}$ mice showed a higher TNC expression at the beginning of the cholestatic and toxic damage (Tab. 14).

Tab. 14: Tenascin C expression. TNC Score quantified by intensity and distribution pattern.

TNC Score	BDL 3 d	BDL 21 d	CCl_4 "Fibrosis" 2 wks	CCl_4 "Fibrosis" 8 wks
Ctrl	3.17	5.5	1.2	4.5
Postn$^{-/-}$	4.75	5.67	2.2	4.67

In the BDL model, the DR was limited to the portal tract, whereas in the CCl_4 model, small new bile ducts where found distributed in the parenchyma. Following BDL, no differences in the number of bile ducts between the genotypes were observed. However, after eight weeks of CCl_4, both knockouts showed less DR than control mice (Tab. 15).

Tab. 15: Ductular reaction. Quantification of the DR by K1C19 staining.

BD/PT	BDL 21 d
Ctrl	4.55
Postn$^{-/-}$	4.47
Tnc$^{-/-}$	4.52

DR	CCl_4 "Fibrosis" 8 wks
Ctrl	153.16
Postn$^{-/-}$	111.14
Tnc$^{-/-}$	116.6

In consequence of the cholestatic damage, Postn$^{-/-}$ mice showed a lower H-Score than control mice at any time. Instead, Tnc$^{-/-}$ mice showed a higher H-Score at the beginning and a lower H-Score at the end, compared to control mice (Tab. 16).

Tab. 16: H-Score. Quantification of HPC after BDL by using the H-Score.

H-Score	3 d	7 d	21 d
Ctrl	79.67	76.42	69.25
Postn$^{-/-}$	68.4	57.25	52.93
Tnc$^{-/-}$	96.2	85.2	63.08

After the BDL, the HPI of Tnc$^{-/-}$ and control showed a peak on day seven, whereas it was almost constant increased in Postn$^{-/-}$ mice. In the CCl_4 “Fibrosis” model, the HPI of control mice increased until week eight. In Postn$^{-/-}$ mice, the HPI was quite stable whereas Tnc$^{-/-}$ mice showed a peak after four weeks. During the regenerative phase, the HPI of control mice continuously decreased. In both knockouts, the HPI decreased in general as well but with a peak on day 14 (Tab. 17).

Tab. 17: Hepatocellular proliferation index. Quantification of the HPI by MKI67 staining.

HPI	BDL			CCl_4 "Fibrosis"			CCl_4 "Regeneration"		
	3 d	7 d	21 d	2 wks	4 wks	8 wks	7 d	14 d	21 d
Ctrl	8.13	16.8	11.63	11.44	11.44	16	11.24	8.8	6.52
Postn$^{-/-}$	23.24	23.4	21.43	25.24	18.56	21.65	6.13	8.7	4.45
Tnc$^{-/-}$	10.96	27.04	8.23	13.16	19.64	8.8	11.17	12.6	9.48

4. Results of the partial hepatectomy model

The PHx model was performed to study the liver regeneration. Mice were sacrificed 4, 8, 14 or 21 days after the operation.

4.1. Necroscopies

During the surgical removal of the liver lobes, it has been noticed that Postn$^{-/-}$ mice showed stronger bleeding than control mice. There was no difference observed among control and Tnc$^{-/-}$ mice. Furthermore, nine Postn$^{-/-}$ mice had to be taken out or died during the first four days after PHx. However, only one control mice and none Tnc$^{-/-}$ mice had to be taken out of the experiment. The necroscopies of all sham operated mice showed no abnormalities of the general condition or of the peritoneal cavity as well as a normal liver and gallbladder. Four days after the PHx, occasionally mild adhesions between the resection margins and the diaphragm and/or intestine were observed in all three genotypes. The remaining liver lobes were enlarged and swollen. With progressive regeneration, the size of the liver increased. After 21 days, the liver was enormously swollen, and no difference was observed of the liver among the three genotypes (Fig. 71).

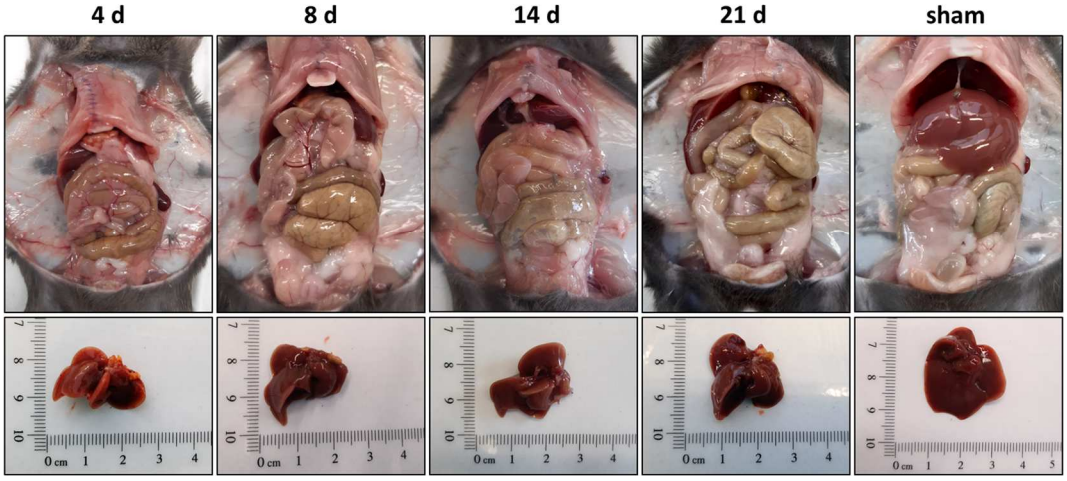

Fig. 71: The liver of control mice after PHx. After removing two-thirds of the liver, the remaining liver lobes swelled and became larger.

The analysis of the LBW-r. % revealed that the original liver mass of all genotypes mass was almost completely restored within eight days after the PHx. In contrast to control and Tnc$^{-/-}$ mice, the LBW-r. % of Postn$^{-/-}$ mice was not constant but

decreased afterwards (Fig. 72).

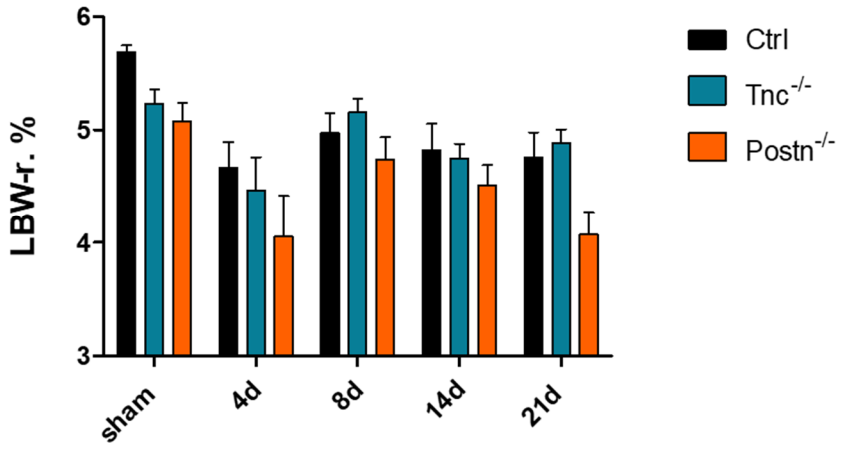

Fig. 72: The LBW-r. % after PHx. The original liver was mass almost completely restored within eight days after PHx. While the ratio was afterwards quite constant in control and $Tnc^{-/-}$ mice, it decreased in $Postn^{-/-}$ mice. Data are expressed as means ± SEM (n=4-6), Kruskal-Wallis test.

V. DISCUSSION

Liver fibrosis is the result of chronic liver diseases and defined by the accumulation of ECM. The main causes are chronic viral hepatitis, alcoholic and non-alcoholic fatty liver disease [2]. The ongoing formation of fibrous scar can ultimately lead to cirrhosis and is related to the development of HCC. Liver cirrhosis causes yearly more than two million deaths per year worldwide and is therefore the 11th most common cause of death [3]. The most effective therapy to treat liver fibrosis and to prevent cirrhosis is still to remove the causative agent [2]. This illustrates how urgently targets for antifibrotic therapies must be found.

One of the main characteristics of the ECM is the active regulation of different functions of neighboring cells, such as proliferation and migration. Thereby, the ECM can actively contribute to tissue homeostasis [122]. During liver damage, the ECM forms a special niche around HPC to influence the fate of these cells and to support liver regeneration [195]. Several studies demonstrated that the two ECM proteins POSTN and TNC are both upregulated during inflammatory and fibrotic processes in the liver and several other organ systems [127,128]. The loss of POSTN results in a reduced fibrosis after a toxin-mediated liver damage and TNC also contributes to liver fibrosis in consequence of an immune-mediated hepatitis in mice [144,196]. Though, the complex interactions of POSTN and TNC with the different cell types during liver damage and regeneration are still not fully resolved. Thus, the aim of the study was to characterize the role of these two ECM proteins during liver damage of different etiologies and following regeneration. Especially the possible influence of POSTN and TNC on the dedifferentiation of the HPC and the DR has been examined. Furthermore, possible compensatory effects of POSTN and TNC were analyzed. Therefore, three different mouse models were performed on Postn$^{-/-}$, Tnc$^{-/-}$ and control mice and subsequently their liver tissue was examined. First, the BDL model to induce a cholestatic damage. Second, the CCl_4 model to induce a toxin-mediated damage and study the following regeneration. The third model was the PHx to further examine the role of POSTN and TNC during liver regeneration after partial resection.

1. The role of Periostin and Tenascin C in liver damage

The histological examination of the liver of healthy $Postn^{-/-}$, $Tnc^{-/-}$ and control mice reveals no difference among the genotypes, which is in line with recent studies [196,197]. Furthermore, the lack of POSTN or TNC does not seem to influence other organs such as heart and pancreas of healthy mice [9,142,198].

Following liver injury, the general condition, and the LBW-r. % was analyzed. In the cholestatic as well as in the toxic model, the LBW-r. % increases and shows no significant difference among $Postn^{-/-}$, $Tnc^{-/-}$ and control mice. The general condition after the BDL is comparable among the three genotypes. The hepatotoxin CCl_4 causes peritoneal inflammation which results in a fibrinous peritonitis and can cause abdominal adhesions. As consequence of the CCl_4 treatment, both knockout mice showed less abdominal adhesions compared to control mice. This can be explained by the fact that POSTN and TNC are involved in inflammatory processes as structural mediators [127,128]. POSTN interacts with collagen I via its EMI domain and enhances the activation of LOX which promotes the collagen cross-linking [132,135]. TNC interacts with a variety of ligands, amongst other things with collagen and fibronectin. The multimodular structure of TNC thereby enhances the structural features of the ECM [128]. Thus, POSTN and TNC promote fibrillogenesis and contribute to stronger adhesions in consequence of the peritoneal inflammation.

Following cholestatic and toxic liver injury, *Postn* and *Tnc* mRNA levels as well as the protein expressions are upregulated. Immunohistochemical analyses of both proteins revealed that they are not expressed in the normal liver. Instead, in consequence of the BDL and CCl_4 treatment, the expression of POSTN and TNC increased with progressive liver damage. Both proteins are located besides necrotic cells and along fibrotic septa, whereby they are stronger expressed in consequence of the cholestatic damage than after toxic injuries. Other studies demonstrated an increase of POSTN in consequence of tissue injury in several organs. For example, in a mouse model of acute pancreatitis, an upregulation of POSTN during the inflammatory processes can be observed [142]. Moreover, the POSTN expression increases in the aorta during an abdominal aortic aneurysm mouse model [199]. Similar results regarding the TNC expression are shown in recent

studies. TNC is upregulated in course of a concanavalin A mediated hepatitis as well as after a hepatic ischemia and reperfusion injury in wildtype mice [165,200]. The fact, that POSTN and TNC are stronger expressed following a cholestatic than toxic damage may be because the BDL induces a stronger inflammation of the liver parenchyma than the CCl_4 treatment. On the other hand, it may also be because the activation of individual ECM proteins might depend on the cause of damage. A cholestatic-obstructive injury could lead to a stronger expression of POSTN and TNC than a toxic damage.

Our study shows no differences in the POSTN expression among $Tnc^{-/-}$ and control mice in consequence of the BDL or CCl_4 treatment. Therefore, the loss of TNC does not cause any compensatory increase of the POSTN expression in $Tnc^{-/-}$ mice compared to control mice. However, the situation is different with the expression of TNC. Compared to control mice, $Postn^{-/-}$ mice show a significant increased TNC expression in the early phase after BDL and CCl_4 treatment. This can be explained by a compensatory effect of TNC and accentuates the importance of POSTN. If POSTN is not available, the liver might try to provide other ECM molecules to contribute to tissue homeostasis and liver regeneration. So far, no evidence for compensatory features of POSTN and TNC during liver damage and regeneration has been reported.

As a result of the BDL and the CCl_4 treatment, $Postn^{-/-}$ mice show a higher inflammatory reaction than control mice, due to more necrotic hepatocytes during fibrogenesis. A recent study demonstrates that $Postn^{-/-}$ mice show an attenuated infiltration with macrophages after CCl_4 treatment [144]. These data suggest that the reduced recruitment of macrophages leads to a reduced phagocytosis of necrotic hepatocytes in $Postn^{-/-}$ mice. The role of macrophages will be further discussed below. Instead, $Tnc^{-/-}$ mice showed a similar inflammatory reaction after the BDL and only after the CCl_4 treatment, more necrotic hepatocytes than control mice. A recent study reports that in course of a concanavalin A-mediated hepatitis, $Tnc^{-/-}$ mice showed a weaker infiltration with inflammatory cells than control mice [165]. The impact of TNC may therefore depend on the cause of liver injury. During toxin- or immune-mediated liver damage, the impact of TNC is greater and an attenuated infiltration with macrophages may cause the reduced degradation of hepatocytes.

The ongoing inflammation of the liver tissue in consequence of the BDL or CCl_4 treatment causes the fibrotic reaction and the abnormal accumulation of ECM. Therefore, we analyzed the distribution of ACTA2 positive cells and the collagen deposition. In the CCl_4 and in the BDL model, the distribution pattern of ACTA2 positive cells corresponds to the pattern of collagen deposition. In all three genotypes, the amount of ACTA2 positive cells increases with ongoing liver damage and accumulation of ECM. These aMF are located next to injured cells and along fibrotic septa. In the BDL model, the fibrous scar expands from the portal tract, whereas in the CCl_4 model, the fibrous reaction starts around the central vein. These findings are in agreement with recent studies which postulate aHSC and aPF as the major sources of collagen producing cells depending on the etiology [23,41]. However, $Postn^{-/-}$ mice show an earlier activation of HSC and PF in the immunohistochemistry and a higher *Acta2* mRNA expression in the early phase of the cholestatic and toxic liver damage than control mice. This suggests that POSTN might have a protective function on hepatocytes. A recent study demonstrates, that POSTN can protect osteoblasts from melatonin-induced apoptosis *in vitro* [201]. However, in a more advanced stage of liver damage, $Postn^{-/-}$ mice showed a lower ACTA2 expression as well as less fibrosis compared to control mice. Furthermore, $Postn^{-/-}$ mice showed an impaired generation of collagen rich matrix following BDL. These findings are in line with another study which shows that $Postn^{-/-}$ mice are protected from CCl_4-induced liver fibrosis and thereby express less ACTA2 than control mice [144]. Additionally, it is known that POSTN contributes to fibrosis in other organs. In the heart, for instance, it is essential for the stiffness of the heart muscle after myocardial infarction. The lack of POSTN causes a reduced amount of ACTA2 positive cells and collagen which results in cardiac rupture in mice [9]. These data suggest that an appropriate and time-dependent expression of POSTN is required for tissue homeostasis. POSTN promotes cellular survival in the early phase of tissue damage but contributes to fibrosis during chronic damage.

In our study, $Tnc^{-/-}$ mice show a similar expression of ACTA2 and collagen deposition as control mice during fibrogenesis. Therefore, TNC might only play a minor part in the development of a cholestatic or toxin-mediated liver fibrosis. A recent study ascribes TNC a more important role. In an immune-mediated

hepatitis mouse model, the loss of TNC leads to a reduced collagen deposition. However, the authors injected concanavalin A in female mice with a BALB/c background [196]. It can therefore be assumed that the gender and the background might have a significant influence of the susceptibility to liver fibrosis in mice. Furthermore, the impact of TNC may differ from the cause of injury and explain the controversial results.

In conclusion, our study demonstrates that the influence of POSTN and TNC in liver damage varies according to the cause of injury. Whereas POSTN may have a protective function on hepatocytes and contributes to liver fibrosis, TNC seems to only play a redundant role. Furthermore, the lack of POSTN leads to a compensatory increase of TNC in the early stage of injury. To our knowledge, this is the first study which indicates that the lack of one ECM could lead to a compensatory increase of another one.

2. The role of Periostin and Tenascin C during liver regeneration

On the one hand, liver regeneration includes the degradation of necrotic hepatocytes and fibrous scarring. On the other hand, it comprises the regeneration of new hepatocytes and the restorage of liver mass.

During liver regeneration after toxic damage, POSTN is only minimal expressed in the wall of the central vein and decreases with ongoing regeneration in $Tnc^{-/-}$ and control mice. TNC is also only weakly expressed around the central vein and along the fibrotic septa in $Postn^{-/-}$ and control mice. However, in control mice, the TNC expression decreases continuously, whereas $Postn^{-/-}$ mice show a prolonged TNC expression. One reason for the prolonged TNC expression in $Postn^{-/-}$ mice could be, as already mentioned before, that the loss of POSTN causes a compensatory increase of TNC. This effect could persist even if the causative agent has already been removed. Another reason could be the fact that POSTN-deficiency causes a reduced MMP expression, which results in an impaired degradation of ECM. In a high fat-diet mouse model, the loss of POSTN causes an attenuated production of MMP-2 and -13 and thereby leads to an impaired atherosclerotic and rheumatic cardiac valve degeneration [138].

However, not only the degradation of TNC is impaired in $Postn^{-/-}$ mice. During liver regeneration following CCl_4 treatment, the collagenous septa become thinner and

interrupted. Thereby, the fibrous scar is removed, and the normal liver architecture restored. In contrast to control mice, Postn$^{-/-}$ as well as Tnc$^{-/-}$ mice show a slightly impaired degradation of the fibrous septa. One reason for this may be a lower infiltration with macrophages. POSTN is a potent chemoattractant for macrophages following liver injury [144]. Macrophages express MMPs and the TNF-related apoptosis-inducing ligand (TRAIL) to induce apoptosis in MF. Through phagocytosis of apoptotic cells and degradation of ECM by MMPs (e.g. MMP-13), macrophages contribute to tissue homeostasis and fibrosis regression [99]. Like Postn$^{-/-}$ mice, several studies demonstrate that Tnc$^{-/-}$ mice also show a reduced expression of several MMPs (e.g. MMP-2 and -13) as a reaction of chronic pressure overload or allergen-induced asthma. This results in an improved cardiac function and attenuates asthma [10,202].

Besides the degradation of the fibrous scar, the degradation of necrotic hepatocytes is a crucial part of liver regeneration. Especially, the BDL causes multiple confluent necroses of the liver parenchyma. In course of the fibrogenesis, these confluent necroses are resorbed and new hepatocytes generated. While Tnc$^{-/-}$ and control mice gradually degrade necroses, the loss of POSTN lead to an impaired degradation of the necrotic hepatocytes and an impaired restoration of liver parenchyma. As described above, an attenuated infiltration with macrophages and the resulting reduced phagocytic activity can cause the impaired degradation of necrotic cells in Postn$^{-/-}$ mice [144]. Furthermore, different studies already demonstrate that POSTN is urgently needed for a proper regeneration of many organs. Following a cerulein-induced acute pancreatitis for instance, Postn$^{-/-}$ mice show an impaired regeneration with a sever pancreatic atrophy [9,142]. Following severe or chronic liver damage, HPC can be activated and contribute to the regeneration of liver tissue. The bipotential HPC can transdifferentiate into biliary cells or into new hepatocytes which mature on the way from the periportal area to the central vein [102,203]. A recent study reveals that mature hepatocytes could also be an origin of HPC and contribute to liver regeneration via reversible ductular metaplasia [111]. As a result of the BDL, Sox9-expressing hepatocytes are mainly located periportal with a portocentral gradient. This observation suggests that hepatocytes could have progenitor features and probably lose them during their maturation. Furthermore, the HPC can directly be regulated by the ECM of

the HPC-nice. The ECM proteins have the capacity to regulate surrounding cells and thereby promote liver regeneration [5]. So far, the influence of POSTN and TNC on the dedifferentiation of HPC is not known. In the BDL model of our study, $Postn^{-/-}$ mice show a lower *Sox9* mRNA expression in the early phase and a generally lower protein expression compared to control mice. Although $Postn^{-/-}$ mice show the same amount of DR as control mice, the new bile ducts are smaller and less well formed. Similar results can be observed during pancreatic regeneration. In case of pancreatitis, acinar cells transdifferentiate into a progenitor-like cell type with ductal structures, called acinar-to-ductal metaplasia (ADM). This mechanism contributes to the regeneration of the exocrine compartment of the pancreas [204]. In a mouse model of acute pancreatitis, the loss of POSTN leads to an impaired redifferentiation of these ADM [142]. These findings suggest that POSTN could have a stimulating effect on the proliferation and differentiation of HPC in course of a cholestatic damage. POSTN is required for a proper regeneration of the liver parenchyma by HPC. Instead, the $Tnc^{-/-}$ mice show a stronger Sox9 protein expression in the earlier phase and in general a higher mRNA expression in course of the cholestatic damage but without any differences in the architecture or the amount of the DR. This indicates that the loss of TNC leads to an early stimulation of HPC to promote the regenerative process. These findings are in line with an earlier report showing that TNC influences the migration and proliferation of neural progenitors. Therefore, TNC-deficiency leads to faster maturation of oligodendrocyte precursors in mice [205].

In contrast to the cholestatic model, the activation of progenitor-like hepatocytes/HPC seems to play no or only a minor role in the toxic CCl_4 model because the SOX9 expression is limited to biliary cells. One reason for this could be the fact that CCl_4 causes centrilobular single cell necrosis of hepatocytes and that pericentral mature hepatocytes probably no longer possess progenitor features. On the other hand, the cause of injury could have an influence on the expression of markers and/or on the origin of the HPC. So far, there is no marker which labels exclusively HPC [203]. Therefore, a CCl_4-mediated damage might not promote the SOX9 expression in HPC and/or the activation of progenitor feature of mature hepatocytes. Nevertheless, the DR following CCl_4 treatment is characterized by small and diffuse scattered new bile ducts in the parenchyma. It

is reported that the administration of CCl_4 causes apoptosis of large cholangiocytes. Smaller cholangiocytes seems to be more resistant and compensate the loss of mass by an increased proliferation [206]. However, after the eight-weeks CCl_4 treatment, the *Sox9* mRNA expression level as well as the number of DR is in both knockouts lower than in control mice. These findings indicate that the restorage of liver parenchyma is impaired in $Postn^{-/-}$ and $Tnc^{-/-}$ mice during toxic damage. In the subsequent regenerative phase, $Postn^{-/-}$ mice show an increased number of new bile ducts for a longer period than $Tnc^{-/-}$ and control mice. This fact confirms the hypothesis that POSTN contributes to a proper differentiation of HPC. POSTN-deficiency results in an inadequate redifferentiation of the DR and impairs tissue regeneration.

Liver parenchyma can also be restored by proliferating mature hepatocytes [110]. During the cholestatic fibrogenesis, $Tnc^{-/-}$ and control mice show the same trend of the HPI. The HPI increases until a peak on day seven and decreases afterwards. Instead, in $Postn^{-/-}$ mice, the HPI is quite constant and always higher than in control mice. Interestingly, the proliferation rate of hepatocytes correlates thereby with the degradation of confluent necroses. While in $Tnc^{-/-}$ and control mice most of the necroses are degraded until day seven, $Postn^{-/-}$ mice show an impaired degradation and in general more confluent necroses. This suggests that $Postn^{-/-}$ mice show a prolonged proliferation of hepatocytes due to an insufficient degradation of the necrotic tissue. During the CCl_4 treatment, the HPI of control mice gradually increases, whereas $Postn^{-/-}$ mice show a continuously higher and increased proliferation rate. This result confirms that POSTN could improve liver regeneration. The increased number of necrotic hepatocytes might result in the increased proliferation of remaining hepatocytes. Similar results are reported in other organs. POSTN-deficiency in mice causes pancreas atrophy after acute pancreatitis, due to an insufficient regeneration [142]. Instead in $Tnc^{-/-}$ mice of our study, the HPI increases only until a peak after four weeks and decreases afterwards. This suggests that TNC-deficiency impairs the proliferation of mature hepatocytes during chronic toxic liver injury. This finding is consistent with another study, which reveals that TNC-deficiency results in impaired spinal cord regeneration following compression injury in mice [207].

During the regenerative phase after the CCl_4 treatment, the proliferation rate

continuously decreases in control mice. Surprisingly, the HPI of Postn$^{-/-}$ mice is lower than in control mice. This suggests that the proliferation of hepatocytes in Postn$^{-/-}$ mice might depend on whether the causative agent is still present or not. It seems that hepatocytes of Postn$^{-/-}$ mice have this high proliferation rate only during acute liver damage. If the causative agent is removed, POSTN-deficiency leads to an attenuated regeneration of new hepatocytes. In Tnc$^{-/-}$ mice, the proliferation rate is constantly increased and higher than in control mice. This prolonged proliferation rate after the CCl_4 treatment corroborates the impaired regenerative capacity of Tnc$^{-/-}$ mice in case of toxic damage. TNC seems to be needed for a fast and more effective regeneration when the causative agent is removed.

Proliferation of mature hepatocytes is furthermore the main mechanism to restore liver mass after PHx [121]. The analysis of the LBW-r. % in course of the PHx reveals that the liver mass was almost restored within eight days. However, after 21 days, the LBW-r. % in Postn$^{-/-}$ mice slightly decreased and was lower than in Tnc$^{-/-}$ and control mice. This fact confirms the reduced regenerative capacity of Postn$^{-/-}$ mice and corroborates that POSTN is required for regeneration. Similar observations are reported in a recently published study. Postn$^{-/-}$ mice show a significant lower LBW-r. % 2, 8 and 14 days after PHx [197]. TNC seems to only play a minor role for the restoration of the liver mass following PHx, as there is no difference of the LBW-r. % between Tnc$^{-/-}$ and control mice. This indicates that the influence of TNC highly dependents of the cause of injury and the following regeneration process.

3. Limitations of the study

Rodent models are the gold standard to study liver fibrosis. They make it possible to investigate complex cell interactions during fibrogenesis and regeneration [208]. In our study, we used the BDL model. It is the most widely used one to study pathogenic mechanisms in the consequence of cholestatic injury. It is a fast, reliable, and highly reproducible model for liver fibrosis. After three to four weeks, a strong fibrotic reaction is present. However, it is possible that if the gallbladder or the bile duct is ruptured bile can leak into the peritoneal cavity and can cause severe peritonitis [170]. In our study, only two mice had to be euthanized due to the

consequences of the operation. The other mice did not show evidence of pain or suffering. The second model of our study, the CCl_4 model is the most common used model to induce a toxic damage. The application via i.p. injections is easy to perform and allows a strong and reproducible liver fibrosis after four to six weeks. According to the literature, i.p. injections can cause a mild peritoneal inflammation and local irritations of the skin [174]. In our experiments, multiple adhesions between the liver, diaphragm and/or intestine after long term application were observed. Strong adhesions could have influenced our results negatively as well as the animal welfare. Both knockout mice show less abdominal adhesions compared to control mice. The third model we used, the PHx model, is the gold standard to study liver regeneration after partial hepatectomy. It allows exact and time dependent investigations of molecular aspects. It is fast to perform but there is a risk to penetrate the diaphragm and the gallbladder or to harm surrounding vessel and the biliary tree [179]. During our operations, we observed that especially $Postn^{-/-}$ mice show occasional heavy bleedings which could explain the increased mortality rate. $Tnc^{-/-}$ and control mice do not show any special abnormalities or signs of pain and suffering after the operation.

The gender, the age and the genetic background could have an influence on the susceptibility for liver fibrosis and on the regeneration process. Recent studies demonstrate that different mouse strains are differently prone towards CCl_4-induced and diet-induced liver damage [168,169]. This suggests that referring to the cholestatic BDL-model, the genetic background could have an impact on the fibrotic reaction. In the PHx model, female mice have a significant decreased or delayed proliferation of hepatocytes and restoration of the liver mass [181]. Furthermore, the regenerative capability decreases with increasing age of rodents. Younger animals show higher levels of pro-restorative cytokines, such as IL-6 [182]. Therefore, only male knockouts and corresponding control littermates of the same age were used in each of our experimental groups. Even if these three mouse models are appropriate models to study the mechanisms of liver fibrosis and regeneration, one should consider that they do not completely represent the human situation. The underlying liver disease has an impact on the fibrosis and regeneration as well. Furthermore, mice have a faster metabolism which also influences the results [209]. They develop a strong fibrotic reaction within weeks,

whereas it takes years in humans [18,170,174]. In summary, mouse models are currently still the best option for a major understanding of fibrogenesis and regeneration, but they are not suitable to understand all aspects of human liver diseases.

The fact that our results do not achieve statistical significance limits our study, as well. We observed only trends which provide information about the functional relevance of POSTN and TNC during liver damage and regeneration.

4. Conclusion and outlook

The data of this study show various functions of POSTN and TNC during liver damage and regeneration. Even if both ECM proteins do not have a statistically significant impact on the fibrotic response or on the regenerative process of the liver, trends can still be observed. The influence of POSTN and TNC varies depending on the cause of damage and the regenerative mechanism.

POSTN seems to have a protective function on hepatocytes. It preserves the liver from cholestatic and toxin-mediated injury. Following liver injury, POSTN takes part in the wound-healing response of the liver and contributes to liver fibrosis. Furthermore, POSTN is required for a regular differentiation of HPC and a proper restoration of the parenchyma by proliferating hepatocytes. During liver regeneration, POSTN promotes the degradation of necrotic and fibrotic tissue and contributes thereby to tissue homeostasis.

The impact of TNC during liver fibrosis and regeneration seems to depend on the cause of injury. Whereas it does not influence the dedifferentiation of HPC during a cholestatic damage, it promotes the DR and thereby liver regeneration during a toxin-mediated injury. Furthermore, TNC does not influence the accumulation of fibrous scar but it contributes to the degradation of the ECM. Once the causative agent is removed, TNC contributes to a faster restoration of liver mass by proliferating hepatocytes.

In summary, our data suggest that POSTN and TNC contribute to a microenvironment which facilitates tissue regeneration and fibrosis resolution. However, further studies must be performed to better understand the molecular mechanisms regarding their influence in tissue homeostasis. Therefore, more analyses are performed currently to study the microenvironment around the

fibrotic and necrotic tissue, especially the amount and types of macrophages. Furthermore, the liver of partial hepatectomized $Postn^{-/-}$, $Tnc^{-/-}$ and control mice is currently being examined. A systemic evaluation of the interactions between ECM molecules and their surrounding cells will support the development of new therapies to treat liver fibrosis and to support liver regeneration.

VI. SUMMARY

Chronic or severe liver damage results in liver fibrogenesis. Thereby, ECM-producing myofibroblasts are activated and secrete an excessive amount of ECM proteins, such as POSTN and TNC. Besides the fibrotic reaction, bipotential HPC start to proliferate following severe liver injury. These HPC can transdifferentiate either into cholangiocytes or into hepatocytes which is histologically observed as DR. Thereby, the ECM forms a special niche around the HPC to influence their fate and contribute to tissue homeostasis. However, the influence of POSTN and TNC on the HPC has not been investigated so far. Therefore, the function of POSTN and TNC in different causes of liver damage and regeneration was investigated. Especially their impact on the dedifferentiation of HPC was analyzed. Furthermore, possible compensating effects between POSTN and TNC have been considered. Therefore, three different mouse model were performed on $Postn^{-/-}$, $Tnc^{-/-}$ and control mice: the BDL model to induce a cholestatic damage, the CCl_4 model to induce a toxic damage and the PHx model to study more particularly the regeneration process.

Data of this study revealed that POSTN has a protective function on hepatocytes and accelerate fibrillogenesis following cholestatic or toxin-mediated injury. During liver regeneration, POSTN promotes the proliferation and differentiation of HPC. Moreover, it ameliorates the degradation of necrotic hepatocytes and the fibrous scar to restore a normal liver architecture. Furthermore, our study demonstrates that the loss of POSTN results in a compensatory increase of TNC in the early period of injury, whereas the loss of TNC causes no such effect.

TNC seems to only play a redundant role during fibrogenesis. Instead during liver regeneration, it enhances the degradation of the ECM and promotes the proliferation of HPC following toxin-mediated damage.

Taken together, our data demonstrate that even if POSTN and TNC do not significantly contribute to remodeling of the liver tissue both proteins support the wound-healing response of the liver. Their function varies thereby depending on the cause of damage and the cell types involved. However, further studies are required to clarify the underlying mechanisms.

VII. ZUSAMMENFASSUNG

Chronische oder schwere Leberschädigung führt zur Leberfibrogenese. Dabei werden ECM-produzierende Myofibroblasten aktiviert und sezernieren übermäßige Menge an ECM, wie POSTN und TNC. Neben der fibrotischen Reaktion beginnen nach einer schweren Schädigung bipotentielle HPC zu proliferieren. Diese HPC können sich entweder zu Cholangiozyten oder zu Hepatozyten differenzieren, was histologisch als duktuläre Reaktion zu erkennen ist. Dabei bildet die ECM eine spezielle Nische um die HPC, um deren Schicksal zu beeinflussen und zur Gewebehomöostase beizutragen. Der Einfluss von POSTN und TNC auf HPC ist jedoch bisher nicht untersucht worden. Daher wurde die Funktion von POSTN und TNC bei verschiedenen Ursachen der Leberschädigung und Regeneration untersucht. Insbesondere ihr Einfluss auf die Dedifferenzierung von HPC wurde analysiert. Darüber hinaus wurden mögliche kompensatorische Effekte zwischen POSTN und TNC berücksichtigt. Hierzu wurden drei verschiedene Mausmodelle an $Postn^{-/-}$, $Tnc^{-/-}$ und Kontrollmäusen angewandt: das BDL Modell um einen cholestatischen Schaden zu induzieren, das CCl_4 Modell um einen toxischen Schaden zu induzieren und das PHx Modell um im Speziellen die Regeneration zu untersuchen.

Die Daten dieser Studie zeigen, dass POSTN eine Schutzfunktion gegenüber Hepatozyten besitzt und die Fibrillogenese nach cholestatischer oder Toxin-vermittelter Schädigung beschleunigt. Während der Leberregeneration fördert POSTN die Proliferation und Differenzierung von HPC. Darüber hinaus verbessert es den Abbau nekrotischer Hepatozyten und des fibrösen Narbengewebes, um eine normale Leberarchitektur wiederherzustellen. Darüber hinaus zeigt unsere Studie, dass der Verlust von POSTN zu einem kompensatorischen Anstieg von TNC in der frühen Phase der Schädigung führt, während der Verlust von TNC keinen solchen Effekt verursacht.

TNC scheint während der Fibrogenese nur eine redundante Rolle zu spielen. Stattdessen verstärkt es während der Leberregeneration den Abbau der ECM und fördert die Proliferation von HPC nach Toxin-vermittelter Schädigung.

Zusammenfassend zeigen unsere Daten, dass selbst wenn POSTN und TNC nicht

signifikant zur Remodellierung des Lebergewebes beitragen, beide Proteine die Wundheilungsreaktion der Leber unterstützen. Ihre Funktion variiert dabei in Abhängigkeit von der Ursache der Schädigung und den beteiligten Zelltypen. Es sind jedoch weitere Studien erforderlich, um die zugrunde liegenden Mechanismen zu klären.

VIII. LITERATURE

1. Malato, Y. *et al.* Fate tracing of mature hepatocytes in mouse liver homeostasis and regeneration. *J. Clin. Invest.* **121**, (2011).

2. Bataller, R. & Brenner, D. A. Liver fibrosis. *J. Clin. Invest.* **115**, (2005).

3. Asrani, S. K., Devarbhavi, H., Eaton, J. & Kamath, P. S. Burden of liver diseases in the world. *Journal of Hepatology* **70**, 151–171 (2019).

4. Bataller, R. & Brenner, D. A. Hepatic stellate cells as a target for the treatment of liver fibrosis. *Seminars in Liver Disease* **21**, 437–451 (2001).

5. Bonnans, C., Chou, J. & Werb, Z. Remodelling the extracellular matrix in development and disease. *Nature Reviews Molecular Cell Biology* **15**, 786–801 (2014).

6. Sato, K. *et al.* Ductular Reaction in Liver Diseases: Pathological Mechanisms and Translational Significances. *Hepatology* **69**, 420–430 (2019).

7. Issa, R. *et al.* Spontaneous recovery from micronodular cirrhosis: Evidence for incomplete resolution associated with matrix cross-linking. *Gastroenterology* **126**, 1795–1808 (2004).

8. Saile, B. & Ramadori, G. Fibrogenese – ZirrhoseFibrogenic cirrhosis. *Der Gastroenterol.* **2**, 228–237 (2007).

9. Shimazaki, M. *et al.* Periostin is essential for cardiac healing after acute myocardial infarction. *J. Exp. Med.* **205**, 295–303 (2008).

10. Podesser, B. K. *et al.* Tenascin-C promotes chronic pressure overloadinduced cardiac dysfunction, hypertrophy and myocardial fibrosis. *J. Hypertens.* **36**, 847–856 (2018).

11. Kumar, V., Abbas, A. K. & Aster, J. C. *Robbins and Cotran Pathologic Basis of Disease*. (Elsevier Inc., 2015).

12. König, H. E. & Liebich, H. *Anatomie der Haussäugetiere*. (Schattauer, 2009).

13. Rogers, A. B. & Dintzis, R. Z. Hepatobiliary System. in *Comparative Anatomy*

and Histology 229–239 (Elsevier, 2018). doi:10.1016/b978-0-12-802900-8.00013-0

14. von Engelhardt, W. & Breves, G. *Physiologie der Hasutiere*. (Enke, 2004).

15. Sinowatz, F. & Hees, H. *Histologie - Kurzlehrbuch der Zytologie und mikroskopischen Anatomie*. (2012).

16. Hernandez-Gea, V. & Friedman, S. L. Pathogenesis of Liver Fibrosis. *Annu. Rev. Pathol. Mech. Dis.* **6**, 425–456 (2011).

17. Friedman, S. L. Liver fibrosis - From bench to bedside. *Journal of Hepatology, Supplement* **38**, (2003).

18. Pellicoro, A., Ramachandran, P., Iredale, J. P. & Fallowfield, J. A. Liver fibrosis and repair: Immune regulation of wound healing in a solid organ. *Nature Reviews Immunology* **14**, 181–194 (2014).

19. Canbay, A., Friedman, S. & Gores, G. J. Apoptosis: The nexus of liver injury and fibrosis. *Hepatology* **39**, 273–278 (2004).

20. Xu, F., Liu, C., Zhou, D. & Zhang, L. TGF-β/SMAD Pathway and Its Regulation in Hepatic Fibrosis. *Journal of Histochemistry and Cytochemistry* **64**, 157–167 (2016).

21. Casini, A. *et al.* Neutrophil-derived superoxide anion induces lipid peroxidation and stimulates collagen synthesis in human hepatic stellate cells: Role of nitric oxide. *Hepatology* **25**, 361–367 (1997).

22. Viñas, O. *et al.* Human hepatic stellate cells show features of antigen-presenting cells and stimulate lymphocyte proliferation. *Hepatology* **38**, 919–929 (2003).

23. Iwaisako, K. *et al.* Origin of myofibroblasts in the fibrotic liver in mice. *Proc. Natl. Acad. Sci. U. S. A.* **111**, (2014).

24. Kisseleva, T. *et al.* Bone marrow-derived fibrocytes participate in pathogenesis of liver fibrosis. *J. Hepatol.* **45**, 429–438 (2006).

25. Friedman, S. L. Mechanisms of Hepatic Fibrogenesis. *Gastroenterology* **134**,

1655–1669 (2008).

26. Arthur, M. J. P. *Fibrogenesis II. Metalloproteinases and their inhibitors in liver fibrosis*. (2000).

27. Duarte, S., Baber, J., Fujii, T. & Coito, A. J. Matrix metalloproteinases in liver injury, repair and fibrosis. *Matrix Biology* **44**–**46**, 147–156 (2015).

28. Roeb, E. Matrix metalloproteinases and liver fibrosis (translational aspects). *Matrix Biology* **68**–**69**, 463–473 (2018).

29. Iwaisako, K., Brenner, D. A. & Kisseleva, T. What's new in liver fibrosis? The origin of myofibroblasts in liver fibrosis. *J. Gastroenterol. Hepatol.* **27**, 65–68 (2012).

30. Lua, I. *et al.* Characterization of hepatic stellate cells, portal fibroblasts, and mesothelial cells in normal and fibrotic livers. *J. Hepatol.* **64**, 1137–1146 (2016).

31. Asahina, K. *et al.* Mesenchymal origin of hepatic stellate cells, submesothelial cells, and perivascular mesenchymal cells during mouse liver development. *Hepatology* **49**, 998–1011 (2009).

32. Guyot, C. *et al.* Hepatic fibrosis and cirrhosis: The (myo)fibroblastic cell subpopulations involved. *International Journal of Biochemistry and Cell Biology* **38**, 135–151 (2006).

33. Lepreux, S. & DesmouliÃ¨re, A. Human liver myofibroblasts during development and diseases with a focus on portal (myo)fibroblasts. *Front. Physiol.* **6**, 173 (2015).

34. Geerts, A. History, Heterogeneity, Developmental Biology, and Functions of Quiescent Hepatic Stellate Cells. *Semin. Liver Dis.* **21**, 311–336 (2001).

35. Sato, M., Suzuki, S. & Senoo, H. Hepatic Stellate Cells: Unique Characteristics in Cell Biology and Phenotype. *Cell Struct. Funct.* **28**, 105–112 (2003).

36. Kendall, T. J. *et al.* p75 neurotrophin receptor signaling regulates hepatic myofibroblast proliferation and apoptosis in recovery from rodent liver fibrosis. *Hepatology* **49**, 901–910 (2009).

37. Casini, A. *et al.* Neutrophil-derived superoxide anion induces lipid peroxidation and stimulates collagen synthesis in human hepatic stellate cells: Role of nitric oxide. *Hepatology* **25**, 361–367 (1997).

38. Friedman, S. L. Hepatic Stellate Cells: Protean, Multifunctional, and Enigmatic Cells of the Liver. doi:10.1152/physrev.00013.2007

39. Hashmi, A. Z. *et al.* Adenosine inhibits cytosolic calcium signals and chemotaxis in hepatic stellate cells. *Am J Physiol Gastrointest Liver Physiol* **292**, 395–401 (2007).

40. Kikuchi, A. *et al.* Platelet-Derived Growth Factor Receptor α Contributes to Human Hepatic Stellate Cell Proliferation and Migration. *Am. J. Pathol.* **187**, 2273–2287 (2017).

41. Mederacke, I. *et al.* ARTICLE Fate tracing reveals hepatic stellate cells as dominant contributors to liver fibrosis independent of its aetiology. *Nat. Commun.* (2013). doi:10.1038/ncomms3823

42. Iwaisako, K. *et al.* Origin of myofibroblasts in the fibrotic liver in mice. doi:10.1073/pnas.1400062111

43. Krenkel, O. & Tacke, F. Liver macrophages in tissue homeostasis and disease. *Nat. Rev. Immunol.* **17**, 306–321 (2017).

44. Maher, J. J. Leukocytes as Modulators of Stellate Cell Activation. *Alcohol. Clin. Exp. Res.* **23**, 917–921 (1999).

45. Friedman, S. L. & Arthur, M. J. P. *Activation of Cultured Rat Hepatic Lipocytes by Kupffer Cell Conditioned Medium Direct Enhancement of Matrix Synthesis and Stimulation of Cell Proliferation via Induction of Platelet-derived Growth Factor Receptors*.

46. Rojkind, M., Giambrone, M.-A. & Biempica, L. *Collagen Types in Normal and Cirrhotic Liver*. *Gastroenterology* **76**, (1979).

47. Lindquist, J. N., Marzluff, W. F. & Stefanovic, B. *Fibrogenesis III. Posttranscriptional regulation of type I collagen*. (2000).

48. Bataller, R. *et al.* Activated human hepatic stellate cells express the renin-

angiotensin system and synthesize angiotensin II. *Gastroenterology* **125**, 117–125 (2003).

49. Tuchweber, B., Desmoulière, A., Bochaton-Piallat, M. L., Rubbia-Brandt, L. & Gabbiani, G. Proliferation and phenotypic modulation of portal fibroblasts in the early stages of cholestatic fibrosis in the rat. *Lab. Investig.* **74**, 265–278 (1996).

50. Beaussier, M. *et al.* Prominent contribution of portal mesenchymal cells to liver fibrosis in ischemic and obstructive cholestatic injuries. *Lab. Investig.* **87**, 292–303 (2007).

51. Knittel, T. *et al.* Rat liver myofibroblasts and hepatic stellate cells: different cell populations of the fibroblast lineage with fibrogenic potential. *Gastroenterology* **117**, 1205–21 (1999).

52. Wells, R. G., Kruglov, E. & Dranoff, J. A. Autocrine release of TGF-β by portal fibroblasts regulates cell growth. *FEBS Lett.* **559**, 107–110 (2004).

53. Lamouille, S., Xu, J. & Derynck, R. Molecular mechanisms of epithelial-mesenchymal transition. *Nat Rev Mol Cell Biol* **15**, 178–196 (2014).

54. Iwano, M. *et al.* Evidence that fibroblasts derive from epithelium during tissue fibrosis Find the latest version : Evidence that fibroblasts derive from epithelium during tissue fibrosis. **110**, 341–350 (2002).

55. Willis, B. C. *et al.* Induction of epithelial-mesenchymal transition in alveolar epithelial cells by transforming growth factor-β1: Potential role in idiopathic pulmonary fibrosis. *Am. J. Pathol.* **166**, 1321–1332 (2005).

56. Sicklick, J. K. *et al.* Evidence for epithelial-mesenchymal transitions in adult liver cells. *Am. J. Physiol. Liver Physiol.* **291**, G575–G583 (2006).

57. Taura, K. *et al.* Hepatocytes Do Not Undergo Epithelial-Mesenchymal Transition in Liver Fibrosis in Mice. doi:10.1002/hep.23368

58. Chu, A. S. *et al.* Lineage tracing demonstrates no evidence of cholangiocyte epithelial-to-mesenchymal transition in murine models of hepatic fibrosis NIH Public Access. *Hepatology* **53**, 1685–1695 (2011).

59. Forbes, S. J. *et al.* A Significant Proportion of Myofibroblasts Are of Bone Marrow Origin in Human Liver Fibrosis. *Gastroenterology* **126**, 955–963 (2004).

60. Gastrointestinal, H. & Pathology, P. Migration of Fibrocytes in Fibrogenic Liver Injury. *AJPA* **179**, 189–198 (2011).

61. Pinzani, M., Gesualdo, L., Sabbah, G. M. & Abboud, H. E. *Effects of Platelet-derived Growth Factor and Other Polypeptide Mitogens on DNA Synthesis and Growth of Cultured Rat Liver Fat-storing Cells*.

62. Borkham-Kamphorst, E. *et al.* Pro-fibrogenic potential of PDGF-D in liver fibrosis. *J. Hepatol.* **46**, 1064–1074 (2007).

63. Marra, F. *et al.* Extracellular signal-regulated kinase activation differentially regulates platelet-derived growth factor's actions in hepatic stellate cells, and is induced byIn Vivo liver injury in the rat. *Hepatology* **30**, 951–958 (1999).

64. Marra, F. *et al. Phosphatidylinositol 3-Kinase Is Required for Platelet-Derived Growth Factor's Actions on Hepatic Stellate Cells*. *GASTROENTEROLOGY* **112**, (1997).

65. Bachem, M. G. *et al. Virchows Archiv B Cell Pathology Tumor necrosis factor alpha (TNF) and transforming growth factor [31 (TGFI31) stimulate fibronectin synthesis and the transdifferentiation of fat-storing cells in the rat liver into myofibroblasts*. *Virchows Archiv B Cell Pathol* **63**, (1993).

66. Schnabl, B. The role of Smad3 in mediating mouse hepatic stellate cell activation. *Hepatology* **34**, 89–100 (2001).

67. Dooley, S. *et al.* Smad7 prevents activation of hepatic stellate cells and liver fibrosis in rats. *Gastroenterology* **125**, 178–191 (2003).

68. Iredale, J. P., Murphy, G., Hembry, R. M., Friedman, S. L. & Arthur, M. J. P. *Rapid Publication Human Hepatic Lipocytes Synthesize Tissue Inhibitor of Metalloproteinases-1 Implications for Regulation of Matrix Degradation in Liver*.

69. Williams, E. J. *et al. Relaxin inhibits eVective collagen deposition by cultured hepatic stellate cells and decreases rat liver fibrosis in vivo*. *Gut* **49**, (2001).

70. Oben, J. A. *et al.* Hepatic fibrogenesis requires sympathetic neurotransmitters. *Gut* **53**, 438–445 (2004).

71. Kanno, K., Tazuma, S. & Chayama, K. AT1A-deficient mice show less severe progression of liver fibrosis induced by CCl4. *Biochem. Biophys. Res. Commun.* **308**, 177–183 (2003).

72. Bataller, R. *et al.* Angiotensin II induces contraction and proliferation of human hepatic stellate cells. *Gastroenterology* **118**, 1149–1156 (2000).

73. Bataller, R. *et al.* Prolonged infusion of angiotensin II into normal rats induces stellate cell activation and proinflammatory events in liver. *Am J Physiol Gastrointest Liver Physiol* **285**, 642–651 (2003).

74. Marra, F. Leptin and liver tissue repair: Do rodent models provide the answers? *J. Hepatol.* **46**, 12–18 (2007).

75. Ikejima, K. *et al.* Leptin receptor-mediated signaling regulates hepatic fibrogenesis and remodeling of extracellular matrix in the rat. *Gastroenterology* **122**, 1399–1410 (2002).

76. Cao, Q., Mak, K. M., Ren, C. & Lieber, C. S. Leptin Stimulates Tissue Inhibitor of Metalloproteinase-1 in Human Hepatic Stellate Cells RESPECTIVE ROLES OF THE JAK/STAT AND JAK-MEDIATED H 2 O 2-DEPENDENT MAPK PATHWAYS*. (2003). doi:10.1074/jbc.M308351200

77. Kamada, Y. *et al.* Enhanced Carbon Tetrachloride-Induced Liver Fibrosis in Mice Lacking Adiponectin. *Gastroenterology* **125**, 1796–1807 (2003).

78. Adachi, M. & Brenner, D. A. High molecular weight adiponectin inhibits proliferation of hepatic stellate cells via activation of adenosine monophosphate-activated protein kinase. *Hepatology* **47**, 677–685 (2008).

79. Pinzani, M. & Luong, T. V. Pathogenesis of biliary fibrosis. *Biochimica et Biophysica Acta - Molecular Basis of Disease* **1864**, 1279–1283 (2018).

80. Ramadori, G. & Saile, B. Portal tract fibrogenesis in the liver. *Laboratory*

Investigation **84**, 153–159 (2004).

81. Pinzani, M. *Springer Seminars in Immunopathology Liver fibrosis*. *Springer Semin Immunopathol* **21**, (2000).

82. Lackner, C. & Tiniakos, D. *Fibrosis and alcohol-related liver disease*. *Journal of Hepatology* **70**, (2019).

83. Hammel, P. *et al.* Regression of Liver Fibrosis after Biliary Drainage in Patients with Chronic Pancreatitis and Stenosis of the Common Bile Duct. *N. Engl. J. Med.* **344**, 418–423 (2001).

84. Dixon, J. B., Bhathal, P. S., Hughes, N. R. & O'Brien, P. E. Nonalcoholic fatty liver disease: Improvement in liver histological analysis with weight loss. *Hepatology* **39**, 1647–1654 (2004).

85. Sun, M. & Kisseleva, T. Reversibility of liver fibrosis. *Clinics and Research in Hepatology and Gastroenterology* **39**, S60–S63 (2015).

86. Iredale, J. P. *Hepatic Stellate Cell Behavior during Resolution of Liver Injury*. *Seminars in Liver Disease* **21**, (2001).

87. Radaeva, S. *et al.* Natural killer cells ameliorate liver fibrosis by killing activated stellate cells in NKG2D-dependent and tumor necrosis factor-related apoptosis-inducing ligand-dependent manners. *Gastroenterology* **130**, 435–452 (2006).

88. Krizhanovsky, V. *et al.* Senescence of Activated Stellate Cells Limits Liver Fibrosis. *Cell* **134**, 657–667 (2008).

89. Kisseleva, T. *et al.* Myofibroblasts revert to an inactive phenotype during regression of liver fibrosis. doi:10.1073/pnas.1201840109

90. Troeger, J. S. *et al.* Deactivation of hepatic stellate cells during liver fibrosis resolution in mice. *Gastroenterology* **143**, (2012).

91. Jirouskova, M., Zbodakova, O., Gregor, M., Chalupsky, K. & Sarnova, L. Hepatoprotective Effect of MMP-19 Deficiency in a Mouse Model of Chronic Liver Fibrosis. *PLoS One* **7**, 46271 (2012).

92. Baeck, C. *et al.* Pharmacological inhibition of the chemokine CCL2 (MCP-1) diminishes liver macrophage infiltration and steatohepatitis in chronic hepatic injury. doi:10.1136/gutjnl-2011-300304

93. Benyon, J. S. *et al.* Resolution of Murine Hepatic Fibrosis Metalloproteinase-13 and Facilitate the Source of Hepatic Matrix Scar-Associated Macrophages Are a Major. *J Immunol Ref.* **178**, 5288–5295 (2007).

94. Fallowfield, J. A. *et al.* Scar-Associated Macrophages Are a Major Source of Hepatic Matrix Metalloproteinase-13 and Facilitate the Resolution of Murine Hepatic Fibrosis. *J. Immunol.* **178**, 5288–5295 (2007).

95. Pellicoro, A. *et al.* Elastin accumulation is regulated at the level of degradation by macrophage metalloelastase (MMP-12) during experimental liver fibrosis. *Hepatology* **55**, 1965–1975 (2012).

96. Ramachandran, P. *et al.* Differential Ly-6C expression identifies the recruited macrophage phenotype, which orchestrates the regression of murine liver fibrosis. doi:10.1073/pnas.1119964109

97. Ramachandran, P. *et al.* Differential Ly-6C expression identifies the recruited macrophage phenotype, which orchestrates the regression of murine liver fibrosis. doi:10.1073/pnas.1119964109

98. Popov, Y. *et al.* Macrophage-mediated phagocytosis of apoptotic cholangiocytes contributes to reversal of experimental biliary fibrosis. *Am. J. Physiol. - Gastrointest. Liver Physiol.* **298**, (2010).

99. Pellicoro, A., Ramachandran, P., Iredale, J. P. & Fallowfield, J. A. Liver fibrosis and repair: immune regulation of wound healing in a solid organ. *Nat. Rev. Immunol.* **14**, 181–194 (2014).

100. Saxena, R. & Theise, N. Canals of Hearing: Recent Insights and Current Knowledge. *Seminars in Liver Disease* **24**, 43–48 (2004).

101. Sackett, S. D. *et al.* Foxl1 is a marker of bipotential hepatic progenitor cells in mice. doi:10.1002/hep.22705

102. Roskams, T. A. *et al.* Nomenclature of the finer branches of the biliary tree:

Canals, ductules, and ductular reactions in human livers. *Hepatology* **39**, 1739–1745 (2004).

103. Bird, T. G., Lorenzini, S. & Forbes, S. J. Activation of stem cells in hepatic diseases. doi:10.1007/s00441-007-0542-z

104. Sato, K. *et al.* Ductular Reaction in Liver Diseases: Pathological Mechanisms and Translational Significances. *Hepatology* **69**, 420–430 (2019).

105. Ró kusz, A. *et al.* Ductular reaction correlates with fibrogenesis but does not contribute to liver regeneration in experimental fibrosis models. (2017). doi:10.1371/journal.pone.0176518

106. Clouston, A. D. *et al.* Fibrosis correlates with a ductular reaction in hepatitis C: Roles of impaired replication, progenitor cells and steatosis. *Hepatology* **41**, 809–818 (2005).

107. Gadd, V. L. *et al.* The portal inflammatory infiltrate and ductular reaction in human nonalcoholic fatty liver disease. *Hepatology* **59**, 1393–1405 (2014).

108. Furuyama, K. *et al.* Continuous cell supply from a Sox9-expressing progenitor zone in adult liver, exocrine pancreas and intestine. *Nat. Genet.* **43**, 34–41 (2011).

109. Shin, S., Upadhyay, N., Greenbaum, L. E. & Kaestner, K. H. Ablation of Foxl1-Cre-labeled hepatic progenitor cells and their descendants impairs recovery of mice from liver injury. *Gastroenterology* **148**, 192-202.e3 (2015).

110. Yanger, K. *et al.* Adult Hepatocytes Are Generated by Self-Duplication Rather than Stem Cell Differentiation AUTHOR CONTRIBUTIONS HHS Public Access. *Cell Stem Cell* **15**, 340–349 (2014).

111. Tarlow, B. D. *et al.* Bipotential adult liver progenitors are derived from chronically injured mature hepatocytes. *Cell Stem Cell* **15**, 605–618 (2014).

112. Morrison, S. J. & Spradling, A. C. *Stem cells and niches: mechanisms that promote stem cell maintenance throughout life*.

113. Roskams, T. *et al.* Oxidative stress and oval cell accumulation in mice and humans with alcoholic and nonalcoholic fatty liver disease. *Am. J. Pathol.*

163, 1301–1311 (2003).

114. Lowes, K. N., Brennan, B. A., Yeoh, G. C. & Olynyk, J. K. Oval cell numbers in human chronic liver diseases are directly related to disease severity. *Am. J. Pathol.* **154**, 537–541 (1999).

115. Kallis, Y. N. *et al.* Remodelling of extracellular matrix is a requirement for the hepatic progenitor cell response. doi:10.1136/gut.2010.224436

116. Van Hul, N. K. M., Abarca-Quinones, J., Sempoux, C., Horsmans, Y. & Leclercq, I. A. Relation between liver progenitor cell expansion and extracellular matrix deposition in a CDE-induced murine model of chronic liver injury. *Hepatology* **49**, 1625–1635 (2009).

117. Chen, L. *et al.* HSCs play a distinct role in different phases of oval cell-mediated liver regeneration. *Cell Biochem. Funct.* **30**, 588–596 (2012).

118. Carpino, G., Renzi, A., Onori, P. & Gaudio, E. Role of Hepatic Progenitor Cells in Nonalcoholic Fatty Liver Disease Development: Cellular Cross-Talks and Molecular Networks. *Int. J. Mol. Sci* **14**, (2013).

119. Ankoma-Sey, V. Hepatic regeneration - Revisiting the myth of Prometheus. *News Physiol. Sci.* **14**, 149–155 (1999).

120. Fausto, N. Liver regeneration. *J. Hepatol. Suppl.* **32**, 19–31 (2000).

121. Taub, R. Liver regeneration: From myth to mechanism. *Nature Reviews Molecular Cell Biology* **5**, 836–847 (2004).

122. Frantz, C., Stewart, K. M. & Weaver, V. M. The extracellular matrix at a glance. *J. Cell Sci.* **123**, 4195–4200 (2010).

123. Rozario, T. & DeSimone, D. W. The extracellular matrix in development and morphogenesis: A dynamic view. *Developmental Biology* **341**, 126–140 (2010).

124. Yeung Tsang, K., H Cheung, M. C., Chan, D. & E Cheah, K. S. The developmental roles of the extracellular matrix: beyond structure to regulation. doi:10.1007/s00441-009-0893-8

125. Iozzo, R. V. & Schaefer, L. Proteoglycan form and function: A comprehensive nomenclature of proteoglycans. *Matrix Biology* **42**, 11–55 (2015).

126. Schaefer, L. & Schaefer, R. M. Proteoglycans: from structural compounds to signaling molecules. doi:10.1007/s00441-009-0821-y

127. Liu, A. Y., Zheng, H. & Ouyang, G. Periostin, a multifunctional matricellular protein in inflammatory and tumor microenvironments. *Matrix Biol.* **37**, 150–156 (2014).

128. Midwood, K. S., Chiquet, M., Tucker, R. P. & Orend, G. Tenascin-C at a glance. *J. Cell Sci.* **129**, 4321–4327 (2016).

129. Horiuchi, K. *et al.* Identification and characterization of a novel protein, periostin, with restricted expression to periosteum and periodontal ligament and increased expression by transforming growth factor β. *J. Bone Miner. Res.* **14**, 1239–1249 (1999).

130. Takeshita, S., Kikuno, R., Tezuka, K.-I. & Amannt, E. *Osteoblast-specific factor 2: cloning of a putative bone adhesion protein with homology with the insect protein fasciclin I*. *Biochem. J* **294**, (1993).

131. Kudo, A. Periostin in fibrillogenesis for tissue regeneration: periostin actions inside and outside the cell. doi:10.1007/s00018-011-0784-5

132. Norris, R. A. *et al.* Periostin Regulates Collagen Fibrillogenesis and the Biomechanical Properties of Connective Tissues. *J Cell Biochem* **101**, 695–711 (2007).

133. Kii, I. *et al.* Incorporation of Tenascin-C into the Extracellular Matrix by Periostin Underlies an Extracellular Meshwork Architecture * □ S. (2009). doi:10.1074/jbc.M109.051961

134. Tanabe, H. *et al.* Periostin Associates with Notch1 Precursor to Maintain Notch1 Expression under a Stress Condition in Mouse Cells. doi:10.1371/journal.pone.0012234

135. Maruhashi, T., Kii, I., Saito, M. & Kudo, A. Interaction between Periostin and BMP-1 Promotes Proteolytic Activation of Lysyl Oxidase * □ S. *J. Biol. Chem.*

285, 13294–13303 (2010).

136. Li, G. *et al.* Phosphatidylinositol-3-kinase signaling mediates vascular smooth muscle cell expression of periostin in vivo and in vitro. *Atherosclerosis* **188**, 292–300 (2006).

137. Uchida, M. *et al.* Periostin, a Matricellular Protein, Plays a Role in the Induction of Chemokines in Pulmonary Fibrosis. doi:10.1165/rcmb.2011-0115OC

138. Hakuno, D. *et al.* Periostin advances atherosclerotic and rheumatic cardiac valve degeneration by inducing angiogenesis and MMP production in humans and rodents. *J. Clin. Invest.* **120**, (2010).

139. Wu, H. *et al.* Periostin expression induced by oxidative stress contributes to myocardial fibrosis in a rat model of high salt-induced hypertension. *Mol. Med. Rep.* **14**, 776–782 (2016).

140. Zhao, S. *et al.* Periostin expression is upregulated and associated with myocardial fibrosis in human failing hearts. *J. Cardiol.* **63**, 373–378 (2014).

141. Sen, K. *et al.* Periostin Is Induced in Glomerular Injury and Expressed de Novo in Interstitial Renal Fibrosis. *Am. J. Pathol.* **179**, 1756–1767 (2011).

142. Hausmann, S. *et al.* Loss of Periostin Results in Impaired Regeneration and Pancreatic Atrophy after Cerulein-Induced Pancreatitis. *Am. J. Pathol.* **186**, 24–31 (2016).

143. Pradeep Kumar, X. *et al.* Periostin promotes liver fibrogenesis by activating lysyl oxidase in hepatic stellate cells. (2018). doi:10.1074/jbc.RA117.001601

144. Huang, Y. *et al.* Matricellular protein periostin contributes to hepatic inflammation and fibrosis. *Am. J. Pathol.* **185**, 786–797 (2015).

145. Bourdon, M. A. *et al. Human Glioma-Mesenchymal Extracellular Matrix Antigen Defined by Monoclonal Antibody*. *CANCER RESEARCH* **43**, (1983).

146. Chiquet, M. & Fambrough, D. M. *Chick Myotendinous Antigen. II. A Novel Extracellular Glycoprotein Complex Consisting of Large Disulfide-linked Subunits*. *THE JOURNAL OF CELL BIOLOGY* **98**, (1984).

147. Grumet, M., Hoffman, S., Crossin, K. L. & Edelman, G. M. *Cytotactin, an extracellular matrix protein of neural and non-neural tissues that mediates glia-neuron interaction (cell-cell adhesion/cell-substrate-adhesion molecule/embryogenesis)*. *Developmental Biology* **82**, (1985).

148. Chiquet-Ehrismann, R., Mackie, E. J., Pearson, C. A. & Sakakura, T. Tenascin: an extracellular matrix protein involved in tissue interactions during fetal development and oncogenesis. *Cell* **47**, 131–139 (1986).

149. Conway, J. F. & Parry, D. A. D. Three-stranded α-fibrous proteins: the heptad repeat and its implications for structure. *Int. J. Biol. Macromol.* **13**, 14–16 (1991).

150. Fischer, D., Brown-Lüdi, M., Schulthess, T. & Chiquet-Ehrismann, R. Concerted action of tenascin-C domains in cell adhesion, anti-adhesion and promotion of neurite outgrowth. *J. Cell Sci.* **110**, 1513–1522 (1997).

151. Götz, M., Bolz, J., Joester, A. & Faissner, A. Tenascin-C Synthesis and Influence on Axonal Growth During Rat Cortical Development. *Eur. J. Neurosci.* **9**, 496–506 (1997).

152. Pas, J. *et al.* Analysis of structure and function of tenascin-C. *Int. J. Biochem. Cell Biol.* **38**, 1594–1602 (2006).

153. Oberhauser, A. F., Marszalek, P. E., Erickson, H. P. & Fernandez, J. M. The molecular elasticity of the extracellular matrix protein tenascin. *Nature* **393**, 181–185 (1998).

154. Orend, G. Potential oncogenic action of tenascin-C in tumorigenesis. *International Journal of Biochemistry and Cell Biology* **37**, 1066–1083 (2005).

155. Jones, F. S. & Jones, P. L. The tenascin family of ECM glycoproteins: Structure, function, and regulation during embryonic development and tissue remodeling. *Dev. Dyn.* **218**, 235–259 (2000).

156. Fluck, M., Tunc-Civelek, V. & Chiquet, M. Rapid and reciprocal regulation of tenascin-C and tenascin-Y expression by laoading of skeletal muscle. *J. Cell*

Sci. **113**, 3583–3591 (2000).

157. Goh, F. G., Piccinini, A. M., Krausgruber, T., Udalova, I. A. & Midwood, K. S. Transcriptional Regulation of the Endogenous Danger Signal Tenascin-C: A Novel Autocrine Loop in Inflammation. *J. Immunol.* **184**, 2655–2662 (2010).

158. Midwood, K. S. & Orend, G. The role of tenascin-C in tissue injury and tumorigenesis. doi:10.1007/s12079-009-0075-1

159. Chiquet-Ehrismann, R. & Chiquet, M. Tenascins: Regulation and putative functions during pathological stress. *J. Pathol.* **200**, 488–499 (2003).

160. Jinnin, M. *et al.* Platelet derived growth factor induced tenascin-C transcription is phosphoinositide 3-kinase/Akt-dependent and mediated by Ets family transcription factors. *J. Cell. Physiol.* **206**, 718–727 (2006).

161. Jinnin, M. *et al.* Tenascin-C upregulation by transforming growth factor-b in human dermal fibroblasts involves Smad3, Sp1, and Ets1. *Oncogene* **23**, 1656–1667 (2004).

162. Zhao, Y., Young, S. L. & McIntosh, J. C. Induction of tenascin in rat lungs undergoing bleomycin-induced pulmonary fibrosis. *Am. J. Physiol. - Lung Cell. Mol. Physiol.* **274**, (1998).

163. Kaarteenaho-Wiik, R., Mertaniemi, P., Sajanti, E., Soini, Y. & Pääkkö, P. *Tenascin is Increased in Epithelial Lining Fluid in Fibrotic Lung Disorders*.

164. Esposito, I. *et al.* Tenascin C and annexin II expression in the process of pancreatic carcinogenesis. *J. Pathol.* **208**, 673–685 (2006).

165. El-Karef, A. *et al.* Deficiency of tenascin-C attenuates liver fibrosis in immune-mediated chronic hepatitis in mice. *J. Pathol.* **211**, 86–94 (2007).

166. Ma, J.-C. *et al.* Tenascin-C promotes migration of hepatic stellate cells and production of type I collagen. *Biosci. Biotechnol. Biochem.* **80**, 1470–1477 (2016).

167. Jones, P. L. & Jones, F. S. Tenascin-C in development and disease: Gene regulation and cell function. *Matrix Biology* **19**, 581–596 (2000).

168. Fengler, V. H. I. *et al.* Susceptibility of Different Mouse Wild Type Strains to Develop Diet-Induced NAFLD/ AFLD-Associated Liver Disease. (2016). doi:10.1371/journal.pone.0155163

169. Walkin, L. *et al. The role of mouse strain differences in the susceptibility to fibrosis: a systematic review*. (2013). doi:10.1186/1755-1536-6-18

170. Tag, C. G. *et al.* Bile Duct Ligation in Mice: Induction of Inflammatory Liver Injury and Fibrosis by Obstructive Cholestasis. *J. Vis. Exp.* 1–11 (2015). doi:10.3791/52438

171. Hofmann, A. F. & Hagey, L. R. Bile acids: Chemistry, pathochemistry, biology, pathobiology, and therapeutics. *Cell. Mol. Life Sci.* **65**, 2461–2483 (2008).

172. Abshagen, K. *et al.* Pathobiochemical signatures of cholestatic liver disease in bile duct ligated mice. *BMC Syst. Biol.* **9**, (2015).

173. Li, M., Cai, S.-Y. & Boyer, J. L. Mechanisms of bile acid mediated Inflammation in the Liver. doi:10.1016/j.mam.2017.06.001

174. Scholten, D., Trebicka, J., Liedtke, C. & Weiskirchen, R. The carbon tetrachloride model in mice. *Lab. Anim.* **49**, 4–11 (2015).

175. D Weber, L. W., Boll, M. & Stampfl, A. Hepatotoxicity and Mechanism of Action of Haloalkanes: Carbon Tetrachloride as a Toxicological Model. *Crit. Rev. Toxicol.* **33**, 105–136 (2003).

176. Animal Models for Fibrotic Liver Diseases: What We Have, What We Need, and What Is under Development. *J. Clin. Transl. Hepatol.* **3**, 53–66 (2015).

177. Hillebrandt, S., Goos, C., Matern, S. & Lammert, F. Genome-wide analysis of hepatic fibrosis in inbred mice identifies the susceptibility locus Hfib1 on chromosome 15. *Gastroenterology* **123**, 2041–2051 (2002).

178. Shi, Z., Wakil, A. E. & Rockey, D. C. *Strain-specific differences in mouse hepatic wound healing are mediated by divergent T helper cytokine responses*. **94**, (1997).

179. Nevzorova, Y., Tolba, R., Trautwein, C. & Liedtke, C. Partial hepatectomy in mice. *Lab. Anim.* **49**, 81–88 (2015).

180. Michalopoulos, G. K. Rous-Whipple Award Lecture Liver Regeneration after Partial Hepatectomy Critical Analysis of Mechanistic Dilemmas. *Am. J. Pathol.* **176**, 2–13 (2010).

181. Wang, Y. *et al.* Gender-dependent histone deacetylases injury may contribute to differences in liver recovery rates of male and female mice. *Transplant. Proc.* **45**, 463–473 (2013).

182. Sánchez-Hidalgo, J. M. *et al.* Impact of age on liver regeneration response to injury after partial hepatectomy in a rat model. *J. Surg. Res.* **175**, (2012).

183. Sato, K. *et al.* Ductular Reaction in Liver Diseases: Pathological Mechanisms and Translational Significances. *Hepatology* **69**, 420–430 (2019).

184. 009067 - B6;129-Postn/J. Available at: https://www.jax.org/strain/009067. (Accessed: 6th September 2019)

185. González-González, L. & Alonso, J. Periostin: A Matricellular Protein With Multiple Functions in Cancer Development and Progression. *Front. Oncol.* **8**, 225 (2018).

186. Oka, T. *et al.* Genetic Manipulation of Periostin Expression Reveals a Role in Cardiac Hypertrophy and Ventricular Remodeling. *Circ. Res.* **101**, 313–321 (2007).

187. RBRC_No.RBRC00169. Available at: https://www2.brc.riken.jp/lab/animal/detail.php?brc_no=RBRC00169. (Accessed: 6th September 2019)

188. Matsumoto, K., Hiraiwa, N., Yoshiki, A., Ohnishi, M. & Kusakabe, M. Tenascin-C Expression and Splice Variant in Habu Snake Venom-Induced Glomerulonephritis. *Exp. Mol. Pathol.* **72**, 186–195 (2002).

189. Mähler (Convenor), M. *et al.* FELASA recommendations for the health monitoring of mouse, rat, hamster, guinea pig and rabbit colonies in breeding and experimental units. *Lab. Anim.* **48**, 178–192 (2014).

190. Longerich, T., Flechtenmacher, C. & Schirmacher, P. Maß und Zahl in der HepatopathologieQuality and quantity in hepatopathology. *Pathologe* **29**,

15–26 (2008).

191. Bateman, A. C. & Hübscher, S. G. Cytokeratin expression as an aid to diagnosis in medical liver biopsies. *Histopathology* **56**, 415–425 (2010).

192. Tanimizu, N. *et al.* Progressive induction of hepatocyte progenitor cells in chronically injured liver. *Sci. Rep.* **7**, 1–13 (2017).

193. Hirsch, F. R. *et al.* Epidermal growth factor receptor in non-small-cell lung carcinomas: Correlation between gene copy number and protein expression and impact on prognosis. *J. Clin. Oncol.* **21**, 3798–3807 (2003).

194. Kreipe, H. Ki67-Tumorheterogenität vs. Assayheterogenität. *Pathologe* **39**, 272–277 (2018).

195. Katoonizadeh, A. & Poustchi, H. *Adult Hepatic Progenitor Cell Niche: How it affects the Progenitor Cell Fate*. *Middle East Journal of Digestive Diseases* **6**, (2014).

196. El-Karef, A. *et al.* Deficiency of tenascin-C attenuates liver fibrosis in immune-mediated chronic hepatitis in mice. *J. Pathol.* **211**, 86–94 (2007).

197. Wu, T. *et al.* Deficiency of periostin impairs liver regeneration in mice after partial hepatectomy. *Matrix Biol.* **66**, 81–92 (2018).

198. Saga, Y., Yagi, T., Ikawa, Y., Sakakura, T. & Aizawa, S. Mice develop normally without tenascin. *Genes Dev.* **6**, 1821–1831 (1992).

199. Yamashita, O., Yoshimura, K., Nagasawa, A., Ueda, K. & Morikage, N. Periostin Links Mechanical Strain to Inflammation in Abdominal Aortic Aneurysm. *PLoS One* **8**, 79753 (2013).

200. Kato, H., Duarte, S., Miller, M. G., Busuttil, R. W. & Coito, A. J. Overproduction of Tenascin-C Driven by Lipid Accumulation in the Liver Aggravates Hepatic Ischemia/Reperfusion Injury in Steatotic Mice. *Liver Transplant.* **25**, 288–301 (2019).

201. Meng, X., Zhu, Y., Tao, L., Zhao, S. & Qiu, S. Periostin has a protective role in melatonin-induced cell apoptosis by inhibiting the eIF2a-ATF4 pathway in human osteoblasts. *Int. J. Mol. Med.* **41**, 1003–1012 (2018).

202. Nakahara, H. *et al.* Deficiency of tenascin C attenuates allergen-induced bronchial asthma in the mouse. *Eur. J. Immunol.* **36**, 3334–3345 (2006).

203. Kaur, S., Siddiqui, H. & Bhat, M. H. Hepatic Progenitor Cells in Action Liver Regeneration or Fibrosis? *American Journal of Pathology* **185**, 2342–2350 (2015).

204. Storz, P. Acinar cell plasticity and development of pancreatic ductal adenocarcinoma. *Nature Reviews Gastroenterology and Hepatology* **14**, 296–304 (2017).

205. Garwood, J. *et al.* The extracellular matrix glycoprotein Tenascin-C is expressed by oligodendrocyte precursor cells and required for the regulation of maturation rate, survival and responsiveness to platelet-derived growth factor. *Eur. J. Neurosci.* **20**, 2524–2540 (2004).

206. LeSage, G. D. *et al.* Acute carbon tetrachloride feeding selectively damages large, but not small, cholangiocytes from normal rat liver. *Hepatology* **29**, 307–319 (1999).

207. Chen, J. *et al.* The Extracellular Matrix Glycoprotein Tenascin-C Is Beneficial for Spinal Cord Regeneration. (2010). doi:10.1038/mt.2010.133

208. Liedtke, C. *et al.* Experimental liver fibrosis research: Update on animal models, legal issues and translational aspects. *Fibrogenes. Tissue Repair* **6**, (2013).

209. Demetrius, L. Of mice and men. *EMBO Rep.* **6**, (2005).

IX. APPENDIX

1. List of figures

2. List of tables

X. ACKNOWLEDGEMENTS

Zunächst möchte ich mich bei meiner Mentorin Frau Prof. Esposito bedanken. Ich danke Ihnen für das entgegengebrachte Vertrauen zur Durchführung der tierexperimentellen Arbeiten und die Möglichkeit meine Dissertation an Ihrem Institut anfertigen zu können. Danke, dass ich mich im Bereich der Versuchstierkunde weiterbilden durfte und durch Sie viel über die Pathologie der Maus lernen konnte.

Bei Herrn PD DR. Dahlhoff bedanke ich mich ganz herzlich für die Übernahme meiner Dissertation und die Betreuung an der tierärztlichen Fakultät.

Ich danke auch dem ganzen Team der Pathologie des Universitätsklinikums Düsseldorf. Den „Routine-Mädels“ danke ich dafür, dass sie mir stets geholfen haben und wertvolle Tipps rund um die Histologie gaben. Andrea Cacciato Insilla danke ich für die Unterstützung bei der histologischen Auswertung. Außerdem möchte ich mich bei den anderen Doktoranden bedanken, besonders bei Lisa, die mich immer ermutigt hat und während meiner Zeit am Institut zur echten Freundin wurde.

Herrn Prof. Sager und dem ganzen Team der ZETT danke ich für die zahlreichen Fortbildungsstunden und der Weiterbildung im Bereich der Versuchstierkunde. Ganz besonders möchte ich mich bei PD Dr. Benten, Elke und den Tierpflegern für die Unterstützung, die wertvollen Ratschlage und die gute Zusammenarbeit bedanken.

Meinen Freundinnen möchte ich besonders für ihre Motivation und Unterstützung danken. Danke, dass ihr immer für mich da seid – egal wie viele Kilometer zwischen uns liegen.

Mein herzlichster Dank gilt meiner Familie. Tina, für das aufmerksame Korrekturlesen. Meinen Geschwistern Julia und Franz, die immer für mich da sind, mich motivieren und stets daran erinnern niemals das Ziel aus den Augen zu verlieren. Meinen Eltern Monika und Franz, die mir das Studium ermöglicht haben und mich immer unterstützen – ohne Sie wäre diese Arbeit nicht möglich gewesen.

Lieber Tim, danke für deine unendliche Geduld und deinen Optimismus. Danke, dass du immer für mich da bist, mich beruhigst und mich immer wieder zum Lachen bringst.